2017

Polarization Observables in Double Pion Photo-Production with Circularly Polarized Photons off Transversely Polarized Protons

Lelia Aneta Net
University of South Carolina

Polarization observables in double pion photo-production with circularly polarized photons off transversely polarized protons

by

Lelia Aneta Net

Bachelor of Science
West University of Timisoara, 2001

Master of Science
West University of Timisoara, 2003

Submitted in Partial Fulfillment of the Requirements

for the Degree of Doctor of Philosophy in

Physics

College of Arts and Sciences

University of South Carolina

2017

Accepted by:

Steffen Strauch, Major Professor

Ralf Gothe, Committee Member

Camelia Knapp, Committee Member

Milind Purohit, Committee Member

Cheryl L. Addy, Vice Provost and Dean of the Graduate School

Dedication

This work is dedicated to my beloved family: my parents Ana and Gheorghe Neț, my sister and best friend Natalia, my nephews Alex and Bogdan, my grandparents Floare and Petru Neț, and my great-grandmother Maria Creț.

Acknowledgments

I would like to thank God for His never-ceasing love and kindness, and for the people who helped me accomplish this work.

I would like to express my deep gratitude to my advisor, Professor Steffen Strauch, for his support, guidance, and for the time he spent helping me during this analysis. He continuously inspired me and patiently guided me through all the steps of my research endeavor, and I highly appreciate it.

I am also indebted to my dissertation committee members: Professor Ralf Gothe, Professor Camelia Knapp and Professor Milind Purohit for their time, insight, and support. I would also like to thank Professor Yordanka Ilieva for her feedback and assistance.

Many thanks also go to the members of FROST g9b group for sharing their knowledge and experience on so many occasions.

Last but not least, it was my privilege to be part of the USC experimental nuclear physics group, a wonderful team of researchers who are friendly, generous and supportive.

Abstract

The study of excited states of the nucleon facilitates the understanding of the nucleon structure and its underlying symmetry and couplings. A main goal of the N^* program at the Thomas Jefferson National Accelerator Facility is to investigate the excitation and decays of the baryon resonances and assist in identifying the "missing" nucleon resonances that are predicted by theoretical models. One way to study the nucleon resonances is by extracting polarization observables, which provide more information than the unpolarized cross-section studies, e.g. access to the transition amplitudes of the reaction. Double-pion photoproduction contributes strongly to the total cross section at high energies and thus it plays an important role in probing the nucleon resonance spectrum. The CLAS g9b (FROST) experiment at Thomas Jefferson National Accelerator Facility provided double-pion photoproduction data using transversely polarized protons and circularly polarized photons, with energies up to 3.0 GeV. Beam- and target-polarization asymmetries were measured and the polarization observables $I^{\odot}$, $P_x^{\odot}$, $P_y^{\odot}$, P_x, P_y were extracted for the $\gamma p \to p\pi^+\pi^-$ reaction. The results are reported and compared with the calculations of an effective Lagrangian model. The data will help deepen the current knowledge of hadronic resonance decays and possibly assist in identifying new baryon resonances via PWA (Partial Wave Analysis) and in this way will contribute to a more comprehensive understanding of the strong interaction.

Table of Contents

List of Tables

List of Figures

Chapter 1

Introduction

"The important thing is not to stop questioning. Curiosity has its own reason for existing."

Albert Einstein

1.1 Quantum Chromodynamics

Quantum Chromodynamics (QCD) is the field theory that describes the strong interaction of colored quarks and gluons. It is an important branch of theoretical physics and its goal is to answer the questions regarding the structure and the interactions of hadrons, which are subatomic particles made out of quarks and bound together by the strong force. QCD describes the strong interactions, e.g. describes how gluons and quarks interact inside a hadron (e.g. proton, neutron, or pion). Quarks are considered to be elementary particles and there are six different flavor types: up, down, strange, charm, bottom, and top and they are the building blocks of the hadrons. In order to quantify the properties of hadrons, a unique set of quantum numbers (e.g. spin, parity, charge parity, etc.) is used, where each number quantifies one property of the hadron. A combination of three valence quarks is called a baryon (e.g. proton and neutron) and when a quark and antiquark combine a meson is formed (e.g. pion). Baryons and mesons are both part of the hadron family, and one interesting property of this composite particle family is regarding

their masses: a hadron is much heavier than the quarks inside of it. But wait! Where is this mass difference coming from? The other hadron components that were not yet defined are the gluons, and they are force-mediating particles (bosons) that come in 8 different types and are massless. So the mass difference in hadrons must come from the strong force field, more specifically from the indeterminate number of virtual quark-antiquark pairs that are created and annihilated continuously inside hadrons.

In QCD there are two unusual and interesting properties: confinement and asymptotic freedom. Confinement, means that a quark cannot be isolated by itself but will always be confined with other quarks. The consequence of the confinement is that quarks are never observed free in nature, but they are always bound inside hadrons. The other property is asymptotic freedom, namely the particle binding is asymptotically weaker when the energy increases and the distance gets smaller. At short distances or at high energies the strong coupling constant is small (quarks bind weakly) and the perturbative QCD (pQCD) describes well the strong interaction in this energetic regime. The problem arises at lower energies ($r \gtrsim 0.1$ fm), where the asymptotic freedom disappears and treating the problem perturbatively is not possible anymore, due to a large coupling constant and a nonlinear behaviour of the strong force, alternative avenues are needed in order to describe the phenomena at these lower energies.

The goal of this work is to contribute to the effort of understanding the low energy non-pQCD regime better, more specifically to understand the complex nucleon structure and the dynamics of its excited states.

1.2 Baryon Spectroscopy And Models Of The Excited States Of Baryons

Baryon spectroscopy is an important branch of particle physics that studies the masses, the properties, and the decay phenomena of baryons and is attempting to solve the problems encountered by QCD in the nonperturbative regime. Since the

pQCD theoretical approach does not work in the low energetic regime, several models were developed in order to understand the structure and properties of baryons. These models predict a series of nucleon resonances, and the existence of some predicted resonances has already been confirmed by looking at the experimental data and for other predicted resonances there is an ongoing effort that will confirm or not their existence.

A model that gives good predictions regarding the hadron properties is the **Constituent quark model (CQM)** [1], which provides an intuitive description of the baryon structure. This model considers that baryons are made only of constituent quarks (see Fig. 1.1, left), whose masses are much larger than the masses of the valence quarks because they are "dressed" with gluons and quark-antiquark pairs, so that the sum of their masses approximately equals the mass of the hadron. The typical

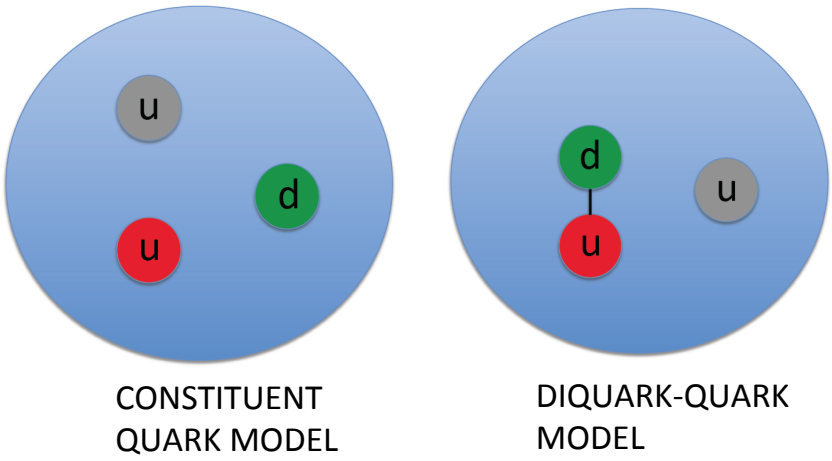

Figure 1.1: lllustration of the proton configuration in the CQM model (right), and in the diquark-quark model (left), where the u stands for the up quark and d represents the down quark.

Hamiltonian consists of a kinetic-energy operator and a potential term including all

quark-quark interactions. The constituent quarks determine the degrees of freedom of a specific baryon (e.g. spin, spatial degree of freedom). These constituent quarks move in the confining potential, and in order to understand the system dynamics the wave equation must be solved for the three quarks moving in the confining inter-quark potential that includes spin-dependent and spin-independent terms, whose solutions include the mass and eigenstates of the ground state baryon and baryon excited state. In a relativistic form, the kinetic-energy term of the Hamiltonian includes the masses and 3-momenta of the constituent quarks and the potential could include a one-gluon exchange (OGE) term or a Goldstone-boson exchange (GBE) term. The OGE model potential includes a Coulomb term, a linear confinement term and a flavor-independent spin-spin interaction term, while the GBE model potential includes a linear confinement term and only the spin-spin part of the meson. These two models (Fig. 1.2) predict a series of different resonance masses, which are located in a wide range of the mass spectrum and many of the predicted ones are yet to be observed.

The Diquark-quark model [3] is a non-relativistic potential model assuming that two quarks are bound inside the baryon forming a diquark and the other quark is unpaired (see Fig. 1.1, left). Because of the binding between the two quarks, some degrees of freedom are frozen, which leads to predicting fewer nucleon resonances. The Hamiltonian includes a Coulomb-like potential, a confining potential, and an exchange potential due to the spins and the isospins of the quark and diquark and this exchange potential is the main characteristic of this model. Since the theoretical calculation of this model reproduces the baryon resonance spectrum by computing the resonance mass, an example of calculation would be the mass of $N(939)$ being equal to 940 MeV and for the mass of $N(1720)$ the calculation gives 1675 MeV [3]. The diquark-quark model predicts fewer resonance states than the constituent quark model.

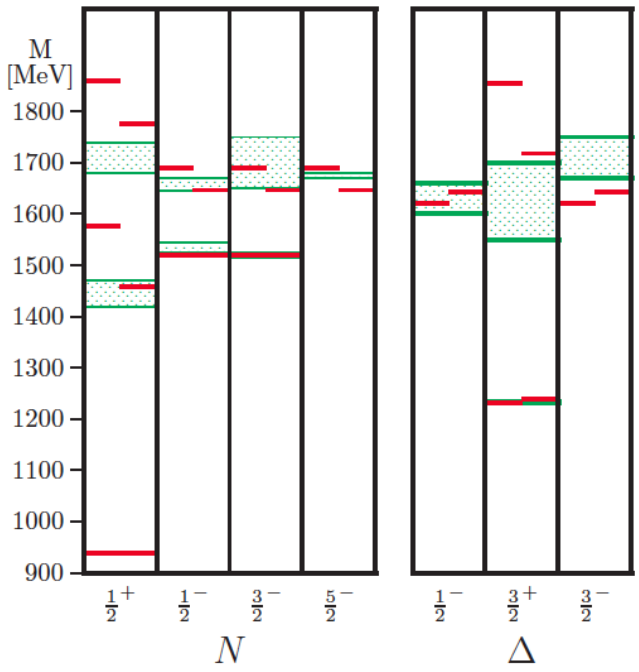

Figure 1.2: The N and Δ states with total angular momentum J^P for CQM model $\mathcal{A}$ (left lines) and model $\mathcal{B}$ (right lines) and the green shaded box representing the experimental data with their uncertainties equal to the width of the band. Figure taken from [2].

Lattice Quantum Chromodynamics (LQCD) [4], is a numerical approach of QCD in the non-perturbative regime and one of its goals is to calculate the quantities characterizing the nucleon, and its predictions must match the experimental data. In LQCD, quarks are lattice nodes and gluons are links between the lattice nodes in a discrete space and time configuration with six unknown parameters entering the calculation: the coupling constant α and the masses of the 5 out of 6 quarks (the top quark is excluded due to its fast decay time). In this way, LQCD allows the calculations of the masses and properties of the numerous particles or nucleon excited states that have the up, down, strange, charm and bottom quark in their composition. Once the calculations are done, the results (e.g. baryon masses) are compared with the experimental data to see if there is an agreement. For example, some of the results of LQCD are shown in Fig. 1.3.

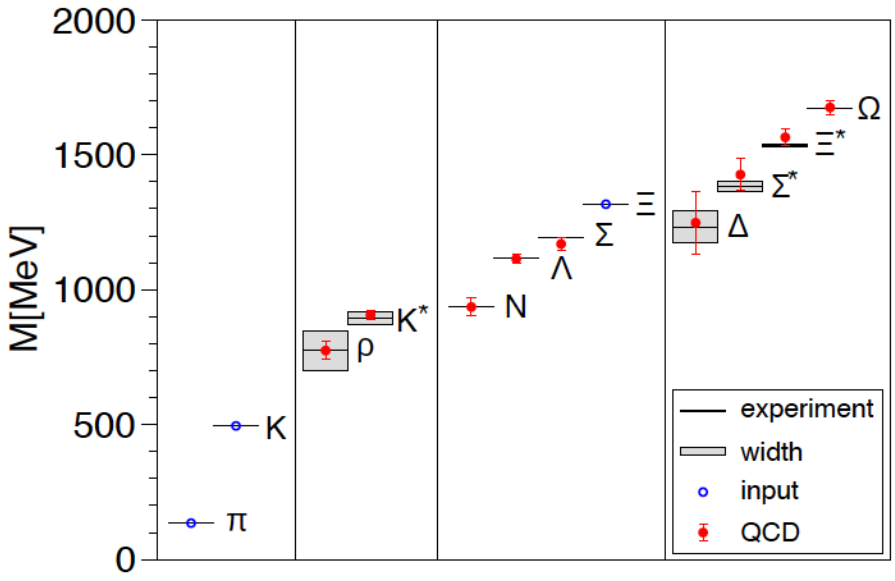

Figure 1.3: Comparison between the experimental data and LQCD calculations for different hadron masses. Figure taken from [4].

Currently, the solutions provided by LQCD are only limited by the computational power available and by the efficiency of the algorithms that are being used.

Missing resonance problem

As stated before, when describing the baryon resonances, various models predict more nucleon resonances than the already observed resonances and this becomes "the missing resonance" problem. Table 1.1 shows the status of different baryon resonances as of 2016. The notation **** in the table means the resonance existence is certain, and properties are at least fairly well explored, *** the existence is very likely but further confirmation of decay mode is required, ** the evidence of existence is only fair, * the evidence of existence is only poor. Figure 1.4 shows an example of experimental measurements versus model predictions [5] for different baryon Δ resonances and one can clearly see that the predicted resonances are more than the observed resonances.

Table 1.1: The nucleon-resonance spectrum (Table taken from [7])

Particle	J^P	overall	$N\gamma$	$N\pi$	$N\eta$	$N\sigma$	$N\omega$	ΛK	ΣK	$N\rho$	$\Delta\pi$
N	$1/2^+$	****									
N(1440)	$1/2^+$	****	****	****		***				*	***
N(1520)	$3/2^-$	****	****	****	***					***	***
N(1535)	$1/2^-$	****	****	****	****					**	*
N(1650)	$1/2^-$	****	****	****	***			***	**	**	***
N(1675)	$5/2^-$	****	****	****	*			*		*	***
N(1680)	$5/2^+$	****	****	****	*	**				***	***
N(1700)	$3/2^-$	***	**	***	*			*	*	*	***
N(1710)	$1/2^+$	****	****	****	***		**	****	**	*	**
N(1720)	$3/2^+$	****	****	****	***			**	**	**	*
N(1860)	$5/2^+$	**		**						*	*
N(1875)	$3/2^-$	***	***	*			**	***	**		***
N(1880)	$1/2^+$	**	*	*		**		*			
N(1895)	$1/2^-$	**	**	*	**			**	*		
N(1900)	$3/2^+$	***	***	**	**		**	***	**	*	**
N(1990)	$7/2^+$	**	**	**					*		
N(2000)	$5/2^+$	**	**	*	**			**	*	**	
N(2040)	$3/2^+$	*		*							
N(2060)	$5/2^-$	**	**	**	*					**	
N(2100)	$1/2^+$	*		*							
N(2120)	$3/2^-$	**	**	**				*	*		
N(2190)	$7/2^-$	****	***	****			*	**		*	
N(2220)	$9/2^+$	****		****							
N(2250)	$9/2^-$	****		****							
N(2300)	$1/2^+$	**		**							
N(2570)	$5/2^-$	**		**							
N(2600)	$11/2^-$	***		***							
N(2700)	$13/2^+$	**		**							

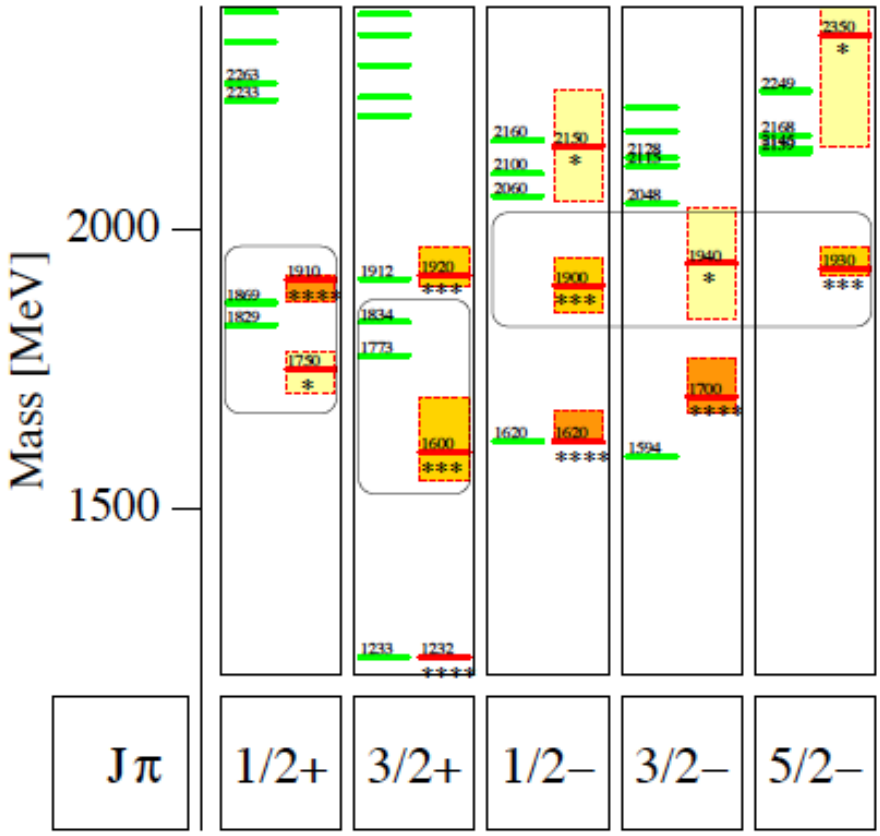

Figure 1.4: Δ resonance mass spectrum from a relativistic quark model [5]. The green lines represent the model results and the yellow and orange bands represent the experimental data and the star ratings denotes the status of that Δ resonance according to PDG and were already explained for Table 1.1. For each total spin J and parity π more excited baryon states are predicted than experimentally observed. Figure taken from [6].

As already shown, the experimental data plays a crucial role in solving the missing resonance problem. After all the expected experimental data are made available, the next step to follow in order to solve the "missing resonance" problem is to perform a coupled-channel analysis and constrain reaction models and Partial Wave Analyses (PWA) to improve the extraction of resonances from the data. In addition to the already available data from other reaction channels, it is expected that new experimental data for single- and double-pion photoproduction will be provided by collaborations like CLAS, GRAAL, LEPS, MAMI, and CB-ELSA and a combined

analysis of these data sets will take place. The way to achieve this combined analysis is through PWA done by groups like the Bonn/Gatchina PWA, SAID, MAID, whose analyses are expected to reveal a set of new baryon resonances.

1.3 Why $\vec{\gamma}\vec{p} \to p\ \pi^+\ \pi^-$?

The scope of this analysis is to study the excitation and decay processes of proton resonances in the low-lying energy regime. The study of the interaction processes at lower energies (nonperturbative QCD regime) promises a better understanding of the strong force that governs the internal structure of hadrons. For each ground state nucleon, there are several excited states and these excited states decay very quickly through the strong nuclear force and this decay can happen through different reaction channels. The study of the nucleon decay dynamics could reveal which resonant states are coupled to a specific reaction channel. Looking only at the unpolarized differential cross section data was proven to be insufficient, because it contains only the magnitude of the transition amplitudes and in order to gain access to the phase of the amplitude, polarization observables were extracted, and 4 out of 5 polarization observables extracted in this analysis are seen for the first time. This analysis focuses on the double pion photoproduction off the proton, where the nucleon resonance decays into two charged pions and a proton. Why double pion photoproduction? Because it is the highest contributor channel to the photoabsorption cross section on the free proton at higher invariant masses (as shown in Fig. 1.5) and because it brings supplementary information about the nucleon decay properties in addition to what the single pion photoproduction could provide. Also it is expected that many higher-energy resonances follow a $N\pi\pi$ decay and as an example when looking at the branching ratios of the nucleon resonance $N(1720)$ one sees that the dominant decay mode of this excited state is the $N\pi\pi$ channel with a fraction between 70%-80%, while the single pion channel's fraction amounts to only 11% [8]. Analyzing double pion

photoproduction could assist in a more deeper investigation of low energy states (e.g. $N(1440)$ also called Roper resonance) and also in the higher energy range (around 1900 MeV) it could assist in studying the negative parity Δ resonances for which there is not much evidence currently.

In addition, these experimental results were compared to theoretical model calculation and will help further constrain the model calculations.

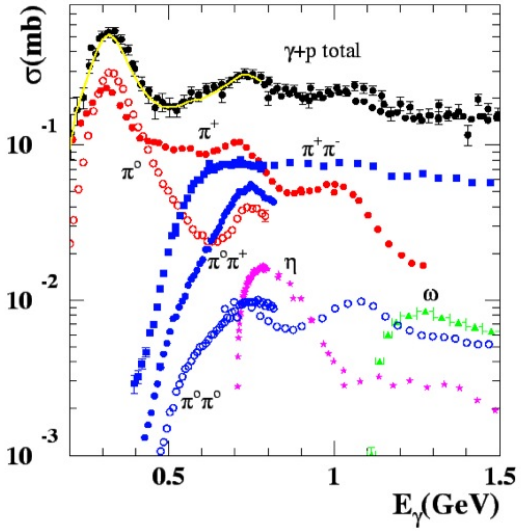

Figure 1.5: Photoabsorption cross section on the free proton, showing that the double pion channel is dominant at high energies. Figure taken from [9].

1.4 Polarization Observables

In photoproduction experiments off nucleons, different resonant and non-resonant terms interfere. The unpolarized differential cross section provides information only on the sum of absolute squares of the helicity amplitudes. And so polarization observables are extracted in order to have access to the phase of the transition amplitudes,

$$i\mathscr{M} = \chi^{\dagger}(\mathscr{A} + \vec{\sigma} \cdot \vec{\mathscr{B}})\phi, \tag{1.1}$$

where $\mathscr{M}$ represents the helicity transition amplitude, χ, ϕ are Pauli spinors for the final and initial nucleons, and $\mathscr{A}$, $\vec{\mathscr{B}}$ contain all the details of the model describing the studied interaction [10]. Due to different helicity combinations of the target nucleon, recoil nucleon, and photon, there are 8 helicity transition amplitudes in total, and each individual amplitude squared gives the probability that the system transitioned from a given initial helicity state combination to a given final helicity state combination. Using the helicity transition amplitudes one can construct another set of amplitudes, which are called transversity amplitudes, whose different combinations also give the magnitude of the polarization observables. For the photoproduction off the proton, there are 64 polarization observables arising in total, out of which 28 observables relate via their absolute magnitudes, 21 relate via transversity amplitude phases and 15 are independent quantities. In double pion photoproduction with circularly polarized photon beam and transversely polarized protons, there are 5 polarization observables arising due to the polarization of the photon beam and of the nucleon target and their helicity amplitudes compositions are [10]

$$I_0 = |\mathscr{M}_1^-|^2 + |\mathscr{M}_1^+|^2 + |\mathscr{M}_2^-|^2 + |\mathscr{M}_2^+|^2 + |\mathscr{M}_3^-|^2 + |\mathscr{M}_3^+|^2 + |\mathscr{M}_4^-|^2 + |\mathscr{M}_4^+|^2, \quad (1.2)$$

$$I_0 P_x = 2\Re(\mathscr{M}_1^- \mathscr{M}_3^{-*} + \mathscr{M}_1^+ \mathscr{M}_3^{+*} + \mathscr{M}_2^- \mathscr{M}_4^{-*} + \mathscr{M}_2^+ \mathscr{M}_4^{+*}), \quad (1.3)$$

$$I_0 P_y = -2\Im(\mathscr{M}_1^- \mathscr{M}_3^{-*} + \mathscr{M}_1^+ \mathscr{M}_3^{+*} + \mathscr{M}_2^- \mathscr{M}_4^{-*} + \mathscr{M}_2^+ \mathscr{M}_4^{+*}), \quad (1.4)$$

$$I_0 I^{\odot} = -|\mathscr{M}_1^-|^2 + |\mathscr{M}_1^+|^2 - |\mathscr{M}_2^-|^2 + |\mathscr{M}_2^+|^2 - |\mathscr{M}_3^-|^2 + |\mathscr{M}_3^+|^2 - |\mathscr{M}_4^-|^2 + |\mathscr{M}_4^+|^2, \quad (1.5)$$

$$I_0 P_x^{\odot} = 2\Re(-\mathscr{M}_1^- \mathscr{M}_3^{-*} + \mathscr{M}_1^+ \mathscr{M}_3^{+*} - \mathscr{M}_2^- \mathscr{M}_4^{-*} + \mathscr{M}_2^+ \mathscr{M}_4^{+*}), \quad (1.6)$$

$$I_0 P_y^{\odot} = 2\Im(\mathscr{M}_1^- \mathscr{M}_3^{-*} - \mathscr{M}_1^+ \mathscr{M}_3^{+*} + \mathscr{M}_2^- \mathscr{M}_4^{-*} - \mathscr{M}_2^+ \mathscr{M}_4^{+*}), \quad (1.7)$$

where the $\pm$ signs represent the photon helicity states and the indices $1, 2, 3, 4$ represent the following sign combinations of the nucleon helicity before and after interaction: $(++)$, $(+-)$, $(-+)$, and $(--)$.

The reaction rate for $\vec{\gamma}\vec{p} \to p\,\pi^+\pi^-$ with circularly polarized photons and transversely polarized nucleon is written as

$$\rho_f I = I_0[(1 + \vec{\Lambda_i} \cdot \vec{P_i}) + \delta_{\odot}(I^{\odot} + \vec{\Lambda_i} \cdot \vec{P_i^{\odot}})], \quad (1.8)$$

where $\rho_f = \frac{1}{2}(1 + \vec{\sigma} \cdot \vec{P'})$ is the density matrix of the recoiling nucleon,

I_0 the unpolarized cross section term,

$\vec{\Lambda}$ the target polarization,

$\vec{P}$ the target polarization cross section asymmetry,

$\delta_\odot$ the degree of the beam circular polarization,

$I^\odot$ the beam helicity cross section asymmetry, and

$\vec{P}^\odot$ the cross section asymmetry due to the beam and target polarization.

Using the angle α between the transverse target polarization $\vec{\Lambda}$ and the x-axis in the reaction frame (see Fig. 6.1), the reaction rate is

$$\rho_f I = I_0[(1+\Lambda\cdot\cos\alpha\cdot P_x+\Lambda\cdot\sin\alpha\cdot P_y)+\delta_\odot(I^\odot+\Lambda\cdot\cos\alpha\cdot P_x^\odot+\Lambda\cdot\sin\alpha\cdot P_y^\odot)], \quad (1.9)$$

where the x and y subscripts in the P_x, $P_x^\odot$, P_y, $P_y^\odot$ notations refer to the x and y coordinates defined in Section 6.1. The polarization observables were determined by measuring angular dependent yields for different combinations of beam helicity and target polarization states.

1.5 A $\gamma p \to \pi\pi N$ Reaction Model

In addition to the theoretical models already discussed, which predict the existence of baryon resonances and calculate the nucleon resonance mass, there are also reaction models that take into account particular baryon resonances and perform calculations that provide cross sections for different channels and consequently they predict the specific observables associated with these channels.

The γN$\to$ $\pi\pi$N model [11] used in this analysis provides the theoretical predictions for the polarization observables extracted. This model uses different diagrams for $\gamma N \to \pi\pi N$ process as shown in Fig. 1.6, where one can see that the model includes besides the N and Δ-Born terms also three resonance terms. The

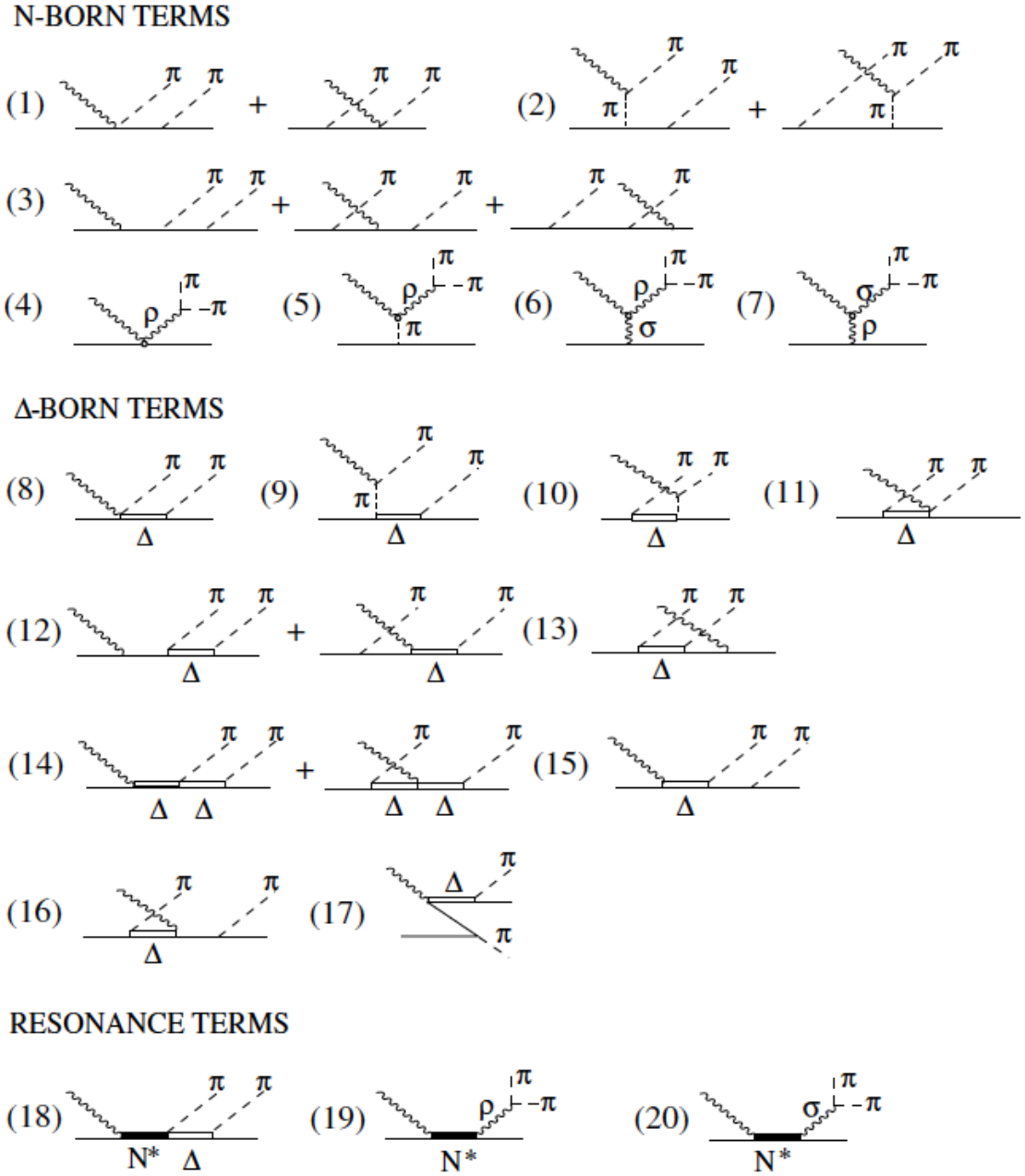

Figure 1.6: Diagrams for $\gamma N \to \pi\pi N$ reaction channel depicting which N-Born terms, Δ-Born terms, and resonance terms enter the model calculation. Figure taken from [11].

nucleon resonance could decay in three different ways: $\gamma N \rightarrow N^* \rightarrow \Delta\pi \rightarrow \pi\pi N$, $\gamma N \rightarrow N^* \rightarrow p\rho \rightarrow \pi\pi N$, and $\gamma N \rightarrow N^* \rightarrow p\sigma \rightarrow \pi\pi N$, which means that the nucleon resonances could decay through intermediate excited states or it could return directly to the ground state. The nucleon resonances included in the model are $\Delta(1232)$, $N(1440)$, $N(1520)$, $N(1535)$, $\Delta(1620)$, $N(1675)$, $N(1680)$, $N(1700)$, and $N(1720)$; and as seen in parentheses they are localized in the mass region up to 1.8 GeV. Also the model includes mesons like ρ and σ, and the calculation is taking as an input the 4-momenta of the incoming photon, proton, recoil proton and pions, and following a Lagrangian approach determines the differential cross sections in the center of mass frame, together with the polarization observables pertaining to this channel. The differential cross section is proportional to the sum of the squares of the all reaction amplitude terms which are included in the model (see Fig. 1.6). The results of the model calculation were compared to the experimental data (see Section 6.2) and one can notice a lack of agreement between the data and the model prediction, which will lead to further constraining the model for a closer agreement.

1.6 Existing Data For Double-Charged Pion Channel

Cross Section Determinations and Production of ρ^0 and Δ^{++} In the Reaction $\gamma p \rightarrow p\pi^+\pi^-$

This photoproduction experiment used a linearly polarized monoenergetic photon beam [12], with photon energy values of 2.8 GeV and 4.7 GeV. The channel cross sections were determined together with nine density-matrix elements for the $\gamma p \rightarrow \Delta^{++}\pi^-$ channel. It has been shown that this channel was dominated by ρ^0 and Δ^{++} production, and the ρ_0 cross section was determined by using the Söding model. Figure 1.7 shows the invariant mass $M_{\pi^+\pi^-}$ for different intervals of the momentum-transfer-squared to the proton and one can notice an agreement of the ρ^0 mass shape

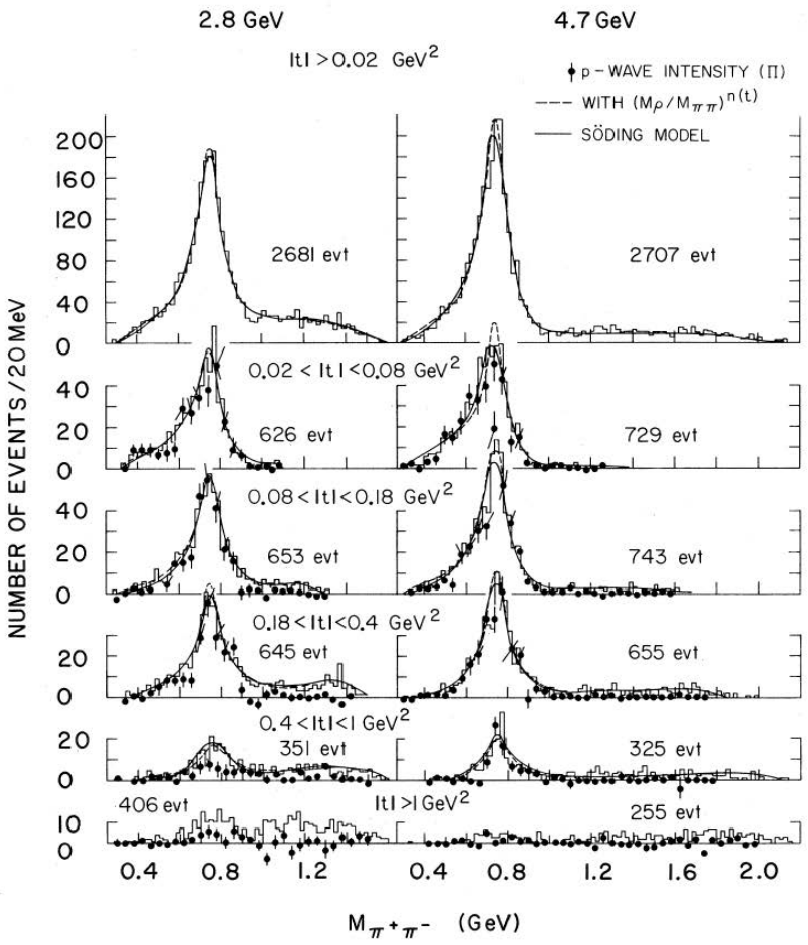

Figure 1.7: $\pi^+\pi^-$ mass distribution, where the dashed curves give the results of maximum-likelihood fits to the channel and the solid curve represents the Söding model [13]. One can see that the ρ^0 is not located at the accepted ρ^0 mass and changes as a function of t. Figure taken from [12].

with the Söding model [13].

Total Cross Section Measurement For Three Double Pion Photoproduction Channels On The Proton

The three double pion channels analyzed were $\gamma p \to p\pi^0\pi^0$, $\gamma p \to n\pi^+\pi^0$, and $\gamma p \to p\pi^+\pi^-$ and the photon energy was ranging from 400 MeV to 800 MeV. Data collection took place at the tagged-photon-beam facility of the MAMI microtron at Mainz and used the large acceptance hadronic detector DAPHNE. Figure 1.8 shows the total

cross sections versus E_γ for the $\gamma p \to p\pi^+\pi^-$, $\gamma p \to p\pi^0\pi^0$, and $\gamma p \to n\pi^+\pi^0$ channels and the data are compared to model predictions [14]. The continuous lines are the predictions of the Murphy and Laget model [15] and the dashed curve represents the prediction of the Tejedor and Oset model [16].

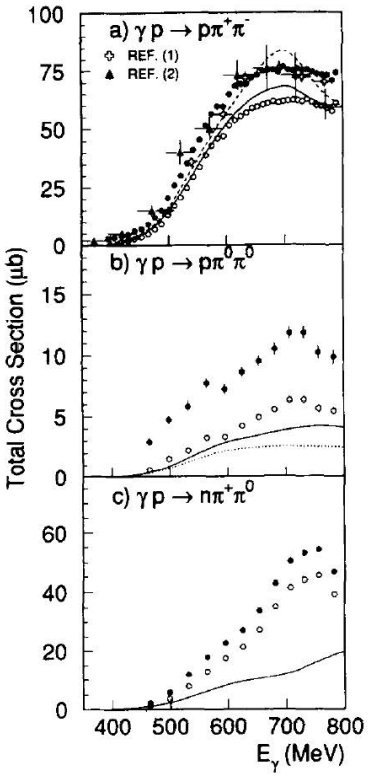

Figure 1.8: Total cross sections for the three double-pion photoproduction channels, where the open circles represent the cross sections measured in DAPHNE, compared to model predictions. Figure taken from [14].

Photoproduction of the ρ^0 Meson on the Proton at Large Momentum Transfer

Data have been measured over a momentum transfer range from $0.1 - 5.0$ GeV^2 using CEBAF Large Acceptance Spectrometer (CLAS) at Thomas Jefferson National Accelerator Facility [17]. The differential cross section for ρ^0 meson photoproduction above the resonance region was measured and compared with different theoretical models as shown in Fig. 1.9. In order to extract the ρ^0 channel from the measured

two-charged pion cross sections the fitting of the $\pi^+\pi^-$ and $p\pi^+$ invariant masses was performed and the indication was that the agreement with the model is better when quark exchange mechanisms are introduced to the calculation of the ρ^0 production.

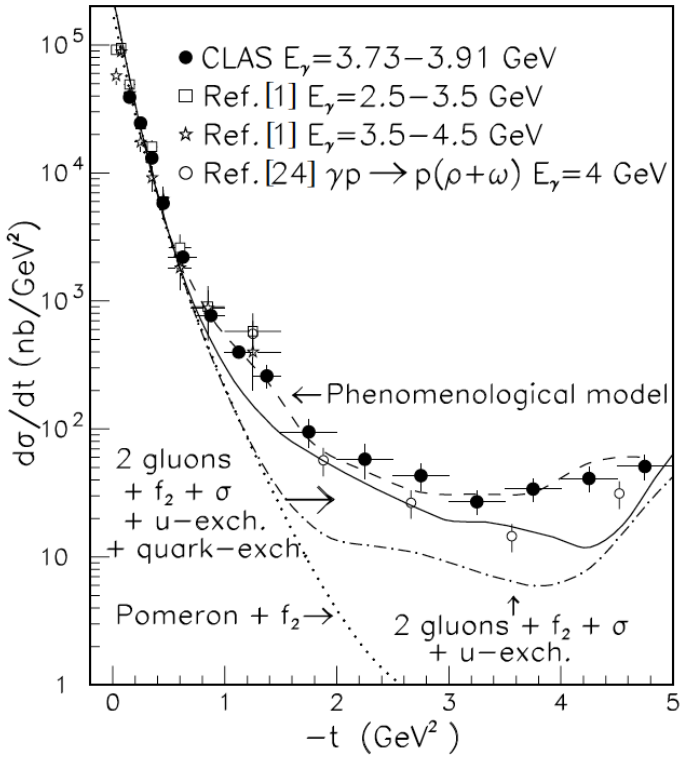

Figure 1.9: Differential cross section for ρ^0 photoproduction, where the black dots are CLAS data, empty rectangles and stars represent previous measurements from Ref. [18] and the empty stars represent previous measurements from Ref. [19]. The dot-dashed line represent a QCD-inspired model, the dashed line depicts the phenomenological model used for the channel separation, the dotted line the Pomeron and f_2 Regge trajectory exchange, and the solid line the full model calculation. Figure taken from [17].

Photoproduction Of ρ^0-mesons And Δ-baryons In The Reaction $\gamma p \rightarrow p\pi^+\pi^-$ At Energies Up To 2.6 GeV

The data were measured at the electron stretcher ELSA with the SAPHIR detector at Bonn University, Germany [20] and the total and differential cross sections were determined as shown in Fig. 1.10 and 1.11. One could see an increasing discrepancy

between data and models above the ρ^0 threshold due to the simplistic modeling of ρ^0 production.

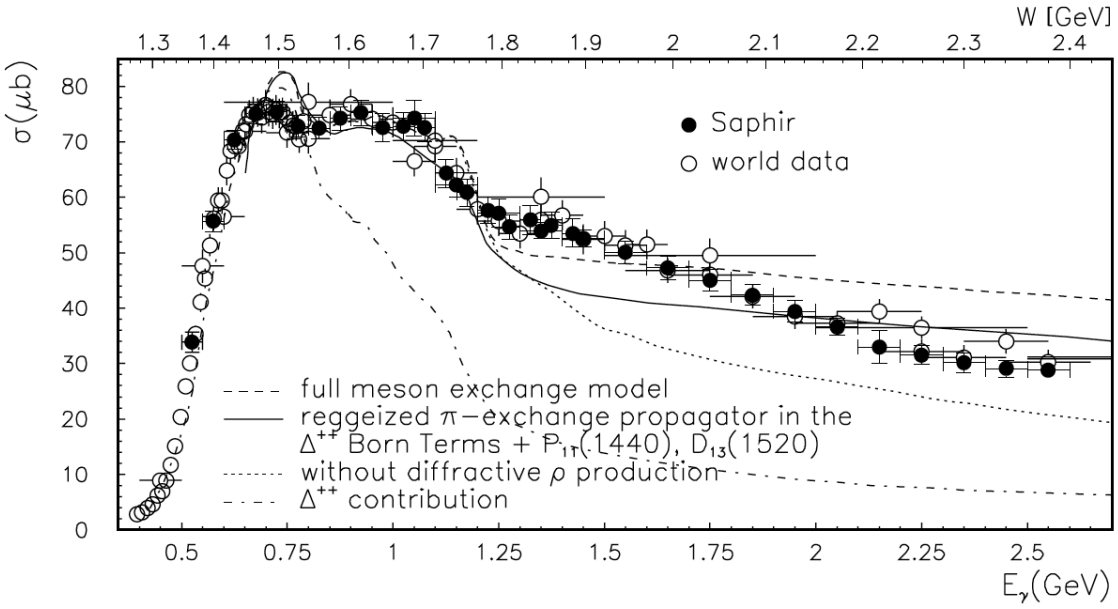

Figure 1.10: Results for the total cross section of the reaction $\gamma p \to p\pi^+\pi^-$ showing the Saphir data as full circles and the world data as empty circles. The data were compared to different theoretical models as illustrated. Figure taken from [20].

Beam-Helicity Asymmetries in Double Pion Photoproduction On The Proton

The experiment was performed at Thomas Jefferson National Accelerator Facility with CEBAF Large Acceptance Spectrometer using circularly polarized photons in the energy range between 0.5 GeV and 2.3 GeV on unpolarized hydrogen target. First time comprehensive measurements of the beam-helicity asymmetry were reported as shown in Fig. 1.12 [21]. As illustrated, the comparison to the model calculations shows a discrepancy, which is due to the insufficiency of the theoretical models.

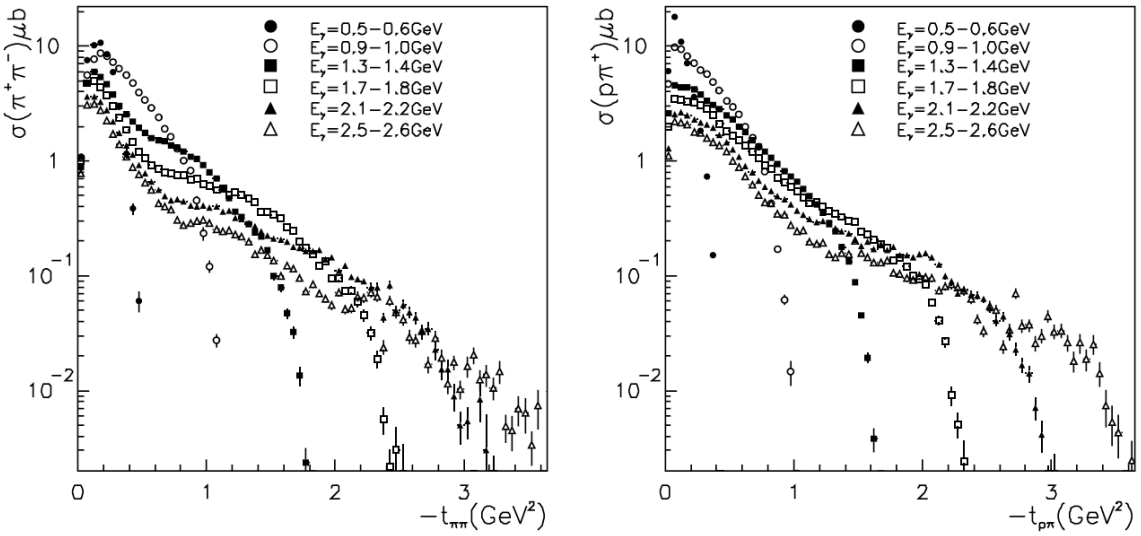

Figure 1.11: Results for the differential cross section of the reaction $\gamma p \to p\pi^+\pi^-$ for different photon energy ranges E_γ. Figure taken from [20].

Beam-Helicity Asymmetries in Double-Pion Photoproduction off the Proton

Beam-helicity asymmetries were extracted at MAMI accelerator in Mainz for $\gamma p \to \pi^+\pi^0 n$, $\gamma p \to \pi^0\pi^0 p$ and $\gamma p \to \pi^+\pi^- p$ channels using a circularly polarized photon beam and a liquid hydrogen target [23]. The results presented in Fig. 1.13 shows a relatively good agreement with the model prediction for the photon-energy bin between 700 and 730 MeV, but lacks a good agreement in the other bins.

Recently completed and ongoing Jefferson Lab analyses

At Jefferson Lab, there are completed and ongoing analyses of the double-pion photoproduction experiments, which have targeted the extraction of 15 polarization ob-

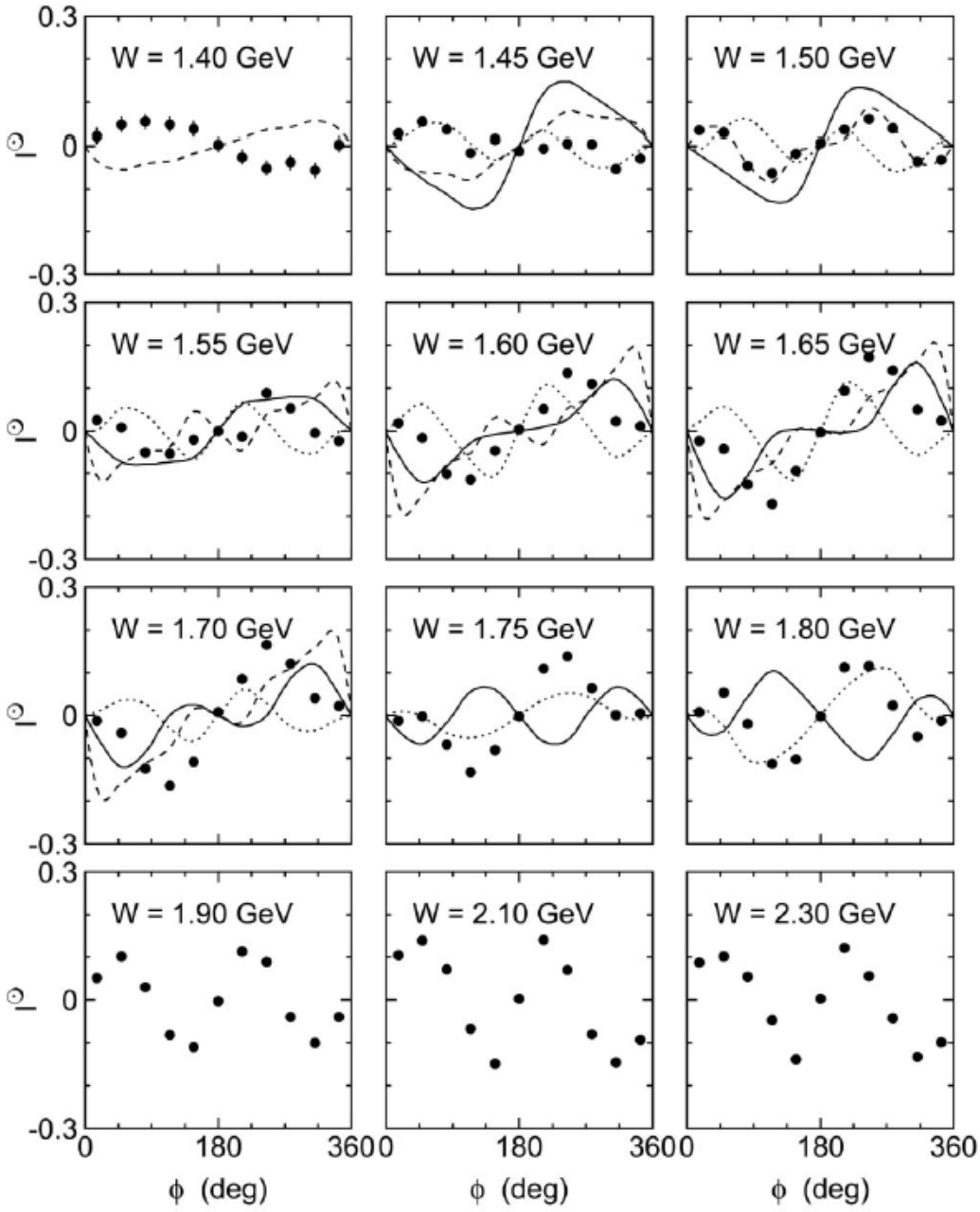

Figure 1.12: CLAS data $\gamma p \to \pi^+\pi^-$ (full circles) for the beam helicity asymmetry angular distribution in the center of mass energy range from 1.4 GeV to 2.3 GeV compared to the calculations by Mokeev et al. [22] (solid and dotted curve) and to calculations by Fix and Arenhövel (dashed curve) [11]. Figure taken from [21].

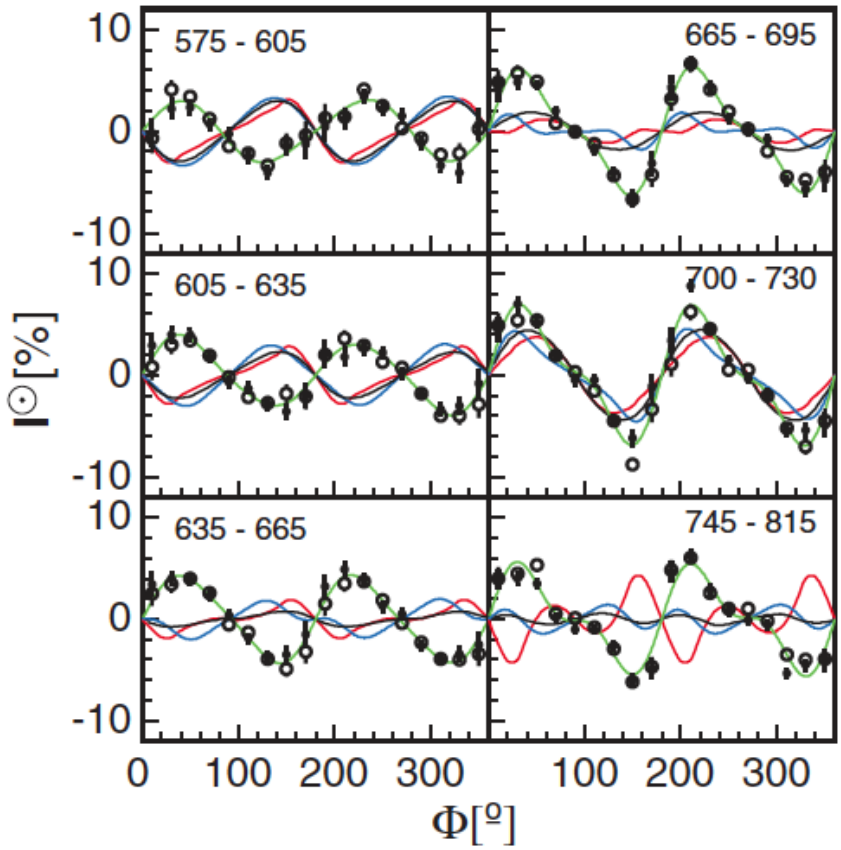

Figure 1.13: The MAMI experimental data for $I^{\odot}$ in 6 bins of photon energy corresponding to the $\gamma p \to \pi^+\pi^- p$ channel, where the filled circles represent $I^{\odot}(\Phi)$ data, the empty circles represent $I^{\odot}(2\pi - \Phi)$ data, the green curve is an odd function fitted to the data and the red, blue, and black curves represent model predictions [11, 24]. Figure taken from [23].

servables corresponding to different combinations of target- and beam-polarization orientations as shown in Table 1.2. The experiment g9a involves a longitudinally polarized target and g9b experiment a transversely polarized target and data were measured with a linearly polarized beam, and a circularly polarized beam.

Table 1.2: The beam- and target-polarization observables in double-pion photoproduction.

	Transverse Target Polarization	Longitudinal Target Polarization	Unpolarized Target
Linearly Polarized Beam	P_x^S, P_y^S, P_x^C, P_y^C	P_z^S, P_z^C	I^S, I^C
Circularly Polarized Beam	$P_x^\odot$, $P_y^\odot$	$P_z^\odot$	$I^\odot$
Unpolarized Beam	P_x, P_y	P_z	I_0

Chapter 2

The Experiment

2.1 Overview

The data for this analysis were taken at the Thomas Jefferson National Accelerator Facility (JLab), located in Newport News, Virginia. The main research facility of the laboratory is the Continuous Electron Beam Accelerator Facility (CEBAF) [25], which consists of a polarized electron source, an injector, and a pair of superconducting linear accelerators. Figure 2.1 presents the aerial view of the JLab facility, and also depicts the full orbit of the beam line that splits in the four halls: A, B, C, and D, where spectrometers record the data resulted from the collisions between the beam and stationary targets. The Hall B physics program used the CEBAF Large Acceptance Spectrometer also called CLAS. The data for this work came from FROST g9b experiment, which involved a transversely-polarized butanol target, with a circularly-polarized photon beam and center of mass energies varying from $W = 1450$ MeV to 2550 MeV. The g9b data acquisition lasted from March 18th to August 12th 2010 recording data for a set of 10 different run groups. Figure 2.2 shows a schematic lateral view of the experimental setup, whose main components are discussed in this chapter. Recently, an upgrade of the beam energy from 6 to 12 GeV took place at JLab and this will allow new data to be recorded and thus will deepen even more the present understanding of hadron properties and hadron dynamics.

Figure 2.1: Aerial view of Jefferson Lab, where in dashed red depicts the beam line and the red circles represent the locations of the experimental halls. Figure taken from [26].

2.2 Photon Beam

First a longitudinally polarized electron beam was generated by a circularly polarized laser beam striking a photocathode at a frequency of 499 MHz and as a result bunches of electrons separated by 2 ns were produced. The longitudinally-polarized electron beam with an incident energy of E_e= 3081.73 MeV hit a thin target (the "Bremsstrahlung-radiator") just upstream from a magnetic spectrometer called the "tagger", and produced a circularly polarized photon beam (Fig. 2.3).

The tagger spectrometer had a maximum magnetic field of 1.75 T which was produced by a dipole magnet. This magnetic field deflected the electron away from

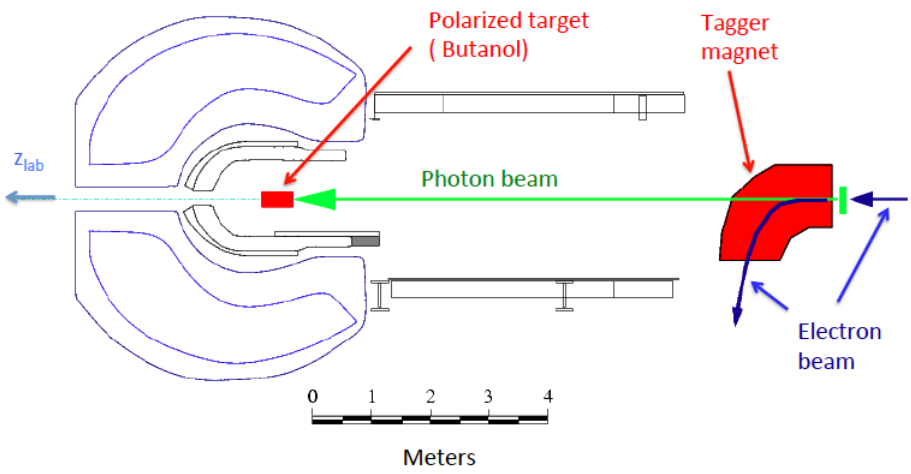

Figure 2.2: CLAS and TAGGER systems in Hall B at JLab, showing the location of the tagger, the photon beam trajectory, and the target position inside the CLAS detector. Figure taken from [27].

the beam line and towards the electron beam dump. Before being dumped, the electron beam passed through the E-counters, which consist of 384 scintillators paddles overlapping and forming the E-plane which together with the magnetic field of the tagger assisted in determining the final electron energy E'_e. The E-counters provide an energy resolution of $0.001E_0$ [29]. Next, the electron passed through the T-counters which were 61 scintillators forming a T-plane located 20 cm behind the E-plane, which helped determining the electron beam time with a time resolution of 300 ps or better. After determining the energy of the electron before and after interacting within the radiator, the photon energy was calculated,

$$E_\gamma = E_e - E'_e. \tag{2.1}$$

Any photons emitted in the radiator passed straight through the magnetic field of the tagger magnet and were collimated before the photoproduction reaction took

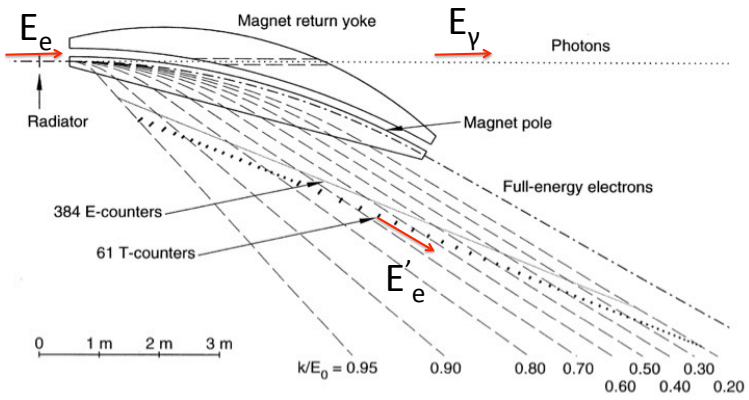

Figure 2.3: Tagging system at JLab. Figure taken from [28].

place. The energy of the photon beam ranges between 20% and 95% of the energy of the incident electron beam and its value is under 3 GeV. The degree of the photon beam polarization depends on the electron beam polarization P_e and to determine P_e a Møller polarimeter was used as discussed in Section 2.9. The expectation is that the electron beam polarization stays constant during the data collection and Table 2.1 shows that during six different measurements the values stayed relatively constant within the statistical uncertainty and their weighted average $\bar{P}_e = 87.3 \pm 0.6$ was used in this analysis to determine the degree of photon beam polarization. The mathematical expression for the degree of photon beam polarization $\delta_\odot$ is given by [30]

$$\delta_\odot = \bar{P}_e \frac{\frac{4E_\gamma}{E_e} - \left(\frac{E_\gamma}{E_e}\right)^2}{4 - \frac{4E_\gamma}{E_e} + 3\left(\frac{E_\gamma}{E_e}\right)^2}, \tag{2.2}$$

where $\bar{P}_e$ is the weighted average of the electron beam polarization as discussed before, E_γ is the photon energy and the E_e is the electron beam energy equal to 3081.73 MeV. The beam helicity was flipped between $+1$ and -1 at a frequency of 30 Hz or 240 Hz. Additionally, inserting a half-wave plate (HWP) in the laser beam was used to flip

Table 2.1: Møller measurements for g9b data runs [31].

Run Number	P_e [%]
62530	88.1 ± 1.5
62530	86.5 ± 1.4
62704	86.8 ± 1.4
62704	86.9 ± 1.3
63525	88.6 ± 1.5
63594	87.1 ± 1.5

the electron-beam helicity. The asymmetry between the number of electrons with positive helicity and the number of electrons with negative helicity, called *beam charge asymmetry* was measured to be $< 0.01\%$ [31].

2.3 Targets

For the g9b FROST (Frozen Spin Target) experiment (Fig. 2.5), three different targets were used: polarized butanol target ($L = 5$ cm, $\phi = 1.5$ cm and $m = 5$ g) [32], unpolarized carbon target ($L = 0.15$ cm, located 6 cm from CLAS center), and unpolarized polyethylene target ($L = 0.35$ cm, located 16 cm downstream from CLAS center). The constituents of the butanol target (C_4H_9OH) are 10 free protons (10 hydrogen atoms) and 64 bound nucleons and they represent the source for the signal and background events in this analysis. The carbon and polyethylene targets are unpolarized and consist of bound nucleons, generating events that mimic the background events from the butanol target. The butanol target was built by doping butanol with a highly stable solid material called TEMPO ($C_9H_{18}NO$) and before freezing, water was added (0.5 % by weight) to avoid the formation of a crystalline solid. To obtain beads of 1-2 mm in diameter the solution was dripped through a small diameter needle into liquid nitrogen. Then a 50 mm long PCTFE($(C_2ClF_3)_n$) target cup was filled with 5 g of beads. The free protons of the butanol target were polarized through

dynamic nuclear polarization (DNP) by using a homogeneous magnetic field (referred to as NMR magnetic field) of 5 T. The target was cooled to a temperature of 0.5 K, polarized through DNP, and then, in order to preserve the polarization orientation of the polarized nucleons, the target temperature was reduced to 30 mK and a holding magnetic field of 0.5 T was applied to maintain the polarization direction. The target polarization orientation was chosen to be transverse to the beam direction (z direction in the lab frame or photon beam direction in CLAS). The relaxation time of the polarized protons is a function of magnetic field and the temperature and its value was approximately 2700 hours (with beam) for the positive target polarization ($116.3^\circ \pm 1.4^\circ$ from the x-axis in the lab frame [33]) and 1400 hours (with beam) for the negative target polarization ($296.3^\circ \pm 1.4^\circ$ from the x-axis). Since the target polarization loss per day is between 1% and 1.5%, the polarization varies within a run group as shown in Fig. 2.4. Every 5-7 days during data collection the target was repolarized and the orientation was flipped by 180° in order to reduce systematic uncertainties. Table 2.2 gives the target-polarization range for each run group.

On July 2nd, 2010, during the running time, the target magnet quenched because of a power surge caused by a power loss in Hall C. Due to this unfortunate situation, the running time was postponed for three weeks and the data collected afterwards included the five run groups whose number ranged from 63508 to 63598 (Table 2.2). Since these data were associated with much lower target polarization and statistics, the choice was to exclude them from this analysis.

2.4 CLAS Detector

The CLAS spectrometer [28] was used for detecting the particles produced during the interactions of the photon beam with the target situated at the center of the detector and covered almost the entire 4π solid angle. The coverage in the azimuthal angle was $8^\circ < \phi < 145^\circ$ and for the polar angle was $-25^\circ < \theta < 25^\circ$. CLAS (Fig. 2.6) was

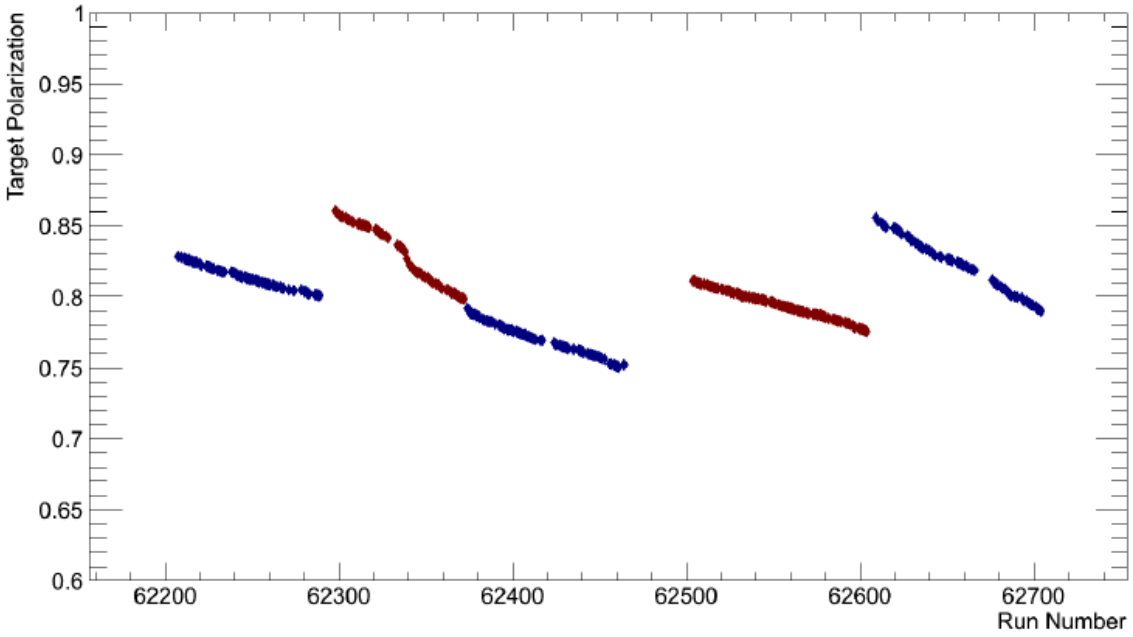

Figure 2.4: Target polarization versus run number for the g9b experiment with circularly polarized beam. The blue data points are for runs with positive target polarization and the red data points are for negative target-polarization runs. Figure courtesy of Hao Jiang [33].

composed of a start counter (ST) located close to the target and providing a precise start time of the particle trajectory, drift chambers (DC) that measure the trajectory of the charged particles, scintillation counters (SC) for time-of-flight measurement that provided track timing information needed in particle identification, Cherenkov counters (CC) helpful in separating electrons from pions (but were not used for the g9b experiment) and electromagnetic calorimeter (EC) for measuring the energy of electrons, photons, and neutrons, also not used in this experiment.

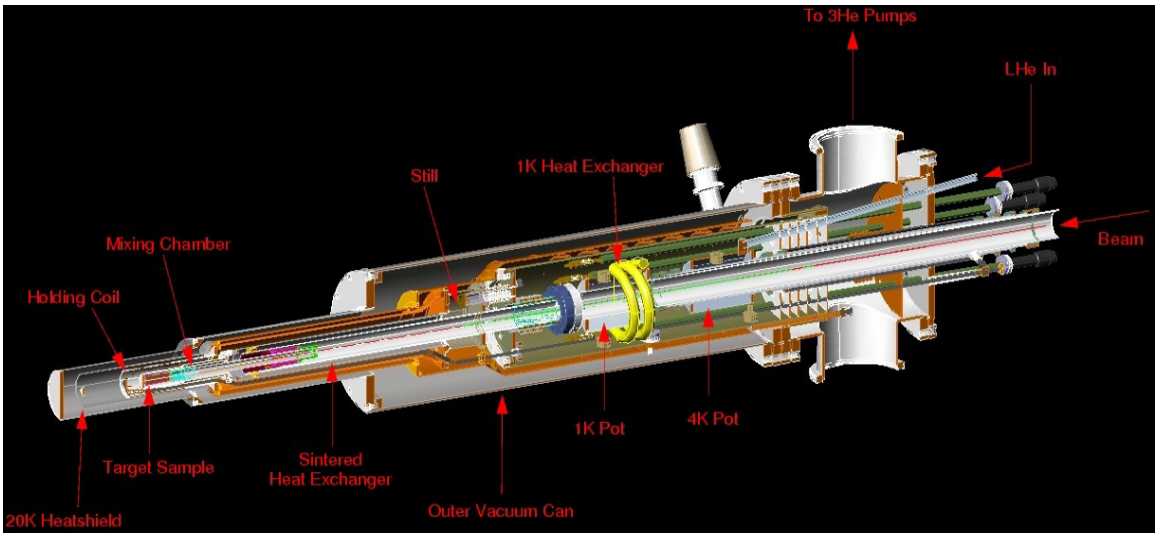

Figure 2.5: FROZEN spin target setup used in g9b experiment. Figure taken from [34].

2.5 Torus Magnet

An important component of the CLAS detector is the torus magnet [28] (5 m in diameter and 5 m in length), which provided the magnetic field used in the kinematic analysis of the charged particles. The structure of the torus magnet consists of six superconducting coils distributed around the beam line. Since there is no iron core present the magnetic field was determined by using the current through the coils. Figure 2.7 displays the geometry and the magnitude of the magnetic field contours. Due to the kidney-shape of the coil, the space at the center of the torus is free of magnetic field (Fig. 2.8), which allowed the use of a polarized target at that location. The direction of the magnetic field is mainly in the ϕ direction and points

Table 2.2: Circular polarization data runs for g9b experiment, showing that the electron beam energy $E_e = 3,081.73$ MeV stayed constant. The signs notations $(++)$, $(-+)$, $(--)$, $(+-)$ stand for different combinations of (NMR magnetic field sign, Holding magnetic field sign).

Run range	Events	Beam energy	Beam current	Helicity frequency	Target polarization
$62207 - 62289$	723.1 M	3081.73 MeV	11.9 nA	240 Hz	83% - 80% $(++)$
$62298 - 62372$	894.9 M	3081.73 MeV	13.4 nA	240 Hz	86% - 80% $(-+)$
$62374 - 62464$	1129.7 M	3081.73 MeV	13.4 nA	240 Hz	79% - 75% $(++)$
$62504 - 62604$	1307.1 M	3081.73 MeV	13.6 nA	240 Hz	81% - 76% $(+-)$
$62609 - 62704$	972.6 M	3081.73 MeV	13.5 nA	240 Hz	85% - 79% $(--)$
$63508 - 63525$	138.2 M	2265.99 MeV	10.7 nA	943 Hz	77% - 58% $(++)$
$63529 - 63542$	166.8 M	2265.99 MeV	8.3 nA	240 Hz	56% - 57% $(+-)$
$63543 - 63564$	321.7 M	2265.99 MeV	13.3 nA	943 Hz	74% - 61% $(++)$
$63566 - 63581$	249.6 M	2265.99 MeV	13.2 nA	943 Hz	70% - 64% $(+-)$
$63582 - 63598$	242.3 M	2265.99 MeV	13.3 nA	240 Hz	48% - 46% $(+-)$

anti-clockwise (for positive magnet current) around the beam line when observed from upstream, but close to the coils there are deviations from this preferential orientation. Positively charged particles entering the magnetic field of the torus were deflected away from the beam line and negatively charged particles were deflected toward the beam line. The coils were made out of four layers of 54 turns of aluminum NbTi/Cu conductor and they were cooled to 4.5 K by circulating helium through cooling tubes adjacent to the coils. The maximum design current was 3860 A which corresponds to a magnetic field of 2.5 T for forward angles and 0.6 T at 90°. The current used for g9b was +1920 A. The momentum of a charged particle was found after determining the curvature of the particle's track through the magnetic field of the torus, which was apriori known.

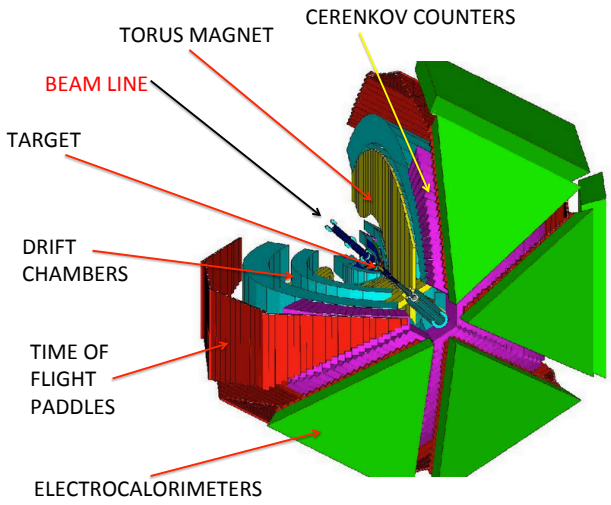

Figure 2.6: CLAS detector at JLab. Figure taken from [35].

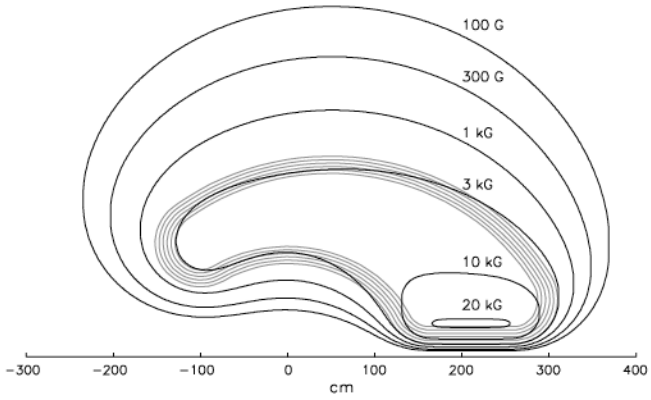

Figure 2.7: Contours of the magnetic field of the torus created in the midplane between two coils, where at the contour line of 3 kG one could see the position of the kidney-shape coil shown as a multiple wrapping. Figure taken from [28].

2.6 Start Counter

The start counter [36] as shown in Fig. 2.9 was the first detector component to "see" the particles, which emerged from the interaction of the photon beam with the target material. ST counter was made out of 24 paddles (EJ-200 brand) surrounding the target cell and distributed in 6 sectors with 4 paddles per each sector (Fig. 2.9)

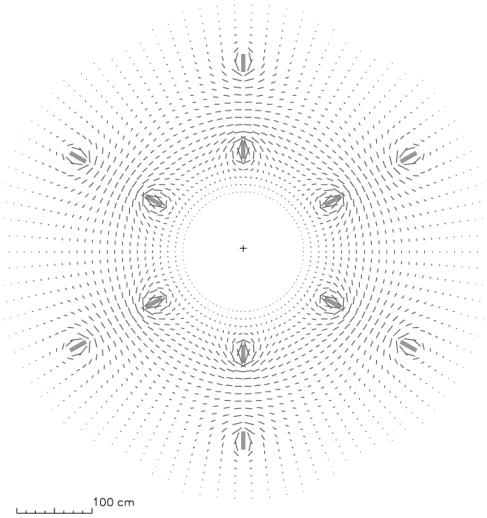

Figure 2.8: Magnetic field vector field transverse to the beam in a plane centered at the target. The length of each segment is proportional to the strength of the field at that point. One can notice the six coils in cross-section and at the center one can clearly observe that there was a space free of magnetic field (where the polarized target was placed). Figure taken from [28].

covering the entire azimuthal angle and a polar angle range $10^\circ \leq \Theta \leq 140^\circ$. In order to identify the photon that initiated the reaction a comparison is made between the tagger time and the start counter time (see Section 3.1). The particle detection is possible because when the particles passed through the start counter paddles, photons were generated through ionization and these photons were collected by the photomultipliers mounted on the paddles. The time resolution of the start counter was approximately 250 ps, which was sufficiently accurate to allow the photon identification.

2.7 Drift Chambers

After the start counter, the next type of CLAS components were the drift chambers [37], which served in tracking the charged particles moving under the influence of the magnetic field of the torus and as result the momentum of these charged particle was reconstructed. From the curvature of the track the momentum and the

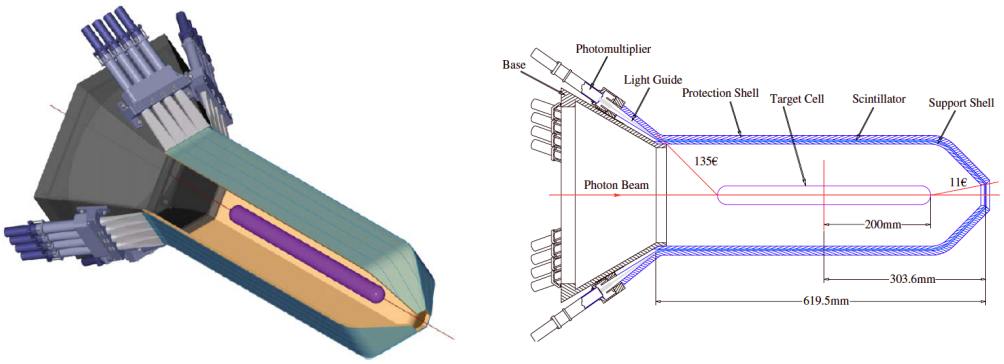

Figure 2.9: Overall view of the Start Counter (left) and the cross-section of the Star Counter (right). Figure taken from [36].

sign of the charge of the particle were extracted. Figure 2.10 shows the three radial locations of the drift chambers: Region 1 chambers surround the target in the low magnetic field, Region 2 chambers are situated between the magnet coils in high magnetic field and Region 3 chambers positioned outside the magnetic coils. Region 1 chambers tracked all charged particles before they entered the magnetic field of the torus, Region 2 chambers tracked all charged particles in the magnetic field of the torus and Region 3 chambers monitored the field-free region outside the torus at a distance between 3 and 3.5 m away from the target. Inside the drift chambers there was a wire arrangement composed of field wires (at high negative potential) and sense wires (at high positive potential). The drift chamber gas was a mixture of 90% argon and 10% carbon dioxide and when the charged particles passed through they caused the ionization of the gas. The electrons resulted from the ionization drifted to the sense wires and created a current through the wire. The angular coverage of the drift chambers was 80% in the azimuthal direction and between 8° and 142° in polar angle and the reconstructed momentum resolution was $\leq 0.05\%$ for 1 GeV/c charged particles and the resolution for θ, ϕ was ≤ 2 mrad [37].

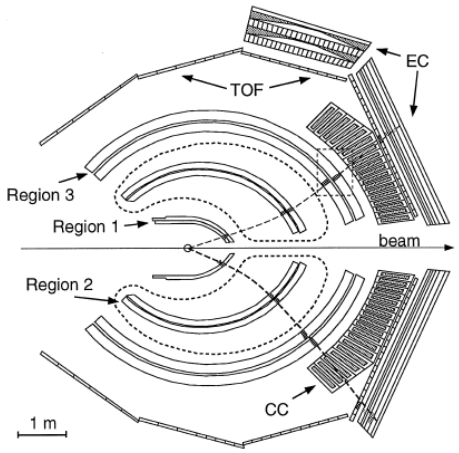

Figure 2.10: Horizontal cut through CLAS detector at the beam line elevation, showing the Region 1, Region 2, and Region 3 chambers. The dotted curves show the trajectories of two particles crossing the drift chambers. The position of detector components like Cherenkov counters (CC), calorimeters (EC) and time of flight counters (TOF) are pictured also together with the dotted contours showing the projection of the torus coils on the sector mid-plane. Figure taken from [37].

2.8 Time Of Flight Counters

After drift chambers, the next detector components were the time-of-flight counters [38], covering a 206 m^2 with lengths varying from 32 cm to 450 cm, which assisted in the event timing of the particles. The scintillator material consisted of Bicron $BC-408$, which had the desirable characteristics like fast time response and low light attenuation. These counters measured the time-of-flight, which was used in the particle identification process due to the good time resolution they provided. The time-of-flight counters permitted the separation of pions and kaons up to momenta of 2 GeV/c, with a time resolution of 120 ps for small angles, and 250 ps at large angles. The geometrical arrangement of these counters formed four sided panels in each of the six sectors as shown for one sector in Fig. 2.11. Each sector has 57 scintillators with a photomultiplier at each end. The TOF scintillators are located at a distance of approximately 5 m away from the target, where the magnetic field strength is less

than 10 G at the position of the forward-angle PMTs and 30 G at large-angle PMTs.

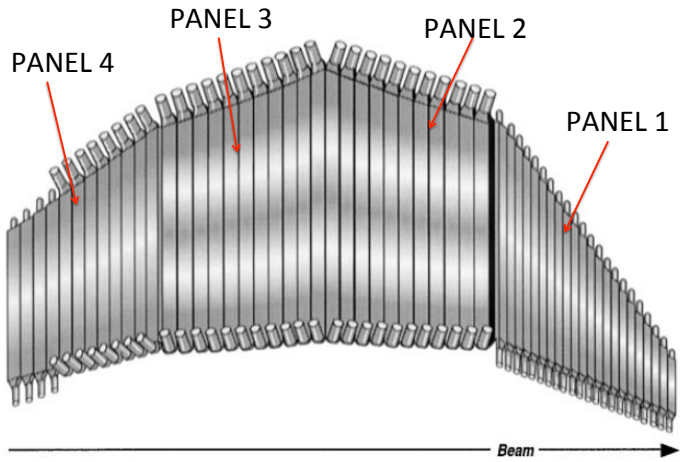

Figure 2.11: TOF scintillators for one sector, where starting from the right the first 23 scintillators form Panel 1 and this panel measured forward going particles, while Panels 2, 3, and 4 cover large angles. Figure taken from [38].

The charged particles emitted by the target material passed through the drift chambers and hit the TOF scintillators, exciting the counter material and causing it to emit photons which travelled to the end of the scintillator bar and then reached the PMTs, which converted the light into an electric current that was measured by their anode. The hit time from TOF paddles together with the event start time provided by the ST counters and the path measured via DC counters served in determining the speed of the particle.

2.9 Beam Line Devices

During this experiment a couple of devices were used to monitor the status of the electron beam, photon beam and target polarization and these are discussed in this section.

Electron beam position monitors (BPMs)

During photon beam experiments (like g9b FROST), two BPMs checked the position

and the direction of the electron beam, and the BPMs were located upstream from the target at 36.0 and 24.6 m [28]. Their role was to determine the x and y positions of the beam at each of the locations and this information was used via a feedback loop in order to keep the beam centered on the target. A typical electron beam profile in the x-direction just upstream of the tagger magnet, after being fitted with a Gaussian function, had a sigma of 73 μm.

Harps

To measure the electron beam profile, thin wires were moved through the beam by devices called **harps** and after the wires scattered the electrons of the beam, these electrons were counted by PMTs [28]. The beam profile is the distribution of the PMT counts versus x and y position of the wire. These beam profiles were checked every time a change occurred and affected the electron beam.

Møller polarimeter

The Møller polarimeter is measuring the asymmetry in elastic electron-electron scattering to determine the polarization of the electron beam. The Møller polarimeter was installed in Hall B just upstream from the tagging system and consisted of a target chamber, two quadrupole magnets and two detectors [28]. The electrons were deflected by the magnetic field of the system and an asymmetry was measured between the electrons entering the two detectors, in order to determine the polarization of the electron beam. The statistical uncertainty from a Møller measurement was about 1%, the systematic uncertainty of the measurement was 3%.

2.10 Event Triggering And Data Acquisition System (DAQ)

Event triggering is the process of selecting only the events of choice that are stored for later processing. Triggering has two roles: to tell DAQ to read out data and to filter unwanted events. There are two main levels of CLAS event triggering [28]: level

1 triggering depends on the fast detectors (e.g. start counters) and level 2 triggering is based on the slower detectors (e.g. drift chambers). The readout process includes TDC (time to digital), ADC (analog to digital) converters and scalars for counts. The CLAS data acquisition system converts the detector signals (analog signals) into a digital format and these data are stored in order to be used later in an analysis. DAQ system is able to read out events that come at a rate of between 3 and 4 kHz and the busy (dead) time was between $15\% - 20\%$, which means that during this time no other event could have been recorded. The data output rate is 25 MByte/s and the event size was between 3 and 5 kB. The sum of all the events recorded during the FROST experiment is over 10 billion events, which means more than 30 TB of data recorded on the JLab data storage silo. These raw data were converted to physical quantities like time, energy, mass through a process called **cooking**, but prior to achieving this, every detector system had to be individually calibrated. The Catholic University of America group performed the calibration for the tagger and time of flight system and the cooking of g9b data. Idaho State University group calibrated the start counter and Florida State University group calibrated the drift chamber system and University of South Carolina group calibrated the target polarization used during g9b FROST experiment. The parameters obtained from detector calibration were used by the cooking software package and the result of this processing was a set of data files that contain all the physical quantities ready to be used in the next step of the analysis, as discussed in the following chapter.

Chapter 3

Event Selection

The $\vec{\gamma}\vec{p} \to p\pi^+\pi^-$ channel has three particles in the final state (one proton, one positive pion, and one negative pion) and this chapter discusses the particle identification process and the corrections applied in this analysis.

3.1 Photon Selection

As mentioned before the electron beam structure consisted of electron bunches produced at 2 ns time intervals and this determined the photon beam to have the same structure. There were many photon candidates, which could have triggered a given event. To determine the photon which initiated the event, the coincidence time Δt was calculated as

$$\Delta t = t_{CLAS,vertex} - t_{\gamma,vertex} = t_{ST} - \frac{d_{ST}}{c \cdot \beta_{calc}} - \left[t_{TAGR} + \frac{Z}{c}\right], \tag{3.1}$$

where

t_{ST} is the time measured when a given particle hit the ST paddles,

d_{ST} is the particle's path measured from the reaction vertex to the ST paddles,

$\beta_{calc} = \frac{p}{\sqrt{p^2+m^2c^2}}$,

where p is the measured momentum and m is the mass of the particle,

t_{TAGR} is the photon time measured by the tagging system,

Z is the Z-vertex of the particle and c is the speed of light.

To further explain, the coincidence time is the difference between the times provided by two different detectors, and in this analysis is the time difference between

the CLAS vertex time and tagger vertex time, where CLAS vertex time is the time corresponding to a given particle, whereas the tagger vertex time corresponds to a given photon. The CLAS vertex time $t_{CLAS,vertex}$ equals the difference between the start counter time t_{ST} (recorded by the ST scintillators with respect to the global start time) and the time needed for the particle to get from the event vertex to the ST counters, which is $\frac{d_{ST}}{c \cdot \beta_{calc}}$. The other time used in calculation was the tagger vertex time $t_{\gamma,vertex}$, which was the time needed by the photon to arrive at the center of the target plus the Z/c time needed to travel from the target center to the Z vertex. The coincidence time Δt needs to be centered around zero. Once the coincidence time Δt between each detected particle of a given event and a particular photon was calculated, ***the photon which triggered the event was chosen to be the one which gave the smallest coincidence time for all detected particles of that event***. Additionally, a later cut was applied to the coincidence time so that only events associated with photons within ± 1 ns window are kept (Fig. 3.1) due to the 2 ns bunch structure of the photon beam.

3.2 Reaction Vertex

Another selection was performed on the Z-vertex, to make sure that the particles came from within the butanol, carbon, or polyethylene targets. The butanol target was positioned at the center of CLAS detector along z-axis where $Z = 0$ and the selected butanol events fall between (-3 cm,$+3$ cm) cut along the Z-vertex as shown in Fig. 3.2, the carbon events are found between 6.5 cm and 11 cm, while the polyethylene events are in the range of Z-vertex from 14 cm to 18 cm. Figure 3.3 shows the cut for the X-vertex and Y-vertex.

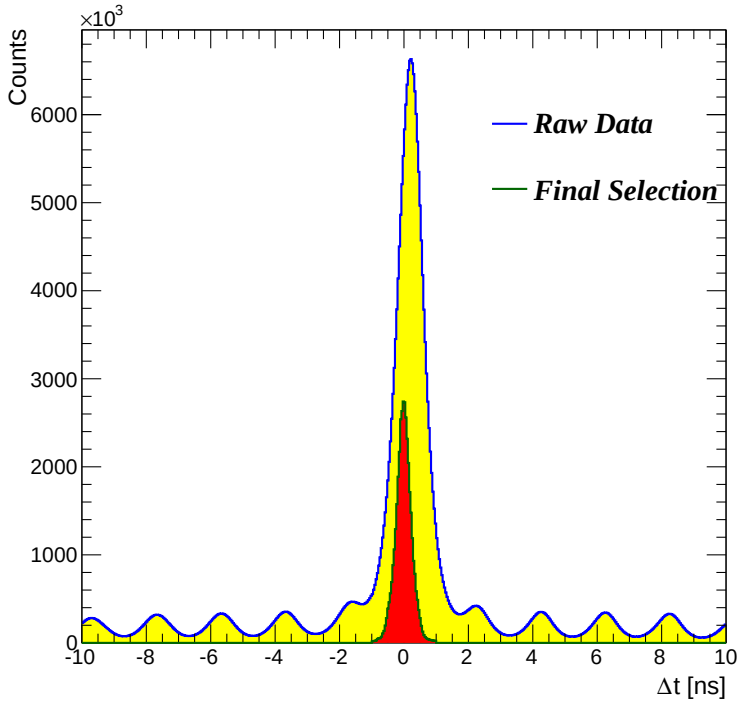

Figure 3.1: Coincidence time selection, where the chosen photons are inside $\Delta t = \pm 1$ ns cut shown as the red central peak.

3.3 Particle Identification

To illustrate the different types of particles that were present in the final state a β versus momentum distribution is shown in Fig. 3.4. To separate the particles of interest, the next step in the analysis was to calculate the difference between the measured speed and the calculated speed of each particle

$$\Delta\beta_m = \beta_{meas} - \beta_{calc} = \beta_{meas} - \frac{p}{\sqrt{p^2 + m^2c^2}}, \tag{3.2}$$

where p is the particle's momentum and m is the nominal mass of the particle. Using this $\Delta\beta$ difference and the charge of the track, the particles selected were only those found within the 3σ cut range as follows: protons if $-0.029 < \Delta\beta_p < +0.032$, positive pions if $-0.036 < \Delta\beta_{\pi^+} < +0.038$ and negative pions if $-0.029 < \Delta\beta_{\pi^-} < +0.033$ as shown in Figs. 3.5, 3.6, and 3.7.

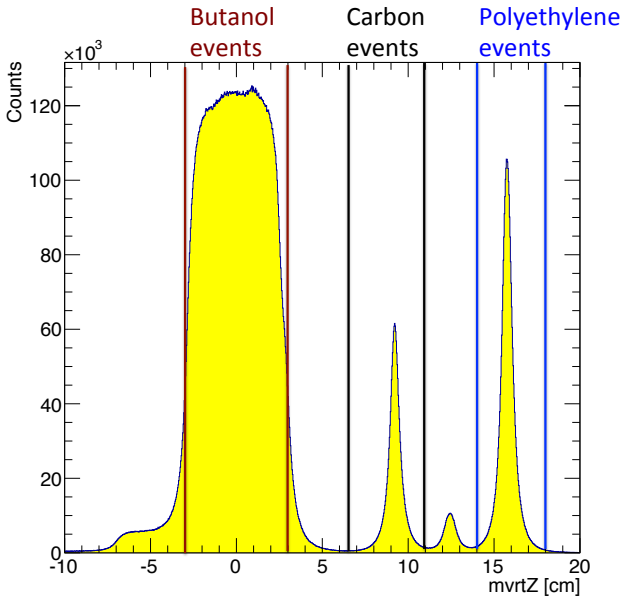

Figure 3.2: Event Z-vertex distribution for g9b circularly polarized photon data showing the cuts applied for the butanol, carbon and polyethylene targets.

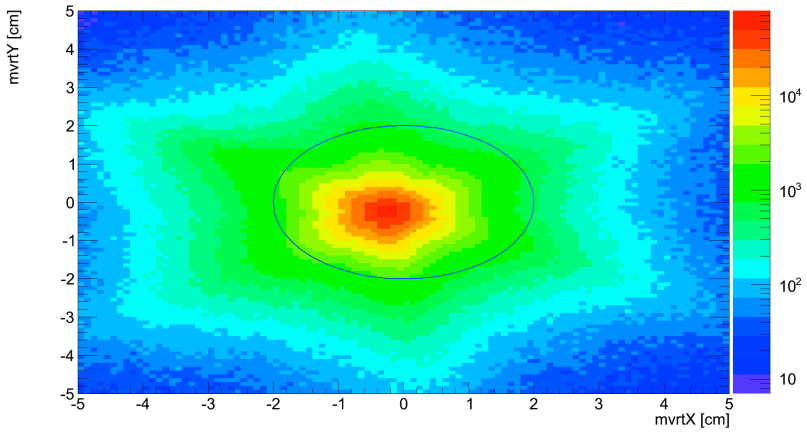

Figure 3.3: The X and Y vertex cut includes the events 2 cm away from the center of CLAS $(X, Y, Z) = (0, 0, 0)$ and only these selected events were further used in the analysis.

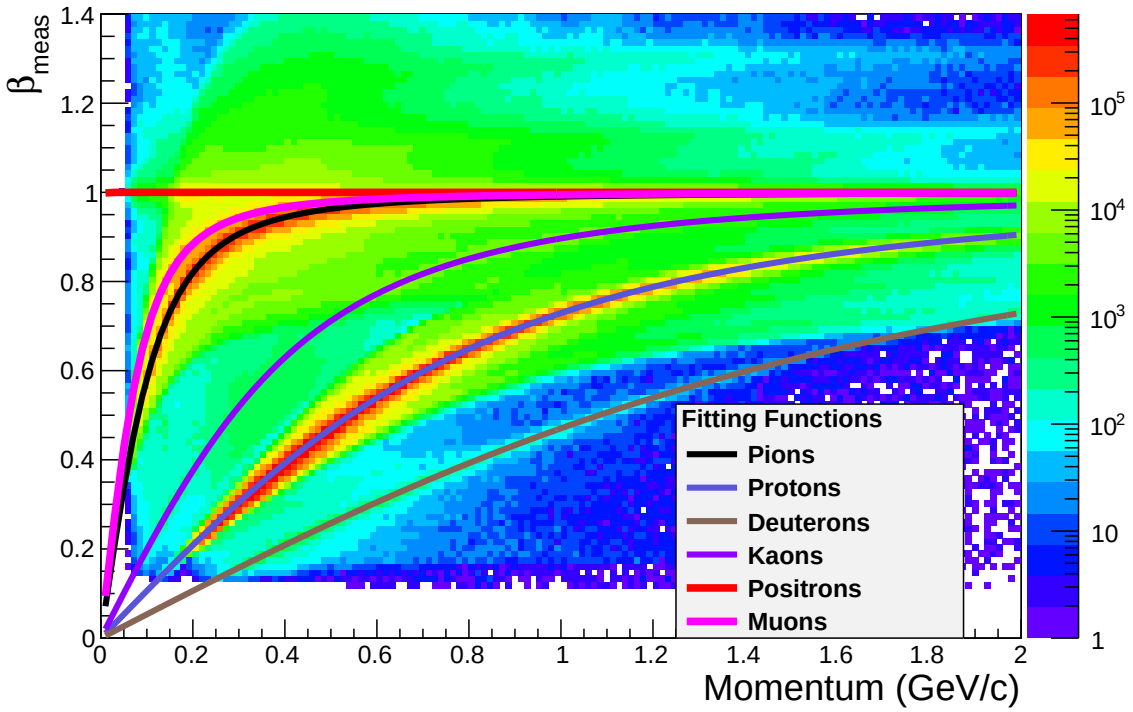

Figure 3.4: Beta versus momentum distribution, where different particles are present: deuterons (light brown curve), protons (blue curve), kaons (violet curve), pions (black curve), muons (magenta curve), and positrons (red curve passing through $\beta_{meas} = 1$).

3.4 Energy Loss Correction For Charged Particles In CLAS

When the proton, π^+, and π^- passed through the target, scintillator material, or even air they lost part of their energy due to ionization and excitation processes and thus one should account for this energy loss. So in order to correct for the energy loss which occurred in the CLAS detector, a software package [39] was used and corrections were applied to correct for the energy lost when the charged particles passed through the target cell wall, between the event vertex and the target wall, through the start counter, through the air of drift chambers and the scattering chamber and through structural components found in their path. Figures 3.8 and 3.9 show the comparison of the missing masses squared of the proton and pions before and after the energy

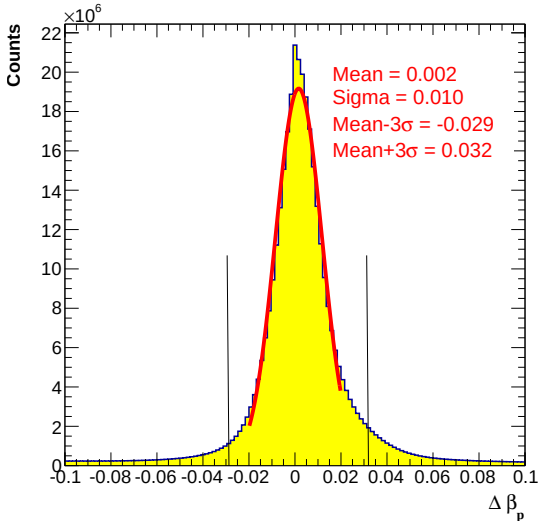

Figure 3.5: $\Delta\beta_p$ distribution showing proton-selection cut.

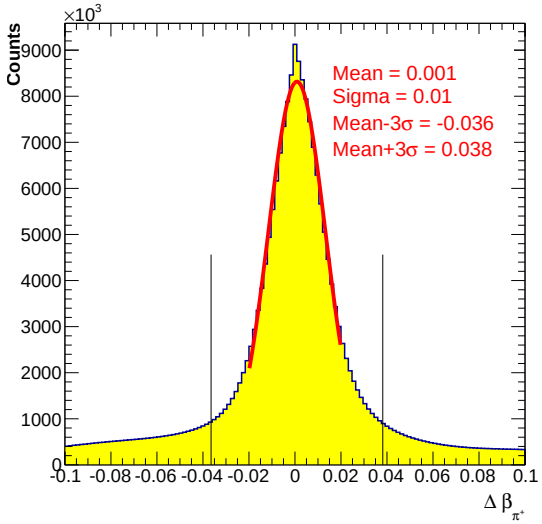

Figure 3.6: $\Delta\beta_{\pi^+}$ distribution showing positive pion-selection cut.

loss correction, and one can clearly see that the distributions were shifted towards the nominal mass squared of the particle and the peaks also got narrower as expected. These corrections return the real value of the momentum of the particles at the event vertex before losing any of its energy and they account for a couple of MeV.

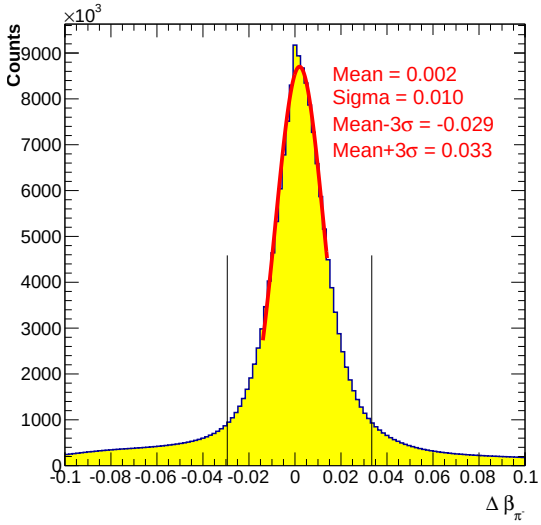

Figure 3.7: $\Delta\beta_{\pi^-}$ distribution showing negative pion-selection cut.

3.5 Momentum Correction

After the energy-loss corrections, also corrections were applied to the final-state particles' momenta. The need for correcting the momentum arises due to discrepancies between the actual magnetic field and the field map used to reconstruct the path of the particle and also due to drift chambers inefficiencies. Arizona State University group provided momentum corrections for the proton and positive pion. The method used the channels $\gamma p \to pX$ and $\gamma p \to \pi^+ X$ to correct the momentum of positive pion and protons and eliminate the azimuthal dependence of the missing-mass-squared distributions [40]. Florida State University (FSU) group obtained a set of correction parameters to fine-tune the momentum of the negative pion. These parameters were a function of momentum, polar angles and azimuthal angles. For comparison, Fig. 3.8 and Fig. 3.9 show the missing-mass-squared distribution for each final-state particle before any correction, after the energy loss correction was applied, after ASU momentum correction, and after FSU correction. The results of these corrections are the following: the mean value of the missing-mass-squared is closer to the nominal mass squared of the particle and the distributions get narrower after

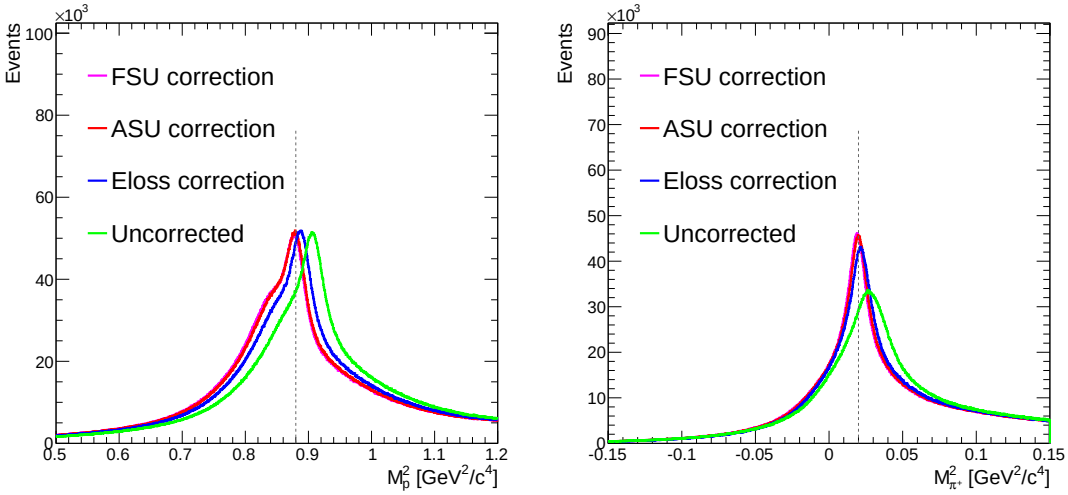

Figure 3.8: Missing-mass-squared distributions of the protons (left) and positive pions (right) before and after energy and momentum corrections.

applying the ASU corrections. This analysis used the ASU corrections for the proton and the positive pions but the FSU momentum correction for the negative pion was not applied because of the minimal effect it had on the missing-mass-squared distribution (Fig. 3.9).

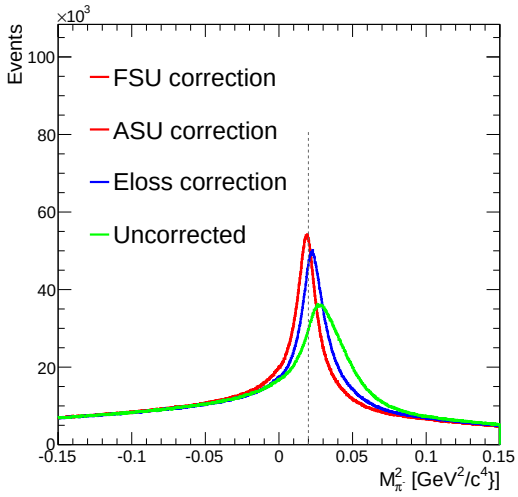

Figure 3.9: Missing-mass-squared distribution of the negative pions before and after energy and momentum corrections.

3.6 Tagger Sagging

A weaken support of some the E-counters caused a tagger sagging of the order of a few mm, that was discovered during prior experiments [41]. This tagger sagging resulted in measuring slightly different electron energies, but it was taken care of by the reconstruction code and no additional correction was needed afterwards.

3.7 Fiducial Cuts

No fiducial cuts were applied in this analysis.

3.8 TOF Study

A study was performed to evaluate the proton and pion time-of-flight-difference distributions $\Delta TOF = \frac{d_{SC}}{\beta_{calc}} - \frac{d_{SC}}{\beta_{meas}}$ for all sectors, paddles, and runs, where d_{SC} is the path length from the reaction vertex to the TOF paddle, β_{calc} and β_{meas} are β calculated, respectively measured for that given particle. For each pion and proton of a given run, ΔTOF was calculated and then collected in a distribution like the ones shown in Figs. 3.10 and 3.13. These distribution were fitted and the mean value was extracted and recorded for that particular run, sector and paddle and it is shown in Fig. 3.14 (showing an example of a good paddle) and Fig. 3.15 (showing an example of a problematic paddle). The average ΔTOF should normally be centered at zero as shown by Fig. 3.10 and 3.11, but looking at the Fig. 3.12 and 3.13 one could see that for certain paddles the average is not at zero, but rather is resembling a double Gaussian structure which hints at a hardware or calibration problem. In this case and other similar situations where the distributions are too broad and they are not normal distributions it is preferred to discard these paddles, and Table 3.1 lists the TOF paddles that were discarded in this analysis.

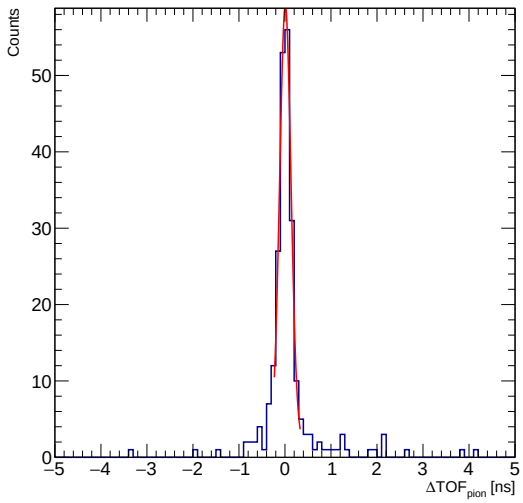

Figure 3.10: Average ΔTOF_{pion} distribution for run number 62381, sector 1 and TOF paddle number 1 peaks as expected at zero and the fitting works very well in providing the average TOF.

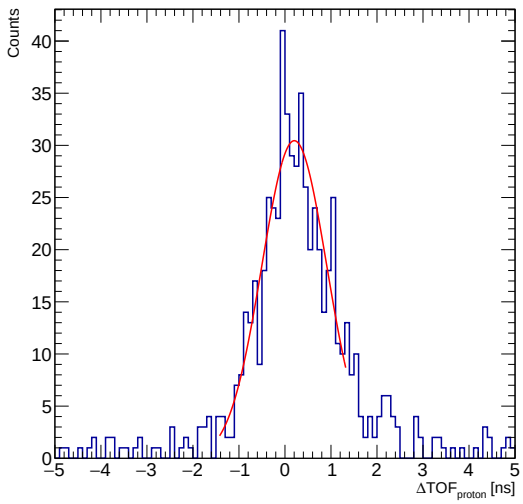

Figure 3.11: Average ΔTOF_{proton} distribution for run number 62562, sector 1 and TOF paddle number 33 where the fitting provides an average close to zero.

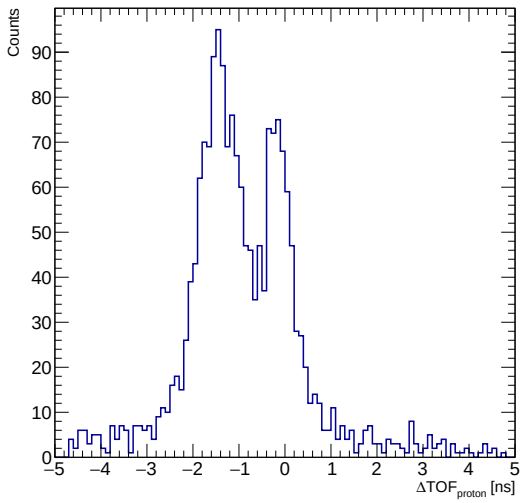

Figure 3.12: Average ΔTOF_{proton} distribution for run number 62638, sector 3 and paddle 26 showing a double peak structure and the fitting to extract the average TOF fails.

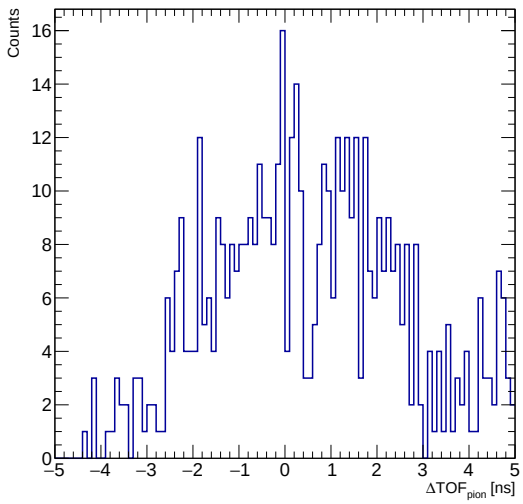

Figure 3.13: Average ΔTOF_{pion} distribution for run number 62562, sector 6 and paddle 33 showing a broad and asymmetric distribution.

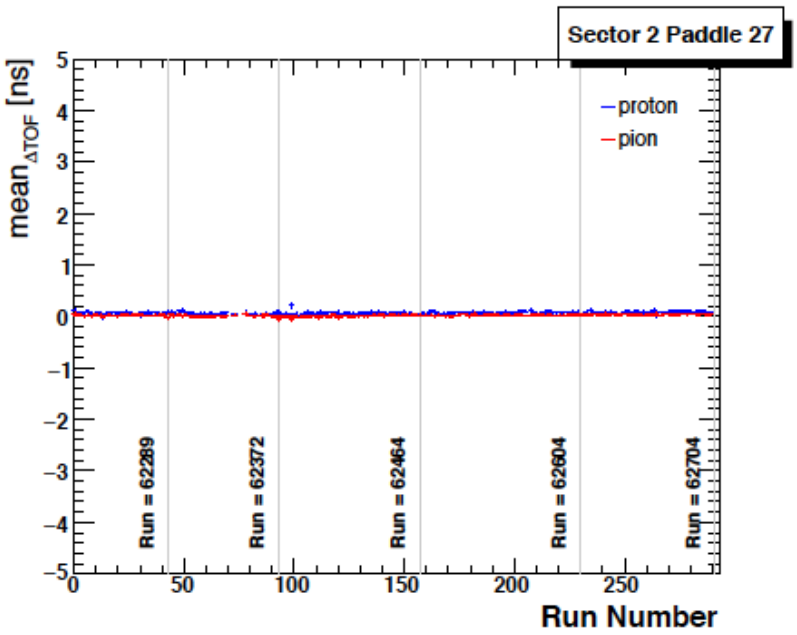

Figure 3.14: Average ΔTOF_{pion} and average ΔTOF_{proton} distribution versus run number for paddle 27 an sector 2 showing a mean ΔTOF value close to zero as expected and this is an example of a good TOF paddle.

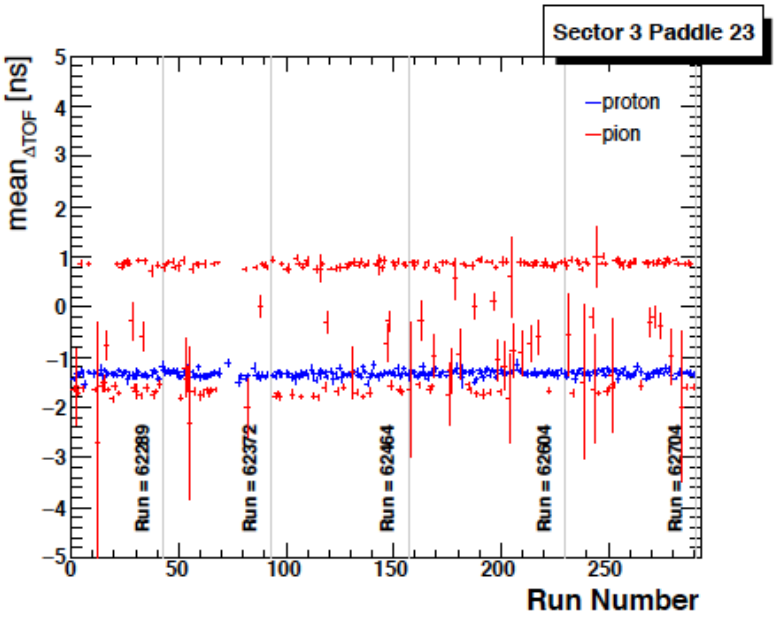

Figure 3.15: Average ΔTOF_{pion} and average ΔTOF_{proton} distribution versus run number for paddle 23 an sector 3, showing a mean ΔTOF value shifted from zero and indicating a problematic paddle that will be discarded from the analysis.

Table 3.1: Bad TOF paddles that were eliminated from this analysis.

Sector	TOF paddle
1	34, 44 ,52, 53, 54, 55, 56, 57
2	26, 44, 45, 49, 51, 53, 54, 55, 56, 57
3	23, 26, 50, 51, 52, 53, 54, 55, 56, 57
4	44, 48, 49, 53, 54, 55, 56, 57
5	22, 23, 27, 40, 50, 51, 52, 53, 54, 55, 56, 57
6	14, 33, 49, 52, 53, 54, 55, 56, 57

3.9 Reaction Channel Selection And Missing Masses

The reaction-channel selection is taking place after photon selection, particle identification, energy loss and momentum corrections were applied. Once the particles of interest have been identified the next step is to select the reaction channel, knowing that in the final state there should be one proton, one positive pion, and one negative pion. The CLAS spectrometer detects sometimes all 3 particles of interest and sometimes only two of them and the third must be reconstructed, which leads to 4 different cases or 4 topologies as they were called:

- topology 1: $\vec{\gamma}\vec{p} \rightarrow p\pi^+\pi^-(X)$, where $X = 0$ and no particle is missing
- topology 2: $\vec{\gamma}\vec{p} \rightarrow \pi^+\pi^-(X)$, $X = p$ because p is missing
- topology 3: $\vec{\gamma}\vec{p} \rightarrow p\pi^-(X)$, $X = \pi^+$ because π^+ is missing
- topology 4: $\vec{\gamma}\vec{p} \rightarrow p\pi^+(X)$, $X = \pi^-$ because π^- is missing

As seen above, for topology 1 all three particles were detected and for the other topologies only two out of three particles were detected. Figures 3.16 and 3.17 show the reconstructed missing-mass-squared distributions for the various topologies for the entire data set. The blue distributions are from butanol-target events and include free-proton and bound-nucleon background events. The red distributions are scaled distributions of carbon-target events and show how the background is distributed. The differences are shown in green and give the distribution of the free-proton events peaking at the expected mass-squares. In topology 2 the shape of the bound-nucleon background is similar to the signal shape in the missing-mass-squared distribution and limited statistics in the background-subtraction procedure (see the following Chapter) made it difficult to separate signal from background. Topology 2 was not further used in this analysis.

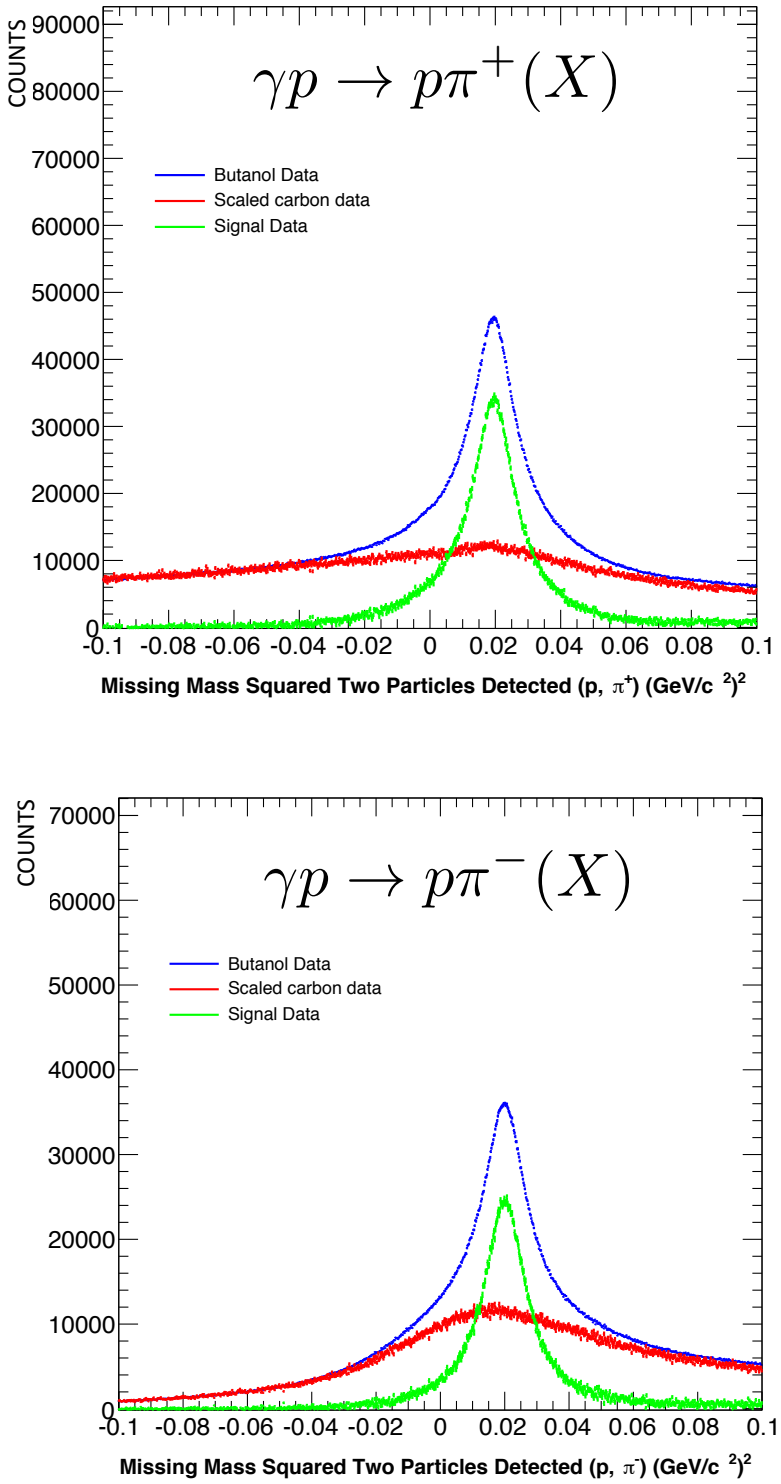

Figure 3.16: Missing-mass-squared for π^- missing topology (top) and π^+ missing (bottom), where the blue curve represents the butanol events, which are free and bound nucleon events, the red curve represents the scaled carbon events, consisting of bound nucleon events and the green curve represents the difference between the butanol and carbon distribution.

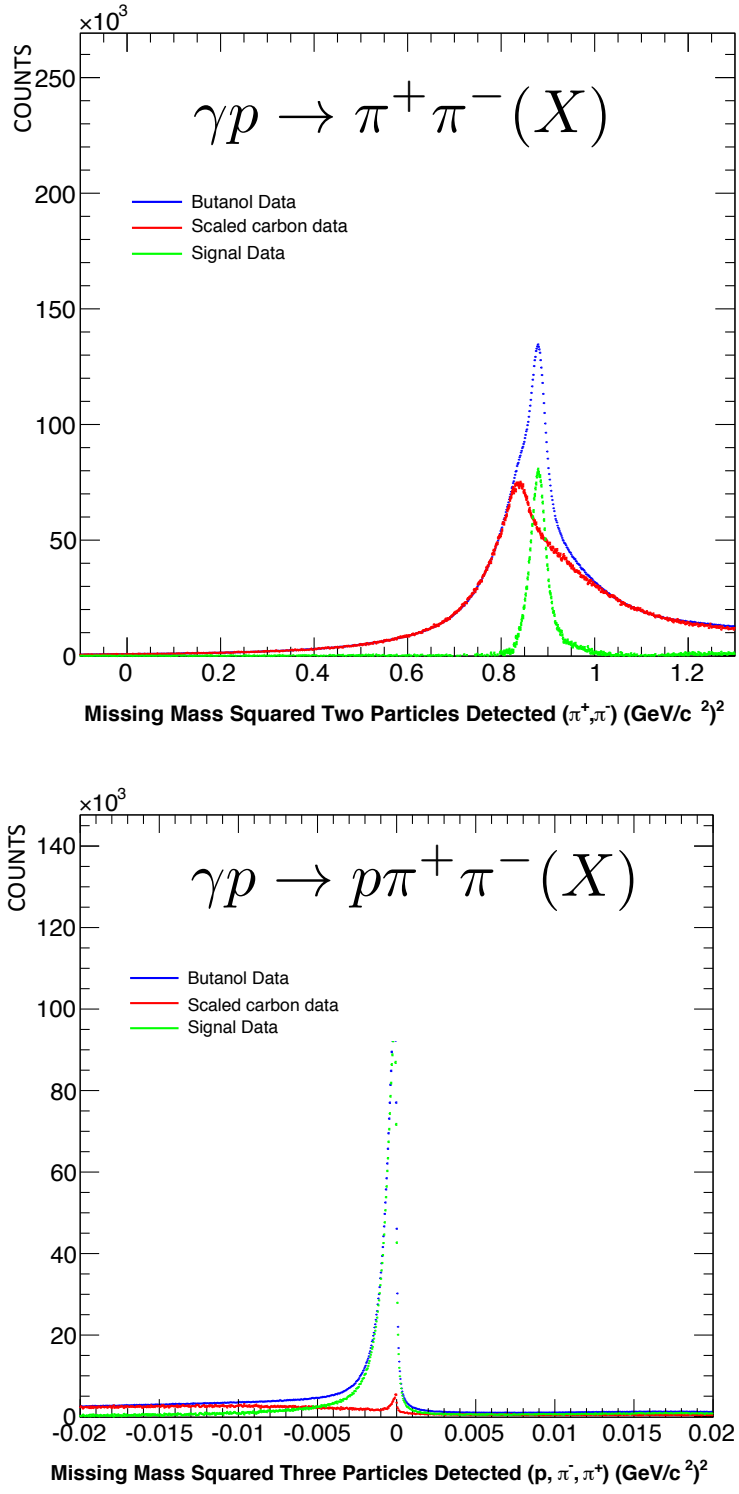

Figure 3.17: Missing-mass-squared distribution for missing proton topology (top) and missing zero topology (bottom), where the blue curve represents the butanol events, which are free and bound nucleon events, the red curve represents the scaled carbon events, consisting of bound nucleon events and the green curve represents the difference between the butanol and carbon distribution.

Chapter 4

Signal Background Separation

4.1 Signal Background Separation Methods

The butanol target ($C_4H_{10}O$) is made up of 10 free protons and 64 bound nucleons and due of its composition it will generate free nucleon events and bound nucleon events. But only the free protons can be polarized, while the rest of the butanol nucleons (protons and neutrons) are unpolarized.

The events of interest for this analysis are the signal events or the polarized free protons events coming from the butanol target. The butanol target, however, was also source of bound-nucleon background events. This chapter discusses two methods that could be used to distinguish between the signal and background events, but only the latter method will be further chosen in this analysis, due to its advantages soon to be discussed.

Background subtraction - Integrated method

The first alternative that could be used for distinguishing the signal events from the background events is called the **integrated method** and involves the calculation of a dilution factor d for each kinematic bin as:

$$d = \frac{\text{free proton events}}{\text{butanol events}} = \frac{\text{butanol events} - \text{scaled carbon events}}{\text{butanol events}} \tag{4.1}$$

where d represents the ratio between the number of free-protons events and the total number of events from the butanol target, which sums up the free and the bound nucleon contributions. To get the dilution factor, the carbon-target data were used

to measure the bound-nucleon background from the butanol target. The premise was that the missing-mass-squared distributions from ^{12}C and ^{16}O nuclei are similar. Since the carbon target had a much smaller size, the statistics of the carbon target was about 1/10 of the butanol statistics and thus the carbon data needed to be scaled in order to determine the dilution factor. The method employed in determining the scale factor [42] was a method accepted and widely used by the members of the FROST experiment in different analyses. It consisted from choosing a region R (Fig. 4.1) outside the signal region of butanol missing-mass-squared distribution and the total number of butanol events contained in that region was divided by the total number of carbon events corresponding to the same region R, the result being the scale factor for that kinematic bin. By subtracting from the butanol distribution the scaled carbon distribution one gets the signal events' distribution as illustrated in Fig 4.1. Once the

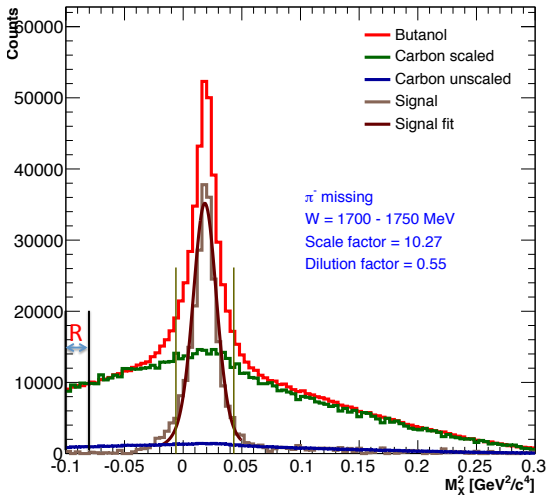

Figure 4.1: Mass squared for missing π^- topology showing the unscaled carbon (blue curve), scaled carbon (green curve), signal (brown curve), butanol (red curve) distributions, and the signal fit function (darker brown curve), where R is the region ranging from the missing-mass-squared of -0.1 to -0.08 GeV$^2/c^4$.

signal events were extracted, the dilution factor d was calculated for the 3σ region around the peak of the signal distribution. When calculating the naive dilution factor one gets $d = 10/74 = 0.135$, but in reality the dilution factors depend on the missing

mass distributions and on the selections applied to the distributions (e.g. kinematic cuts) which could diminish the background contribution and could increase the value of the dilution factor as shown in Fig. 4.1. In this analysis, the weighted average of the dilution factors for all topologies integrated over all kinematic variables is equal to 0.53, which means that 53% of the selected butanol events were free protons events and the rest constituted bound-nucleons events.

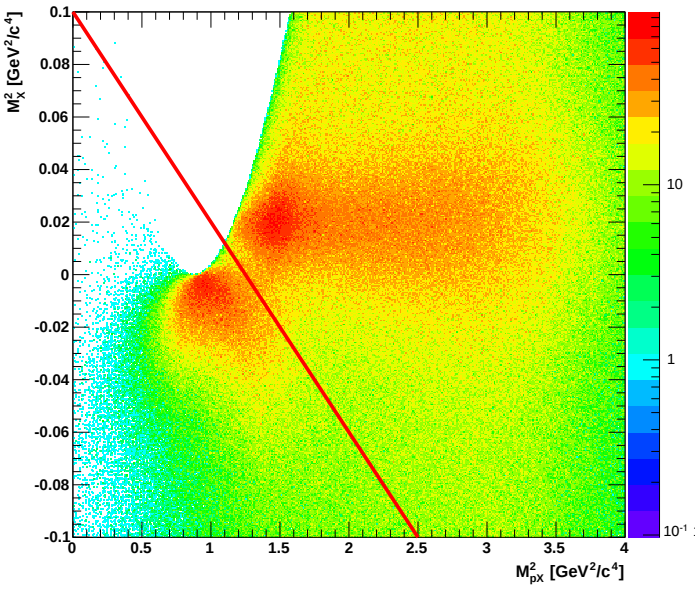

Figure 4.2: Missing-mass-squared distribution versus the invariant-mass-squared of pX for missing π^+ topology, showing the neutron events coming from $\gamma n \to p\pi^-(X = 0)$ (lower left peak) and positive pion events coming from $\gamma p \to p\pi^-(X = \pi^+)$ (upper right peak). The red diagonal line indicates the cut applied in order to eliminate from the analysis the neutron events on the left side of the diagonal red line.

For the missing-positive-pion topology, the missing-mass-squared distribution is double peaked (Fig. 4.3) due to background-neutron events coming from $\gamma n \to p\pi^-(X = 0)$ that needs to be separated from the positive proton events coming from $\gamma p \to p\pi^-(X = \pi^+)$ through a cut shown in Fig. 4.2. After applying the cut the resulting missing-mass-squared of π^+ (yellow filled distribution in Fig. 4.3) was used

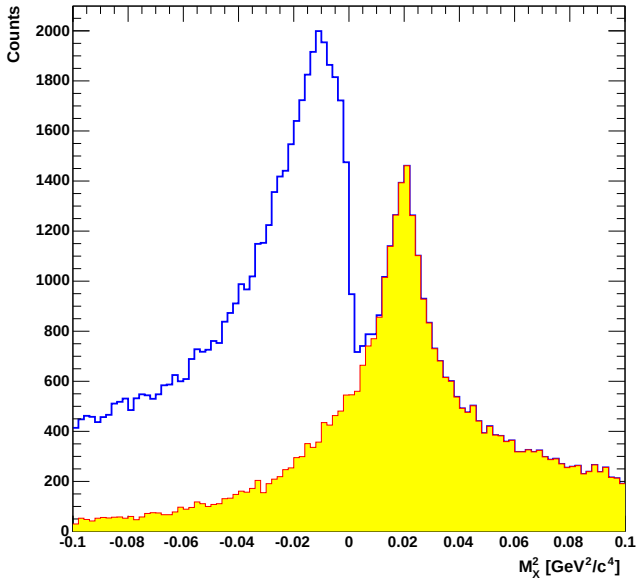

Figure 4.3: Missing-mass-squared for missing-positive-pion topology before (blue curve) and after the cut of neutron events (yellow filled distribution) for run number 62207.

further in the analysis.

Background subtraction - Probabilistic weighting method using butanol and carbon data fitting

The method of choice used in order to distinguish between the signal events and the background events was the **probabilistic weighting method**. The main idea of this method is to determine the probability for a given event ϵ_i to be a signal event Q_i or a background event $1 - Q_i$. The first step consists of pre-binning data in center of mass energy bins of 50 MeV wide. Next, a distance measure was defined and this indicated how close two events were in the kinematic space defined by the following variables $\cos\theta^*$, $\cos\theta_{CM}$, ϕ^*, $m_{p\pi^+}$, $m^2_{\pi^+\pi^-}$ (variables defined in Section 6.1). This distance measure between an event ϵ_a and any other random event ϵ_b from the that

Table 4.1: Distance scales for nearest-neighbor determination.

Kinematic variable	Δ_i
$\cos\theta^*$	2
$\cos\theta_{CM}$	2
ϕ^*	2π
$m_{p\pi^+}$	m_p
$m^2_{\pi^+\pi^-}$	$m_{\pi^+}\cdot m_{\pi^+}$

particular W bin is expressed as

$$D_{\epsilon_a,\epsilon_b} = \sum_{i=1}^{5} \left(\frac{\Gamma_i^{\epsilon_a} - \Gamma_i^{\epsilon_b}}{\Delta_i} \right)^2, \tag{4.2}$$

where $\Gamma_i = \cos\theta^*$, $\cos\theta_{CM}$, ϕ^*, $m_{p\pi^+}$, $m^2_{\pi^+\pi^-}$ and Δ_i is distance scale. Table 4.1 shows the distance scales for each kinematic parameter.

For each event a (called ***seed event***), the 5000 kinematically nearest neighbors were found and these neighbors could have been butanol and respectively carbon events as shown in Figs. 4.4, 4.5, and 4.6. The best choice for the number of nearest neighbors was found to be 5000 due to the low statistics of carbon, after a study has shown that distributions counting less than 5000 nearest neighbors could not be used by this method and the reason will be explained shortly. The probabilistic weighting method relied on a fitting routine, which included a Gauss function for the signal plus a scaled cubic spline function for the background. A cubic spline $S_3(x)$ through 3 nodes of coordinates (x_1, y_1), (x_2, y_2) and (x_3, y_3) is a set of two cubic polynomial $S_{i=1,2}(x) = y_i + b_i(x - x_i) + c_i(x - x_i)^2 + d_i(x - x_i)^3$, which has the following properties: $S_i(x_i) = y_i$, $S_i(x_{i+1}) = y_{i+1}$, $S'_{i-1}(x_i) = S'_i(x_i)$, $S''_{i-1}(x_i) = S''_i(x_i)$.

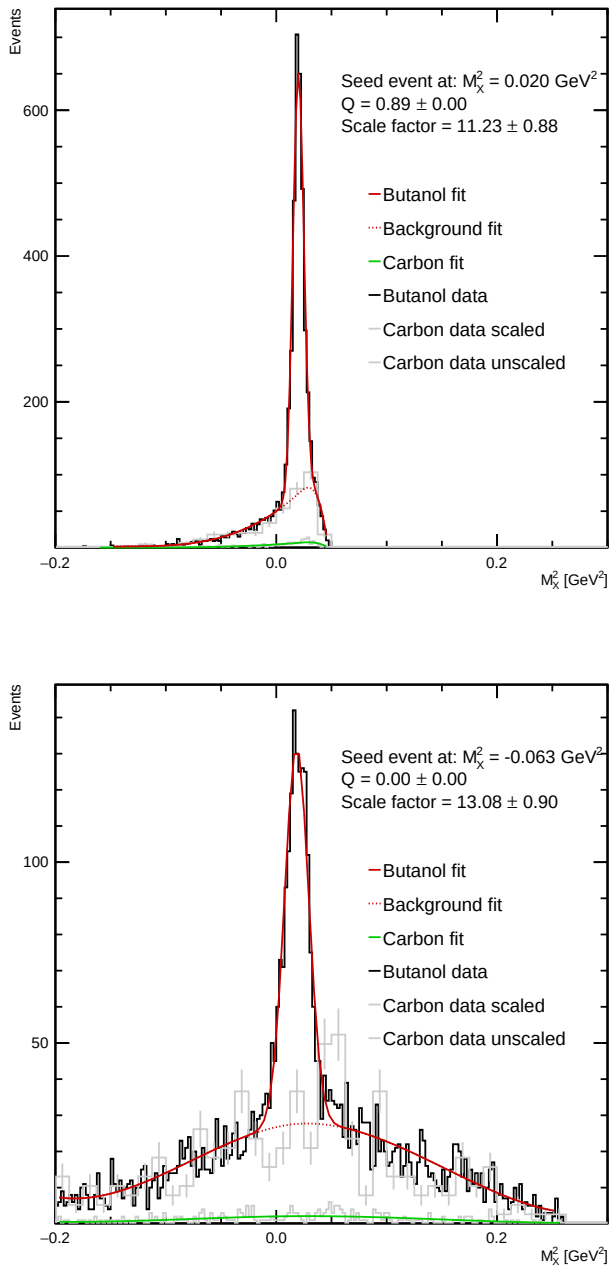

Figure 4.4: 5000 nearest neighbors distributions for missing π^- topology at $W = 1450 - 1500$ MeV (top), respectively at $W = 1950 - 2000$ MeV (bottom).

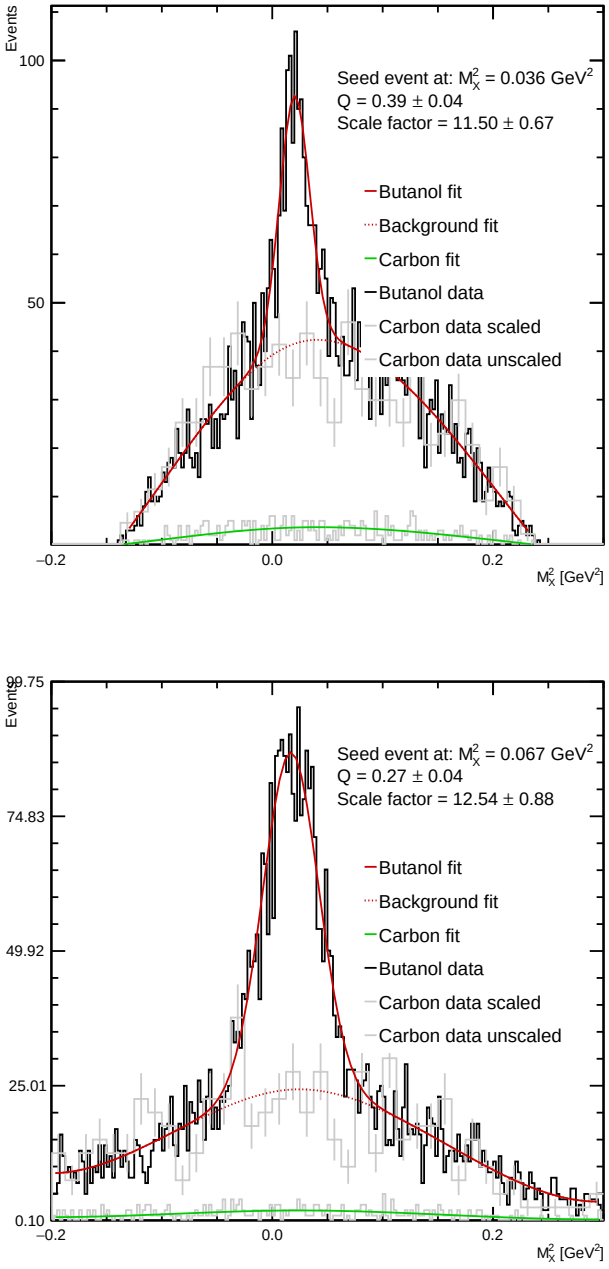

Figure 4.5: 5000 nearest neighbors distributions for missing π^+ topology at $W = 1950 - 2000$ MeV (top), respectively at $W = 2450 - 2500$ MeV (bottom).

The fit functions were

$$G(x) = p_2 e^{-\frac{(x-p_0)^2}{2p_1^2}}, \tag{4.3}$$

$$S_3(x) = f(x, p_3, p_4, p_5, p_6, p_7, p_8, p_9, p_{10}), \tag{4.4}$$

$$B(x) = V(x) + p_{11} S_3(x), \tag{4.5}$$

where p_0 is the Gaussian mean, p_1 the Gaussian sigma, p_2 the Gaussian height and the parameters p_3, p_4, p_5 represent the M_X^2 values corresponding to the positions of the three nodes of the spline function, while the parameters p_6, p_7, p_8, which are free parameters and correspond to the three nodes of $S_3(x)$. p_9 and p_{10} are the begin- and end-point derivatives of the spline function and p_{11} is the scale factor used for the background scaling. A simultaneous fit was performed where the carbon data was fitted with a cubic spline $S_3(x)$ and the butanol data was fitted with the function $B(x)$ and then using the maximum likelihood method (Eq. (4.6)) the fit parameters were extracted in order to calculate the probability for a particular butanol event to be a signal or background event. The fitting routine was implemented via RooFit package of ROOT program developed by CERN. In the fit

$$\chi^2 = 2\Big[\sum_i [B_i(x) - N_i^B \cdot \log B_i(x)] + \sum_j [S_3^j(x) - N_j^C \cdot \log S_3^j(x)]\Big] \tag{4.6}$$

was minimized. Here, the first summation was performed over the number of missing-mass-squared butanol bins, N_B^i representing the butanol entries per bin. The second summation was done over the number of bins of the carbon missing-mass-squared distribution, where N_C^j represents the carbon entries per bin. The carbon events were used by this method in order to help fitting the butanol background, and its importance was proved to be crucial in cases where the butanol distributions lacked the tails. Thus without the use of carbon data, the probabilistic weighting method will not work well in many cases where the tails of the missing-mass-squared distribution are non-existent and where the carbon offers a good hint for how the background

looks like, as shown in Fig. 4.7, and these cases dominate the whole lower energy range as discussed later.

For zero missing topology, where all particles were detected, the nearest neighbors distribution (Fig. 4.6) has a signal peak which is asymmetric and can not be described by a Gaussian function. So in this case the background alone was fitted and then the Q-value was determined by reading the counts of the butanol distribution and evaluating the background function at the position of the seed event.

The main advantage of the probabilistic weighing method is that each event from

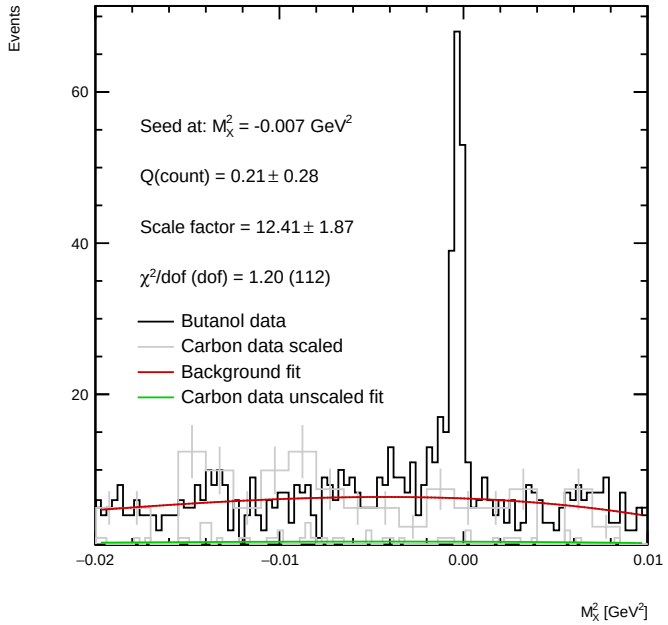

Figure 4.6: 5000 nearest neighbors distribution for missing zero topology for $W = 1950 - 2000$ MeV showing the background fit (red) which was used to determine the Q-value.

the dataset has an associated Q-value and this speeds up a lot the extraction of the asymmetries since the analysis does not have to be repeated each time to determine the dilution factors for the kinematic bin of choice.

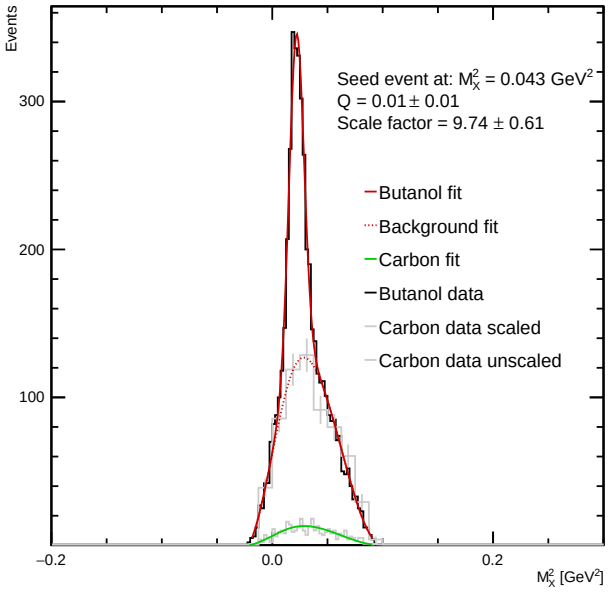

Figure 4.7: 5000 kinematically closest neighbors for the missing π^+ topology for $W = 1450 - 1500$ MeV.

4.2 Signal Background Separation Quality Checks

Looking at Fig. 4.8, which represents the χ^2-distribution one could see that the fitting procedure gives χ^2 values that are distributed mostly around 1, indicating that the fitting worked well. Another check was to look at the missing-mass-squared distributions for the butanol, carbon, and signal data given by the Q-value method versus the carbon and signal distributions given by the integrated method and compare the dilution factors for the 3σ range around the signal peak distribution. One could see a good agreement between these two different background subtraction methods for different energy ranges and topologies, as shown by Fig. 4.9 and Fig. 4.10.

Another check performed was to look at the average scale factor per missing-mass-squared and Fig. 4.11 shows that the average scale factor stays constant for a given W bin. Also the average χ^2 versus missing-mass-squared was verified and Fig. 4.12 shows that it stays close to 1 as expected.

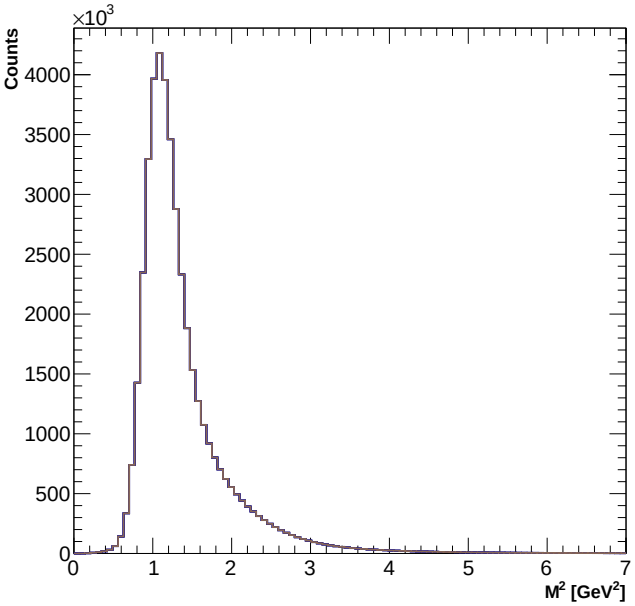

Figure 4.8: The χ^2-distribution resulted from Q-value determination method.

4.3 Normalization

As mentioned before, the g9b circularly polarized data set is organized in five run groups and the target polarization alternates from positive orientation to negative from run group to run group, starting with run group one which is positively polarized, having three run groups positively polarized (run groups 1, 3 and 5) and two run groups negatively polarized (run groups 2 and 4). Since the number of photons for the positive target polarization data set is different than the photon number for negative target polarization data set, different run groups contain different number of events and so a normalization factor is required. The preferred normalization factor is the initial number of photons also called photon flux, which is not available for g9b data. So in this case, the normalization factor was the total number of the carbon target events (Table 4.2) recorded for each run group, this number being proportional to the number of incident photons.

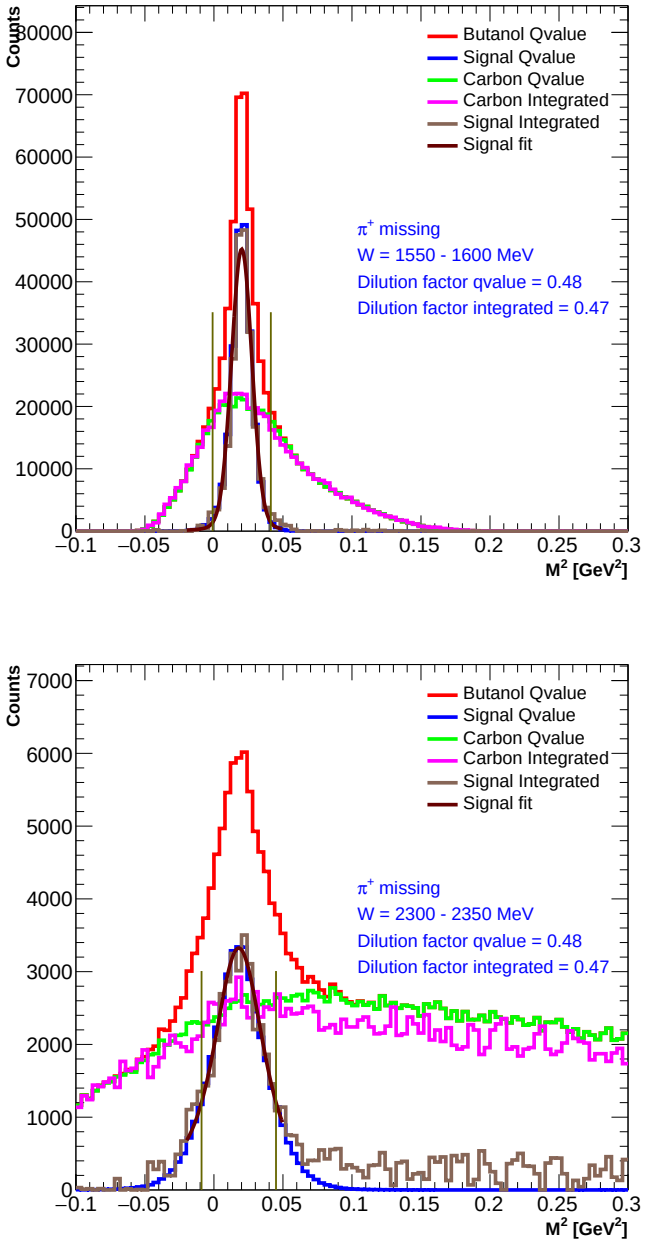

Figure 4.9: Missing-mass-squared distributions for butanol, signal, and background data for $W = 1550 - 1600$ MeV (top) and $W = 2300 - 2350$ MeV (bottom) for π^+ missing topology obtained using the Q-value method and the integrated method. It shows the dilution-factor comparison between the two methods for background subtraction.

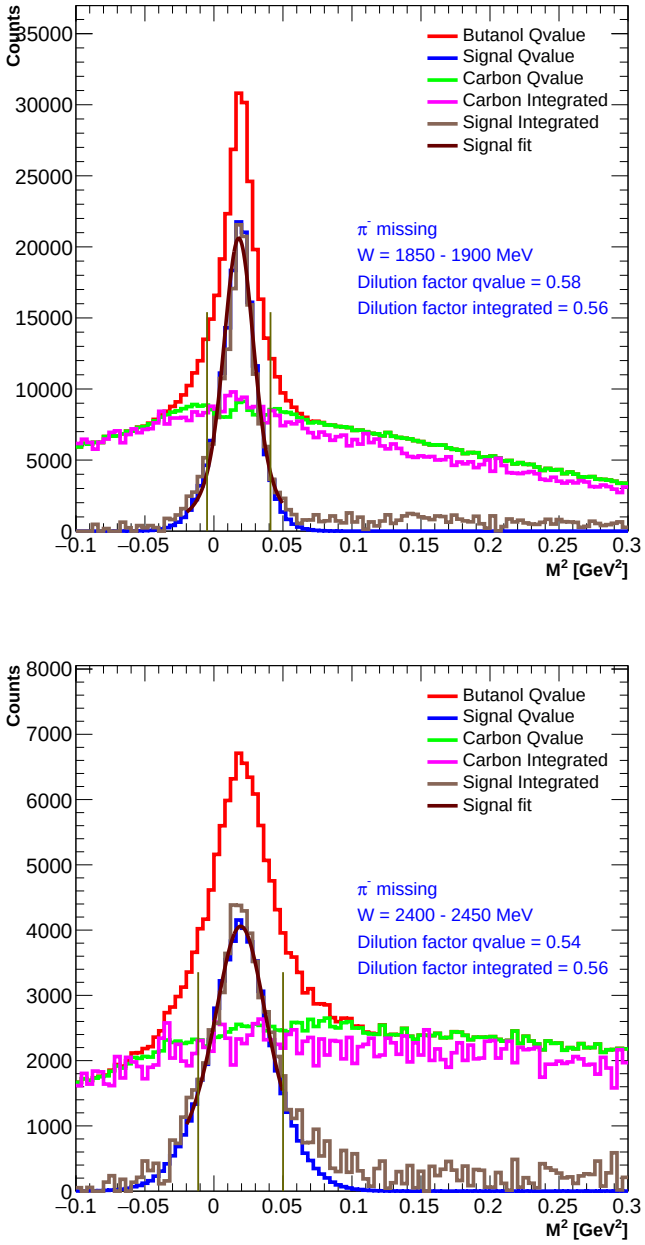

Figure 4.10: Missing-mass-squared distributions for butanol, signal, and background data for $W = 1850 - 1900$ MeV (top) and $W = 2400 - 2450$ MeV (bottom) for π^- missing topology obtained using the Q-value method and the integrated method. It shows the dilution-factor comparison between the two methods for background subtraction.

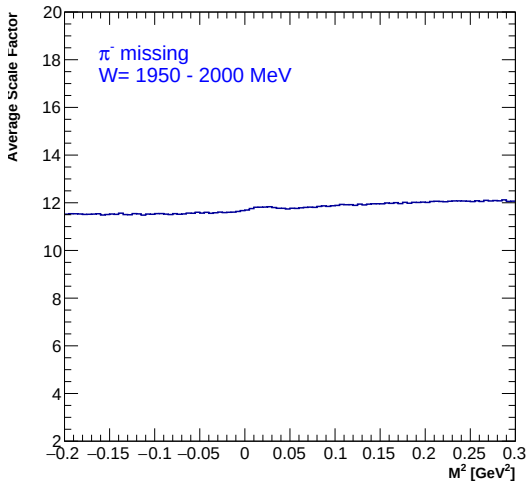

Figure 4.11: Average scale factor versus missing-mass-squared distribution for $W = 1950 - 2000$ MeV for missing π^- topology.

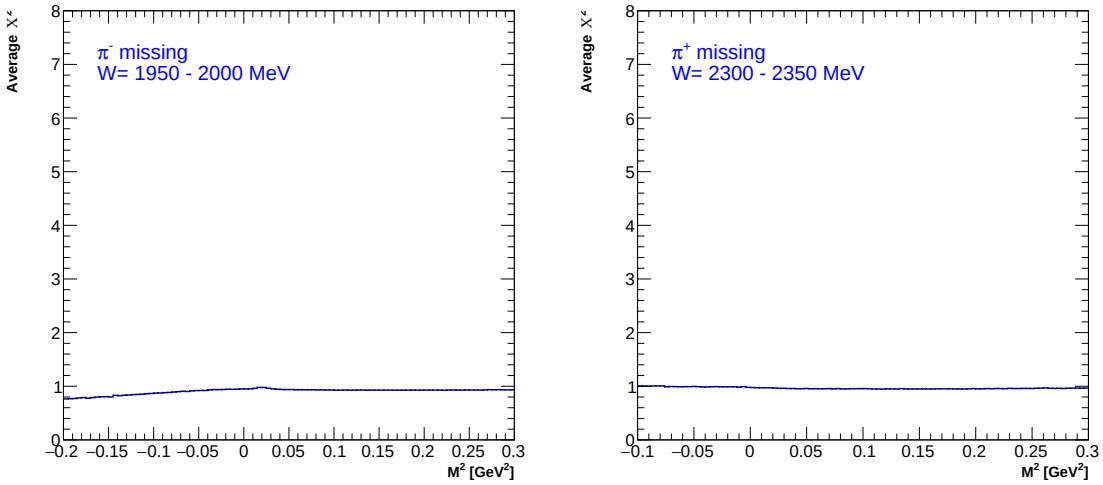

Figure 4.12: Average χ^2 per degree of freedom versus missing-mass-squared distribution for $W = 1950 - 2000$ MeV for missing π^- topology (left) and for $W = 2300 - 2350$ MeV for missing π^+ topology (right).

4.4 Simplified Expressions Of The Observables

Assuming the background to be unpolarized, the polarized cross-section for the kinematic bin τ is:

Table 4.2: Carbon-target yields.

Run group	Target polarization	Runs	Events
1	+	$62207 - 62289$	304606
2	−	$62298 - 62372$	388641
3	+	$62374 - 62464$	403271
4	−	$62504 - 62604$	645623
5	+	$62609 - 62704$	480411

$$\begin{aligned}\sigma = \sigma_{B0}(\tau) + \sigma_{S0}(\tau)[(1 + \bar{\Lambda}P_x(\tau)\cos\alpha + \bar{\Lambda}P_y(\tau)\cos\alpha) + \\ \bar{\delta}_{\odot}[I^{\odot}(\tau) + \bar{\Lambda}P_x^{\odot}(\tau)\cos\alpha + \bar{\Lambda}P_y^{\odot}(\tau)\cos\alpha]]\end{aligned} \tag{4.7}$$

where σ_{S0} represents the unpolarized signal cross-section and σ_{B0} represents the unpolarized background cross-section and the other variables were previously defined in Section 1.4. The relationship between the Q-value and the polarized, respectively unpolarized cross-section is:

$$Q(\tau) = \frac{\sigma_{S0}(\tau)}{\sigma_{S0}(\tau) + \sigma_{B0}(\tau)} \tag{4.8}$$

The moments method [43] allows the determination of an undiluted polarization observable (in this simplified example P_x), by using the ratio:

$$\frac{Y_{\cos\alpha}}{Y_{Q\cos^2\alpha}} = \frac{\int_\tau(\sigma_{S0}(\tau) + \sigma_{B0}(\tau))Q(\tau)P_x(\tau)d\tau}{\int_\tau(\sigma_{S0}(\tau) + \sigma_{B0}(\tau))Q(\tau)d\tau} = \frac{\int_\tau \sigma_{S0}P_x(\tau)d\tau}{\int_\tau \sigma_{S0}(\tau)d\tau} \approx \frac{1}{\bar{\Lambda}}\frac{\sum_i \cos\alpha_i}{\sum_i Q_i\cos^2\alpha_i} = \bar{P}_x \tag{4.9}$$

where the summation runs over the event index i. Similarly, one could obtain the simplified expressions for the all the other polarization observables as[1]

[1]The simplified estimator for the observable $\bar{I}^{\odot}$ is $\frac{\sum_i H_i}{\delta_{\odot}\sum_i Q_i}$ if the background is unpolarized; this is not the case in the present data.

$$\bar{P}_x = \frac{1}{\bar{\Lambda}} \frac{\sum_i \cos\alpha_i}{\sum_i Q_i \cos^2\alpha_i}, \tag{4.10}$$

$$\bar{P}_y = \frac{1}{\bar{\Lambda}} \frac{\sum_i \sin\alpha_i}{\sum_i Q_i \sin^2\alpha_i}, \tag{4.11}$$

$$\bar{P}_x^{\odot} = \frac{1}{\bar{\Lambda}} \frac{1}{\bar{\delta}_{\odot}} \frac{\sum_i H_i \cos\alpha_i}{\sum_i Q_i \cos^2\alpha_i}, \tag{4.12}$$

$$\bar{P}_y^{\odot} = \frac{1}{\bar{\Lambda}} \frac{1}{\bar{\delta}_{\odot}} \frac{\sum_i H_i \sin\alpha_i}{\sum_i Q_i \sin^2\alpha_i}. \tag{4.13}$$

The photon-beam helicity H_i enters the estimate of the helicity-dependent observables. Due to the high correlation between any two σ_{Q_i} and σ_{Q_j} from the data set, caused by the nearest neighbors technique used in determining the Q-values, the analytical error propagation is not feasible to implement since the data set contains tens of millions of events, and computationally speaking would require a huge amount of time and CPU power.

4.5 Bootstrapping With Sample Replacement

The method used in this analysis in order to estimate the observables' statistical uncertainties was the **bootstrap method with sample replacement** [44]. The bootstrapping algorithm with replacement consists of drawing from the original data set many data samples with some events being repeated and other events being skipped for a given sample. The number of drawn samples chosen for this analysis is equal to $N = 100$, and to produce these samples a random-number generator was used to select the events for each of the N samples. Each generated sample must contain the same number of events as the original data set and as an example one could have one sample containing the following event numbers: 0,1,1,2,4,5,6,6... and while other sample will contain the event numbers: 1,2,2,3,4,4,5,7,..., and so forth until N

bootstrap samples are obtained. Next, for each bootstrap sample the observables are extracted in the same way as when using the original data set and as a result N observables O_i are extracted for each angular bin. Then the average $\bar{O}$ for each angular bin was calculated and the corresponding variance for each bin:

$$\sigma^2_{O,\ bootstrap} = \frac{\sum_i^N (O_i - \bar{O})^2}{N-1} \tag{4.14}$$

where O_i is the observable extracted from the i^{th} bootstrap sample for that given bin and $\bar{O}$ represents the mean value of O_i for that particular angular bin after averaging over N bootstrap samples.

Chapter 5

Extraction of the observables

5.1 Moments' Method: The Extraction Of The Helicity-Independent Observables

The polarized cross section for the channel of this analysis is expressed as:

$$d\sigma = d\sigma_0\Big[1+\Lambda\cdot\cos\alpha\cdot P_x+\Lambda\cdot\sin\alpha\cdot P_y+\delta_\odot(I^\odot+\Lambda\cdot\cos\alpha\cdot P_x^\odot+\Lambda\cdot\sin\alpha\cdot P_y^\odot)\Big], \quad (5.1)$$

where σ_0 is the unpolarized cross section, α is the target polarization angle, Λ is the degree of the target polarization, $\delta_\odot$ the degree of the photon beam polarization and $I^\odot$, P_x, P_y, $P_x^\odot$, and $P_y^\odot$ are the observables to be extracted in this analysis. The observables arising due to the polarization of the recoil-proton are integrated out and do not appear in the polarized cross section, Eq. (5.1). The observables to be extracted in this analysis are only due to the polarization of the incident proton and to the polarization of the photon beam. The extraction of the polarization observables involves observed angular-dependent yields for 0° and 180° or (positive, negative) target polarization orientations and ±1 photon-helicity states. For a given kinematic bin defined by τ=(W, ϕ^*, θ_{CM}, θ^*, $m^2_{\pi^+\pi^-}$, $m_{p\pi^+}$) as shown in Section 6.1, the normalized yield can be written as

$$\begin{aligned} Y = \frac{1}{2\pi}\int\int_0^{2\pi} Y_0'(\tau)A(\tau,\alpha)(1+\Lambda P_x\cos\alpha+\Lambda P_y\sin\alpha+ \\ +\delta_\odot(I^\odot+\Lambda P_x^\odot\cos\alpha+\Lambda P_y^\odot\sin\alpha))d\alpha d\tau, \end{aligned} \quad (5.2)$$

where $Y_0'(\tau)$ is the unpolarized cross section for the kinematic bin τ. The acceptance $A(\tau,\alpha)$ for the two different target orientations is expressed through a Fourier series

as a function of the kinematic parameters of that bin, represented by τ, and as a function of the polarization angle α

$$A(\tau,\alpha) = \frac{a_0^0(\tau)}{2} + a_1^0(\tau)\cos\alpha + b_1^0(\tau)\sin\alpha + a_2^0(\tau)\cos 2\alpha + b_2^0(\tau)\sin 2\alpha, \quad (5.3)$$

$$A(\tau,\alpha+\pi) = \frac{a_0^{180}(\tau)}{2} - a_1^{180}(\tau)\cos\alpha - b_1^{180}(\tau)\sin\alpha + a_2^{180}(\tau)\cos 2\alpha + b_2^{180}(\tau)\sin 2\alpha, \quad (5.4)$$

where a^0, a_1^0, b_1^0, a_2^0 and b_2^0 are the Fourier coefficients corresponding to the positive target orientation and a^{180}, a_1^{180}, b_1^{180}, a_2^{180}, and b_2^{180} are the Fourier coefficients corresponding to the negative target orientation. Higher-order terms are possible but do not enter in the final result. For an ideal detector, the acceptance is constant over the run time, but for a detector in real life the acceptance could be changing over the run time. Since this analysis extracts polarization asymmetries, and it needs to account for any instrumental asymmetries. A study of the unpolarized target data (e.g. carbon and polyethylene targets) was done to verify whether the acceptance changed from run group to run group or not. The expectation is that since the carbon target was unpolarized, there should be no target-polarization asymmetries coming from the carbon data, and any yield asymmetry in this case should be instrumental. Since the observed yields are proportional to the Fourier coefficients times the unpolarized yield, one cannot determine the Fourier coefficients individually, but look at their ratios where the unpolarized yield cancels out. The carbon data for a high statistics bin ($W = 1550 - 1650$ MeV) shows that the Fourier coefficients ratios are non-zero and they vary from run group to run group (Fig. 5.1). Starting from the assumption that the acceptance for carbon and butanol data was predominantly the same, one could use these Fourier coefficients from carbon to correct the detector asymmetries that show up in butanol data.

To extract the helicity independent observables P_x and P_y, the moments corresponding to the two possible orientations of the target polarization $(0, 180)$ were calculated. The helicity-dependent part of the integral ($\bar{\delta}_\odot$ term) cancels out when

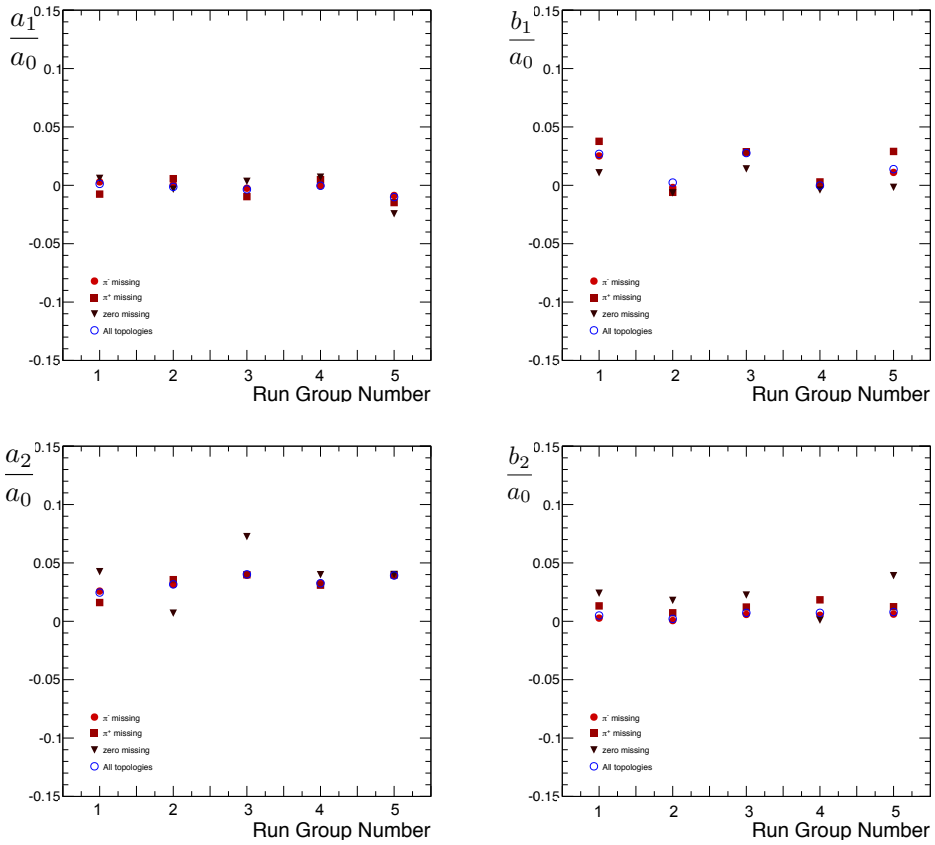

Figure 5.1: The Fourier coefficients ratios a_1/a_0, b_1/a_0, a_2/a_0, and b_2/a_0 for the five run groups as seen for the carbon data when $W = 1550 - 1650$ MeV. It can be seen that from run group to run group the coefficients a_1 and b_1 change for each topology.

summing over the helicity states $(+1, -1)$.

$$Y^0 = \iint_0^{2\pi} \frac{Y_0'}{\pi} A(\tau, \alpha)(1 + \Lambda^0 P_x \cos\alpha + \Lambda^0 P_y \sin\alpha) d\alpha d\tau \tag{5.5}$$

$$Y^{180} = \iint_0^{2\pi} \frac{Y_0'}{\pi} A(\tau, \alpha + \pi)(1 + \Lambda^{180} P_x \cos\alpha + \Lambda^{180} P_y \sin\alpha) d\alpha d\tau \tag{5.6}$$

$$Y^0_{\sin\alpha} = \iint_0^{2\pi} \frac{Y_0'}{\pi} A(\tau, \alpha) \sin\alpha(1 + \Lambda^0 P_x \cos\alpha + \Lambda^0 P_y \sin\alpha) d\alpha d\tau \tag{5.7}$$

$$Y^{180}_{\sin\alpha} = \iint_0^{2\pi} \frac{Y_0'}{\pi} A(\tau, \alpha + \pi) \sin\alpha(1 + \Lambda^{180} P_x \cos\alpha + \Lambda^{180} P_y \sin\alpha) d\alpha d\tau \tag{5.8}$$

$$Y^0_{\cos\alpha} = \iint_0^{2\pi} \frac{Y_0'}{\pi} A(\tau, \alpha) \cos\alpha(1 + \Lambda^0 P_x \cos\alpha + \Lambda^0 P_y \sin\alpha) d\alpha d\tau \tag{5.9}$$

$$Y^{180}_{\cos\alpha} = \iint_0^{2\pi} \frac{Y_0'}{\pi} A(\tau, \alpha + \pi) \cos\alpha(1 + \Lambda^{180} P_x \cos\alpha + \Lambda^{180} P_y \sin\alpha) d\alpha d\tau \tag{5.10}$$

$$Y^0_{\sin 2\alpha} = \iint_0^{2\pi} \frac{Y'_0}{\pi} A(\tau,\alpha)\sin 2\alpha(1+\Lambda^0 P_x \cos\alpha + \Lambda^0 P_y \sin\alpha) d\alpha d\tau \tag{5.11}$$

$$Y^{180}_{\sin 2\alpha} = \iint_0^{2\pi} \frac{Y'_0}{\pi} A(\tau,\alpha+\pi)\sin 2\alpha(1+\Lambda^{180} P_x \cos\alpha + \Lambda^{180} P_y \sin\alpha) d\alpha d\tau \tag{5.12}$$

$$Y^0_{\cos 2\alpha} = \iint_0^{\pi} \frac{Y'_0}{\pi} A(\tau,\alpha)\cos 2\alpha(1+\Lambda^0 P_x \cos\alpha + \Lambda^0 P_y \sin\alpha) d\alpha d\tau \tag{5.13}$$

$$Y^{180}_{\cos 2\alpha} = \iint_0^{2\pi} \frac{Y'_0}{\pi} A(\tau,\alpha+\pi)\cos 2\alpha(1+\Lambda^{180} P_x \cos\alpha + \Lambda^{180} P_y \sin\alpha) d\alpha d\tau \tag{5.14}$$

After evaluating the integrals, the following notations were used $a_0^{0,180}(\bar{\tau}) = a_0^{0,180}$, $a_1^{0,180}(\bar{\tau}) = a_1^{0,180}$, $b_1^{0,180}(\bar{\tau}) = b_1^{0,180}$,$b_2^{0,180}(\bar{\tau}) = b_2^{0,180}$, the moments' expressions are:

$$Y^0 = Y_0\Big(a_0^0 + a_1^0 P_x \bar{\Lambda}^0 + b_1^0 P_y \bar{\Lambda}^0\Big), \tag{5.15}$$

$$Y^0_{\sin\alpha} = Y_0\Big(b_1^0 + \frac{b_2^0}{2} P_x \bar{\Lambda}^0 + \Big(\frac{a_0^0}{2} - \frac{a_2^0}{2}\Big) P_y \bar{\Lambda}^0\Big), \tag{5.16}$$

$$Y^0_{\cos\alpha} = Y_0\Big(a_1^0 + \Big(\frac{a_0^0}{2} + \frac{a_2^0}{2}\Big) P_x \bar{\Lambda}^0 + \frac{b_2^0}{2} P_y \bar{\Lambda}^0\Big), \tag{5.17}$$

$$Y^{180} = Y_0\Big(a_0^{180} - a_1^{180} P_x \bar{\Lambda}^{180} - b_1^{180} P_y \bar{\Lambda}^{180}\Big), \tag{5.18}$$

$$Y^{180}_{\sin\alpha} = Y_0\Big(-b_1^{180} + \frac{b_2^{180}}{2} P_x \bar{\Lambda}^{180} + \Big(\frac{a_0^0}{2} - \frac{a_2^{180}}{2}\Big) P_y \bar{\Lambda}^{180}\Big), \text{ and} \tag{5.19}$$

$$Y^{180}_{\cos\alpha} = Y_0\Big(-a_1^{180} + \Big(\frac{a_0^{180}}{2} + \frac{a_2^{180}}{2}\Big) P_x \bar{\Lambda}^{180} + \frac{b_2^{180}}{2} P_y \bar{\Lambda}^{180}\Big), \tag{5.20}$$

where $\bar{\Lambda}^{0,180} = \frac{\sum_i Q_i \Lambda_i}{\sum_i Q_i}$, $Y^{0,180} = \frac{1}{N^{0,180}} \sum_i Q_i$, $Y^{0,180}_{\sin\alpha} = \frac{1}{N^{0,180}} \sum_i \sin\alpha_i$, $Y^{0,180}_{\cos\alpha} = \frac{1}{N^{0,180}} \sum_i \cos\alpha_i$, $Y^{0,180}_{\sin 2\alpha} = \frac{1}{N^{0,180}} \sum_i Q_i \sin 2\alpha_i$, $Y^{0,180}_{\cos 2\alpha} = \frac{1}{N^{0,180}} \sum_i Q_i \cos 2\alpha_i$, and the index i runs over all selected butanol-target events in that kinematic bin for $0°$, and respectively $180°$. The normalization factors N^0 and N^{180} were obtained from carbon-target data. After adding up Y^0 and Y^{180} and sorting the P_x and P_y terms, the normalized unpolarized moment $Y_0 = \int_\tau Y'_0(\tau) d\tau$ will be expressed:

$$Y_0 = \frac{Y^0 + Y^{180}}{a_0^0 + a_0^{180} + P_x\Big(a_1^0 \bar{\Lambda}^0 - a_1^{180} \bar{\Lambda}^{180}\Big) + P_y\Big(b_1^0 \bar{\Lambda}^0 - b_1^{180} \bar{\Lambda}^{180}\Big)}. \tag{5.21}$$

The next step is to replace Y_0 expression in the sum of $Y^0_{\sin\alpha}$ and $Y^{180}_{\sin\alpha}$.

$$\begin{aligned}(Y^0_{\sin\alpha}+Y^{180}_{\sin\alpha})\Big(a^0_0+a^{180}_0+P_x\Big(a^0_1\bar{\Lambda}^0-a^{180}_1\bar{\Lambda}^{180}\Big)+P_y\Big(b^0_1\bar{\Lambda}^0-b^{180}_1\bar{\Lambda}^{180}\Big)\Big)=\\ (Y^0+Y^{180})\Big(b^0_1-b^{180}_1+P_x\Big(\frac{b^0_2}{2}\bar{\Lambda}^0+\frac{b^{180}_2}{2}\bar{\Lambda}^{180}\Big)+\Big(\frac{a^0_0}{2}\bar{\Lambda}^0+\frac{a^{180}_0}{2}\bar{\Lambda}^{180}\Big)P_y-\\ -P_y\Big(\frac{a^0_2}{2}\bar{\Lambda}^0+\frac{a^0_2}{2}\bar{\Lambda}^{180}\Big)\Big)\end{aligned} \tag{5.22}$$

Moving the P_x and P_y terms to the right of the equation yields:

$$\begin{aligned}(a^0_0+a^{180}_0)(Y^0_{\sin\alpha}+Y^{180}_{\sin\alpha})-(Y^0+Y^{180})\Big(b^0_1-b^{180}_1\Big)=\\ P_x\Big[(Y^0+Y^{180})\Big(\frac{b^0_2}{2}\bar{\Lambda}^0+\frac{b^{180}_2}{2}\bar{\Lambda}^{180}\Big)-\\ -(Y^0_{\sin\alpha}+Y^{180}_{\sin\alpha})\Big(a^0_1\bar{\Lambda}^0-a^{180}_1\bar{\Lambda}^0\Big)\Big]+\\ +P_y\Big[(Y^0+Y^{180})\Big(\frac{a^0_0}{2}\bar{\Lambda}^0+\frac{a^{180}_0}{2}\bar{\Lambda}^{180}-\frac{a^0_2}{2}\bar{\Lambda}^0-\frac{a^0_2}{2}\bar{\Lambda}^{180}\Big)\\ -(Y^0_{\sin\alpha}+Y^{180}_{\sin\alpha})\Big(b^0_1\bar{\Lambda}^0-b^{180}_1\bar{\Lambda}^{180}\Big)\Big].\end{aligned} \tag{5.23}$$

In the same way after adding $Y^0_{\cos\alpha}$ and $Y^{180}_{\cos\alpha}$ and plugging in Y_0 the following equation is obtained.

$$\begin{aligned}(a^0_0+a^{180}_0)(Y^0_{\cos\alpha}+Y^{180}_{\cos\alpha})-(Y^0+Y^{180})\Big(a^0_1-a^{180}_1\Big)=\\ P_x\Big[(Y^0+Y^{180})\Big[\frac{a^0_0}{2}\bar{\Lambda}^0+\frac{a^{180}_0}{2}\bar{\Lambda}^{180}+\frac{a^0_2}{2}\bar{\Lambda}^0+\frac{a^{180}_2}{2}\bar{\Lambda}^{180}\Big]-\\ -(Y^0_{\cos\alpha}+Y^{180}_{\cos\alpha})\Big(a^0_1\bar{\Lambda}^0-a^{180}_1\bar{\Lambda}^{180}\Big)\Big]+\\ P_y\Big[(Y^0+Y^{180})\Big(\frac{b^0_2}{2}\bar{\Lambda}^0+\frac{b^0_2}{2}\bar{\Lambda}^{180}\Big)-\\ -(Y^0_{\cos\alpha}+Y^{180}_{\cos\alpha})\Big(b^0_1\bar{\Lambda}^0-b^{180}_1\bar{\Lambda}^{180}\Big)\Big]\end{aligned} \tag{5.24}$$

Next, the Eq. (5.23) is divided by $a_0^0 + a_0^{180}$ and equals:

$$\begin{aligned}(Y^0_{\sin\alpha} + Y^{180}_{\sin\alpha}) - (Y^0 + Y^{180})\Big(\frac{b_1^0 - b_1^{180}}{a_0^0 + a_0^{180}}\Big) = \\ P_x\Big[(Y^0 + Y^{180})\Big(\frac{b_2^0\bar{\Lambda}^0 + b_2^{180}\bar{\Lambda}^{180}}{2(a_0^0 + a_0^{180})}\Big) - \\ -(Y^0_{\sin\alpha} + Y^{180}_{\sin\alpha})\Big(\frac{a_1^0\bar{\Lambda}^0 - a_1^{180}\bar{\Lambda}^0}{a_0^0 + a_0^{180}}\Big)\Big] + \\ +P_y\Big[(Y^0 + Y^{180})\Big(\frac{a_0^0\bar{\Lambda}^0 + a_0^{180}\bar{\Lambda}^{180}}{2(a_0^0 + a_0^{180})} - \frac{a_2^0\bar{\Lambda}^0 + a_2^0\bar{\Lambda}^{180}}{2(a_0^0 + a_0^{180})}\Big) \\ -(Y^0_{\sin\alpha} + Y^{180}_{\sin\alpha})\Big(\frac{b_1^0\bar{\Lambda}^0 - b_1^{180}\bar{\Lambda}^{180}}{a_0^0 + a_0^{180}}\Big)\Big].\end{aligned} \tag{5.25}$$

In the same way dividing Eq. (5.24) by $a_0^0 + a_0^{180}$ gives:

$$\begin{aligned}(Y^0_{\cos\alpha} + Y^{180}_{\cos\alpha}) - (Y^0 + Y^{180})\Big(\frac{a_1^0 - a_1^{180}}{a_0^0 + a_0^{180}}\Big) = \\ P_x\Big[(Y^0 + Y^{180})\Big[\frac{a_0^0\bar{\Lambda}^0 + a_0^{180}\bar{\Lambda}^{180}}{2(a_0^0 + a_0^{180})} + \frac{a_2^0\bar{\Lambda}^0 + a_2^{180}\bar{\Lambda}^{180}}{2(a_0^0 + a_0^{180})}\Big] - \\ -(Y^0_{\cos\alpha} + Y^{180}_{\cos\alpha})\Big(\frac{a_1^0\bar{\Lambda}^0 - a_1^{180}\bar{\Lambda}^{180}}{a_0^0 + a_0^{180}}\Big)\Big] + \\ P_y\Big[(Y^0 + Y^{180})\Big(\frac{b_2^0\bar{\Lambda}^0 + b_2^0\bar{\Lambda}^{180}}{2(a_0^0 + a_0^{180})}\Big) - \\ -(Y^0_{\cos\alpha} + Y^{180}_{\cos\alpha})\Big(\frac{b_1^0\bar{\Lambda}^0 - b_1^{180}\bar{\Lambda}^{180}}{a_0^0 + a_0^{180}}\Big)\Big].\end{aligned} \tag{5.26}$$

The Fourier coefficients from butanol data cannot be determined, but their ratios are considered to be equal to the ratios of the Fourier coefficients from carbon data. To get the coefficients' ratios from carbon, the moments are expressed in the same way as the butanol moments as shown in Eqs. (5.15) – (5.20), but this time the P_x and P_y terms disappear since the carbon target is unpolarized.

$$Y^0_C = a^0_{0,C} Y_{0,C} \tag{5.27}$$

$$Y^0_{\sin\alpha,C} = b^0_{1,C} Y_{0,C} \tag{5.28}$$

$$Y^0_{\cos\alpha,C} = a^0_{1,C} Y_{0,C} \tag{5.29}$$

$$Y^0_{\sin 2\alpha,C} = b^0_{2,C} Y_{0,C} \tag{5.30}$$

$$Y^0_{\cos 2\alpha,C} = a^0_{2,C} Y_{0,C} \tag{5.31}$$

$$Y^{180}_{C} = a^{180}_{0,C} Y_{0,C} \tag{5.32}$$

$$Y^{180}_{\sin \alpha,C} = -b^{180}_{1,C} Y_{0,C} \tag{5.33}$$

$$Y^{180}_{\cos \alpha,C} = -a^{180}_{1,C} Y_{0,C} \tag{5.34}$$

$$Y^{180}_{\sin 2\alpha,C} = b^{180}_{2,C} Y_{0,C} \tag{5.35}$$

$$Y^{180}_{\cos 2\alpha,C} = a^{180}_{2,C} Y_{0,C} \tag{5.36}$$

Using these carbon yields Eq. (5.25) becomes:

$$\begin{aligned}
(Y^0_{\sin\alpha} + Y^{180}_{\sin\alpha}) - (Y^0 + Y^{180})\Big(\frac{Y^0_{\sin\alpha,C} + Y^{180}_{\sin\alpha,C}}{Y^0_C + Y^{180}_C}\Big) = \\
P_x\Big[(Y^0 + Y^{180})\Big(\frac{Y^0_{\sin 2\alpha,C}\bar{\Lambda}^0 + Y^{180}_{\sin 2\alpha,C}\bar{\Lambda}^{180}}{2(Y^0_C + Y^{180}_C)}\Big) - \\
-(Y^0_{\sin\alpha} + Y^{180}_{\sin\alpha})\Big(\frac{Y^0_{\cos\alpha,C}\bar{\Lambda}^0 + Y^{180}_{\cos\alpha,C}\bar{\Lambda}^0}{Y^0_C + Y^{180}_C}\Big)\Big] + \\
+P_y\Big[(Y^0 + Y^{180})\Big(\frac{Y^0_C\bar{\Lambda}^0 + Y^{180}_C\bar{\Lambda}^{180}}{2(Y^0_C + Y^{180}_C)} - \frac{Y^0_{\cos 2\alpha,C}\bar{\Lambda}^0 + Y^{180}_{\cos 2\alpha,C}\bar{\Lambda}^{180}}{2(Y^0_C + Y^{180}_C)}\Big) \\
-(Y^0_{\sin\alpha} + Y^{180}_{\sin\alpha})\Big(\frac{Y^0_{\sin\alpha,C}\bar{\Lambda}^0 + Y^{180}_{\sin\alpha,C}\bar{\Lambda}^{180}}{Y^0_C + Y^{180}_C}\Big)\Big].
\end{aligned} \tag{5.37}$$

Similarly Eq. (5.26) is rewritten as:

$$\begin{aligned}
(Y^0_{\cos\alpha} + Y^{180}_{\cos\alpha}) - (Y^0 + Y^{180})\Big(\frac{Y^0_{\cos\alpha,C} + Y^{180}_{\cos\alpha,C}}{Y^0_C + Y^{180}_C}\Big) = \\
P_x\Big[(Y^0 + Y^{180})\Big[\frac{Y^0_C\bar{\Lambda}^0 + Y^{180}_C\bar{\Lambda}^{180}}{2(Y^0_C + Y^{180}_C)} + \frac{Y^0_{\cos 2\alpha,C}\bar{\Lambda}^0 + Y^{180}_{\cos 2\alpha,C}\bar{\Lambda}^{180}}{2(Y^0_C + Y^{180}_C)}\Big] - \\
-(Y^0_{\cos\alpha} + Y^{180}_{\cos\alpha})\Big(\frac{Y^0_{\cos\alpha,C}\bar{\Lambda}^0 + Y^{180}_{\cos\alpha,C}\bar{\Lambda}^{180}}{Y^0_C + Y^{180}_C}\Big)\Big] + \\
P_y\Big[(Y^0 + Y^{180})\Big(\frac{Y^0_{\sin 2\alpha,C}\bar{\Lambda}^0 + Y^0_{\sin 2\alpha,C}\bar{\Lambda}^{180}}{2(Y^0_C + Y^{180}_C)}\Big) - \\
-(Y^0_{\cos\alpha} + Y^{180}_{\cos\alpha})\Big(\frac{Y^0_{\sin\alpha,C}\bar{\Lambda}^0 + Y^{180}_{\sin\alpha,C}\bar{\Lambda}^{180}}{Y^0_C + Y^{180}_C}\Big)\Big].
\end{aligned} \tag{5.38}$$

To determine the unknown P_x and P_y the system of two equations (Eq. (5.37), Eq. (5.38)) with two unknowns was solved. To quantify the contribution of the

correction to the final value of the observable, the following substitutions were made.

$$c_1 = \frac{Y^0_{\sin\alpha,C} + Y^{180}_{\sin\alpha,C}}{Y^0_C + Y^{180}_C} \tag{5.39}$$

$$c_2 = \frac{Y^0_{\sin 2\alpha,C}\bar{\Lambda}^0 + Y^{180}_{\sin 2\alpha,C}\bar{\Lambda}^{180}}{2(Y^0_C + Y^{180}_C)} \tag{5.40}$$

$$c_3 = \frac{Y^0_{\cos\alpha,C}\bar{\Lambda}^0 + Y^{180}_{\cos\alpha,C}\bar{\Lambda}^{180}}{Y^0_C + Y^{180}_C} \tag{5.41}$$

$$c_4 = \frac{Y^0_C\bar{\Lambda}^0 + Y^{180}_C\bar{\Lambda}^{180}}{2(Y^0_C + Y^{180}_C)} \tag{5.42}$$

$$c_5 = \frac{Y^0_{\cos 2\alpha,C}\bar{\Lambda}^0 + Y^{180}_{\cos 2\alpha,C}\bar{\Lambda}^{180}}{2(Y^0_C + Y^{180}_C)} \tag{5.43}$$

$$c_6 = \frac{Y^0_{\sin\alpha,C}\bar{\Lambda}^0 + Y^{180}_{\sin\alpha,C}\bar{\Lambda}^{180}}{Y^0_C + Y^{180}_C} \tag{5.44}$$

$$c_7 = \frac{Y^0_{\cos\alpha,C} + Y^{180}_{\cos\alpha,C}}{Y^0_C + Y^{180}_C} \tag{5.45}$$

While comparing these coefficients extracted from carbon data to those from polyethylene data, one could see that within uncertainties they are almost the same as shown in Fig. 5.2; and for this reason carbon data was combined with polyethylene data in order to improve the statistics when determining the acceptance-corrections factors. This is also showing that since the carbon acceptance resembles the polyethylene target acceptance, it is expected that the butanol target to show the same acceptance differences.

Substituting the expressions for c_1 and c_7 to Eq. (5.37) and dividing by $c_4(Y^0 + Y^{180})$ leads to:

$$\frac{1}{c_4}\frac{Y^0_{\sin\alpha} + Y^{180}_{\sin\alpha}}{Y^0 + Y^{180}} - \frac{c_1}{c_4} = P_x\Big(\frac{c_2}{c_4} - \frac{c_3}{c_4}\frac{Y^0_{\sin\alpha} + Y^{180}_{\sin\alpha}}{Y^0_C + Y^{180}_C}\Big) + P_y\Big(1 - \frac{c_5}{c_4} - \frac{c_6}{c_4}\frac{Y^0_{\sin\alpha} + Y^{180}_{\sin\alpha}}{Y^0_C + Y^{180}_C}\Big). \tag{5.46}$$

Similarly Eq. (5.38) becomes :

$$\frac{1}{c_4}\frac{Y^0_{\cos\alpha} + Y^{180}_{\cos\alpha}}{Y^0 + Y^{180}} - \frac{c_7}{c_4} = P_x\Big(1 + \frac{c_5}{c_4} - \frac{c_3}{c_4}\frac{Y^0_{\sin\alpha} + Y^{180}_{\cos\alpha}}{Y^0_C + Y^{180}_C}\Big) + P_y\Big(\frac{c_2}{c_4} - \frac{c_6}{c_4}\frac{Y^0_{\cos\alpha} + Y^{180}_{\cos\alpha}}{Y^0_C + Y^{180}_C}\Big), \tag{5.47}$$

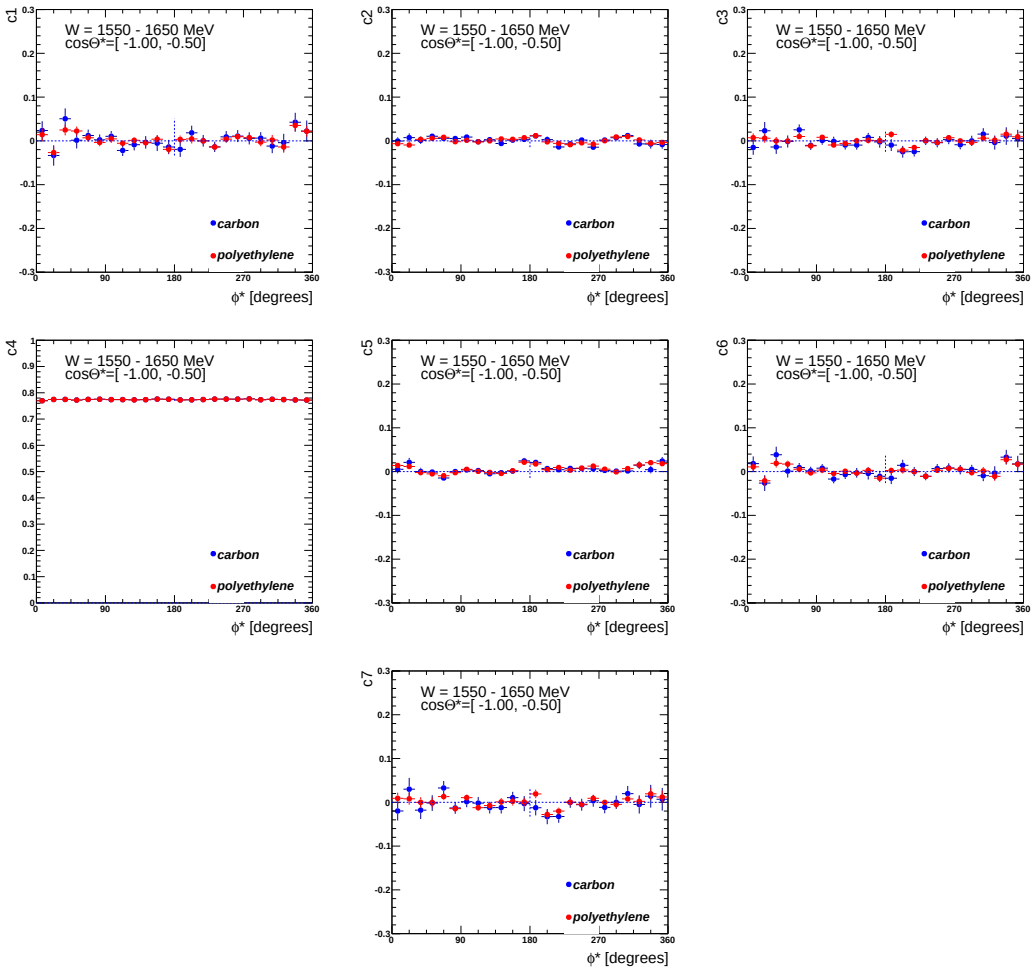

Figure 5.2: The coefficients c_1, c_2, c_3, c_4, c_5, c_6, and c_7 for carbon and polyethylene data for $W = 1550 - 1650$ MeV and $\cos\theta^* = [-1, -0.5]$.

and defining :

$$\delta_1 = -\frac{c_5}{c_4} - \frac{c_6}{c_4}\frac{Y^0_{\sin\alpha} + Y^{180}_{\sin\alpha}}{Y^0_C + Y^{180}_C} \tag{5.48}$$

$$\delta_2 = \frac{c_5}{c_4} - \frac{c_3}{c_4}\frac{Y^0_{\sin\alpha} + Y^{180}_{\cos\alpha}}{Y^0_C + Y^{180}_C} \tag{5.49}$$

On the right side of Eq. (5.46) the leading term is the P_y term and on the right side of Eq. (5.47) the leading term is the P_x term, but the $P_y\delta_1$ and $P_x\delta_2$ corrections are negligible compared to the P_x and P_y values. The largest contribution that remains is the ratio $\frac{c_1}{c_4}$ (Fig. 5.3, left) present on the left side of Eq. (5.46) and $\frac{c_7}{c_4}$ (Fig. 5.3, right) present on the left side of Eq. (5.47). When using these correction factors to account

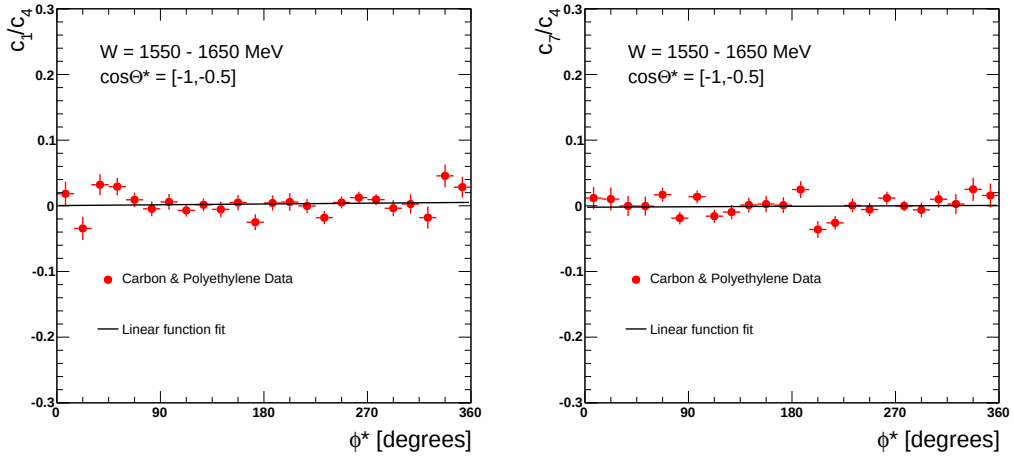

Figure 5.3: The correction terms $\frac{c_1}{c_4}$ and $\frac{c_7}{c_4}$ for the kinematic bin $W = 1550 - 1650$ MeV and $\cos\theta^* = [-1, -0.5]$ and where the linear fit indicates an average zero offset less than 0.01.

for the acceptance changes, the statistical uncertainties of the observables increase significantly due to the still low carbon+polyethylene statistics and thus they will not be further considered in this analysis beyond estimating the systematic uncertainties arising from the changing acceptance. These correction terms (Fig. 5.3) indicate a maximum contribution to the systematic uncertainty for the observables P_x and P_y of less than 0.01 (Section 5.3); in this example it is, in fact, consistent with zero. Also from Fig. 5.1 (upper right plot) one can see that when combining all topologies the acceptance effect is diminished.

After estimating the systematic uncertainties due to the changing acceptance, the expressions for P_x and P_y are derived assuming the acceptance for the positive target polarization run groups is the same as the acceptance corresponding to the negative target polarization run groups, the following simplifications were made: $a_0^0 = a_0^{180} = a_0$, $a_1^0 = a_1^{180} = a_1$, $b_1^0 = b_1^{180} = b_1$, $a_2^0 = a_2^{180} = a_2$, and $b_2^0 = b_2^{180} = b_2$ and in

this case, the Eqs. (5.5) – (5.14) become:

$$Y^0 = Y_0\Big(a_0 + a_1 P_x \bar{\Lambda}^0 + b_1 P_y \bar{\Lambda}^0\Big) \tag{5.50}$$

$$Y^0_{\sin\alpha} = Y_0\Big(b_1 + \frac{b_2}{2} P_x \bar{\Lambda}^0 + \Big(\frac{a_0}{2} - \frac{a_2}{2}\Big) P_y \bar{\Lambda}^0\Big), \tag{5.51}$$

$$Y^0_{\cos\alpha} = Y_0\Big(a_1 + \Big(\frac{a_0}{2} + \frac{a_2}{2}\Big) P_x \bar{\Lambda}^0 + \frac{b_2}{2} P_y \bar{\Lambda}^0\Big), \tag{5.52}$$

$$Y^0_{\sin 2\alpha} = Y_0\Big(b_2 + \frac{b_1}{2} P_x \bar{\Lambda}^0 + \frac{a_1}{2} P_y \bar{\Lambda}^0\Big), \tag{5.53}$$

$$Y^0_{\cos 2\alpha} = Y_0\Big(a_2 + \frac{a_1}{2} P_x \bar{\Lambda}^0 - \frac{b_1}{2} P_y \bar{\Lambda}^0\Big), \tag{5.54}$$

$$Y^{180} = Y_0\Big(a_0 - a_1 P_x \bar{\Lambda}^{180} - b_1 P_y \bar{\Lambda}^{180}\Big), \tag{5.55}$$

$$Y^{180}_{\sin\alpha} = Y_0\Big(- b_1 + \frac{b_2}{2} P_x \bar{\Lambda}^{180} + \Big(\frac{a_0}{2} - \frac{a_2}{2}\Big) P_y \bar{\Lambda}^{180}\Big), \tag{5.56}$$

$$Y^{180}_{\cos\alpha} = Y_0\Big(- a_1 + \Big(\frac{a_0}{2} + \frac{a_2}{2}\Big) P_x \bar{\Lambda}^{180} + \frac{b_2}{2} P_y \bar{\Lambda}^{180}\Big), \tag{5.57}$$

$$Y^{180}_{\sin 2\alpha} = Y_0\Big(b_2 - \frac{b_1}{2} P_x \bar{\Lambda}^{180} - \frac{a_1}{2} P_y \bar{\Lambda}^{180}\Big), \text{and} \tag{5.58}$$

$$Y^{180}_{\cos 2\alpha} = Y_0\Big(a_2 - \frac{a_1}{2} P_x \bar{\Lambda}^{180} + \frac{b_1}{2} P_y \bar{\Lambda}^{180}\Big). \tag{5.59}$$

Using the above yields we express the Fourier coefficients:

$$a_0 = \frac{Y^0 \bar{\Lambda}^{180} + Y^{180} \bar{\Lambda}^0}{Y_0(\bar{\Lambda}^0 + \bar{\Lambda}^{180})} \tag{5.60}$$

$$a_1 = \frac{Y^0_{\cos\alpha} \bar{\Lambda}^{180} - Y^{180}_{\cos\alpha} \bar{\Lambda}^0}{Y_0(\bar{\Lambda}^0 + \bar{\Lambda}^{180})}, \tag{5.61}$$

$$b_1 = \frac{Y^0_{\sin\alpha} \bar{\Lambda}^{180} - Y^{180}_{\sin\alpha} \bar{\Lambda}^0}{Y_0(\bar{\Lambda}^0 + \bar{\Lambda}^{180})}, \tag{5.62}$$

$$a_2 = \frac{Y^0_{\cos 2\alpha} \bar{\Lambda}^{180} + Y^{180}_{\cos 2\alpha} \bar{\Lambda}^0}{Y_0(\bar{\Lambda}^0 + \bar{\Lambda}^{180})}, \text{and} \tag{5.63}$$

$$b_2 = \frac{Y^0_{\sin 2\alpha} \bar{\Lambda}^{180} + Y^{180}_{\sin 2\alpha} \bar{\Lambda}^0}{Y_0(\bar{\Lambda}^0 + \bar{\Lambda}^{180})}. \tag{5.64}$$

After replacing the Fourier coefficients into the expressions of the moments, the following system of equations is solved for P_x and P_y:

$$Y^0_{\sin\alpha} + Y^{180}_{\sin\alpha} = Y_0\Big(\frac{b_2}{2} P_x(\bar{\Lambda}^0 + \bar{\Lambda}^{180}) + \Big(\frac{a_0}{2} - \frac{a_2}{2}\Big) P_y(\bar{\Lambda}^0 + \bar{\Lambda}^{180})\Big), \text{and} \tag{5.65}$$

$$Y^0_{\cos\alpha} + Y^{180}_{\cos\alpha} = Y_0\Big(\Big(\frac{a_0}{2} + \frac{a_2}{2}\Big) P_x(\bar{\Lambda}^0 + \bar{\Lambda}^{180}) + \frac{b_2}{2} P_y(\bar{\Lambda}^0 + \bar{\Lambda}^{180})\Big), \tag{5.66}$$

which yields the observables P_x and P_y.

$$P_x = 2\frac{(Y^0_{\sin 2\alpha}\bar{\Lambda}^{180} + Y^{180}_{\sin 2\alpha}\bar{\Lambda}^0)(Y^0_{\sin\alpha} + Y^{180}_{\sin\alpha})}{(Y^0_{\sin 2\alpha}\bar{\Lambda}^{180} + Y^{180}_{\sin 2\alpha}\bar{\Lambda}^0)^2 + (Y^0_{\cos 2\alpha}\bar{\Lambda}^{180} + Y^{180}_{\cos 2\alpha}\bar{\Lambda}^0)^2 - (Y^0\bar{\Lambda}^{180} + Y^{180}\bar{\Lambda}^0)^2} - \frac{[(Y^0\bar{\Lambda}^{180} + Y^{180}\bar{\Lambda}^0) - (Y^0_{\cos 2\alpha}\bar{\Lambda}^{180} + Y^{180}_{\cos 2\alpha}\bar{\Lambda}^0)](Y^0_{\cos\alpha} + Y^{180}_{\cos\alpha})}{(Y^0_{\sin 2\alpha}\bar{\Lambda}^{180} + Y^{180}_{\sin 2\alpha}\bar{\Lambda}^0)^2 + (Y^0_{\cos 2\alpha}\bar{\Lambda}^{180} + Y^{180}_{\cos 2\alpha}\bar{\Lambda}^0)^2 - (Y^0\bar{\Lambda}^{180} + Y^{180}\bar{\Lambda}^0)^2} \tag{5.67}$$

$$P_y = 2\frac{[(Y^0\bar{\Lambda}^{180} + Y^{180}\bar{\Lambda}^0) + (Y^0_{\cos 2\alpha}\bar{\Lambda}^{180} + Y^{180}_{\cos 2\alpha}\bar{\Lambda}^0)](Y^0_{\sin\alpha} + Y^{180}_{\sin\alpha})}{(Y^0\bar{\Lambda}^{180} + Y^{180}\bar{\Lambda}^0)^2 - (Y^0_{\cos 2\alpha}\bar{\Lambda}^{180} + Y^{180}_{\cos 2\alpha}\bar{\Lambda}^0)^2 - (Y^0_{\sin 2\alpha}\bar{\Lambda}^{180} + Y^{180}_{\sin 2\alpha}\bar{\Lambda}^0)^2} \frac{-(Y^0_{\sin 2\alpha}\bar{\Lambda}^{180} + Y^{180}_{\sin 2\alpha}\bar{\Lambda}^0)(Y^0_{\cos\alpha} + Y^{180}_{\cos\alpha})}{(Y^0\bar{\Lambda}^{180} + Y^{180}\bar{\Lambda}^0)^2 - (Y^0_{\cos 2\alpha}\bar{\Lambda}^{180} + Y^{180}_{\cos 2\alpha}\bar{\Lambda}^0)^2 - (Y^0_{\sin 2\alpha}\bar{\Lambda}^{180} + Y^{180}_{\sin 2\alpha}\bar{\Lambda}^0)^2} \tag{5.68}$$

These expressions (Eq. (5.67) and Eq. (5.68)) were used in the extraction of the polarization observables P_x and P_y.

5.2 Moments' Method: The Extraction Of The Helicity-Dependent Observables

In order to solve for the helicity-dependent observables $I^\odot$, $P_x^\odot$ and $P_y^\odot$, the moments for the two possible orientations 0° and 180° of the target polarization and the two helicity states $(+1, -1)$ are written:

$$\begin{aligned}
Y^{\pm 0} &= \frac{1}{2\pi}\int_0^{2\pi} Y'_0 A(\alpha)[1 + \Lambda^0 P_x \cos\alpha + \Lambda^0 P_y \sin\alpha + \\
&\quad \pm \delta_\odot (I^\odot + \Lambda^0 P_x^\odot \cos\alpha + \Lambda^0 P_y^\odot \sin\alpha)]d\alpha, \\
Y^{\pm 180} &= \frac{1}{2\pi}\int_0^{2\pi} Y'_0 A(\alpha)[1 + \Lambda^{180} P_x \cos\alpha + \Lambda^{180} P_y \sin\alpha + \\
&\quad + \delta_\odot (I^\odot + \Lambda^{180} P_x^\odot \cos\alpha + \Lambda^{180} P_y^\odot \sin\alpha)d\alpha, \\
Y^{\pm 0}_{\sin\alpha} &= \frac{1}{2\pi}\int_0^{2\pi} Y'_0 A(\alpha)\sin\alpha[1 + \Lambda^0 P_x \cos\alpha + \Lambda^0 P_y \sin\alpha - \\
&\quad \pm \delta_\odot (I^\odot + \Lambda^0 P_x^\odot \cos\alpha + \Lambda^0 P_y^\odot \sin\alpha)]d\alpha, \\
Y^{\pm 180}_{\sin\alpha} &= \frac{1}{2\pi}\int_0^{2\pi} Y'_0 A(\alpha+\pi)\sin\alpha[1 + \Lambda^{180} P_x \cos\alpha + \Lambda^{180} P_y \sin\alpha + \\
&\quad \pm \delta_\odot (I^\odot + \Lambda^{180} P_x^\odot \cos\alpha + \Lambda^{180} P_y^\odot \sin\alpha)]d\alpha,
\end{aligned} \tag{5.69}$$

$$Y^{\pm 0}_{\cos\alpha} = \frac{1}{2\pi}\int_0^{2\pi} Y'_0 A(\alpha)\cos\alpha[1 + \Lambda^0 P_x \cos\alpha + \Lambda^0 P_y \sin\alpha + \\ \pm \delta_\odot(I^\odot + \Lambda^0 P_x^\odot \cos\alpha + \Lambda^0 P_y^\odot \sin\alpha)]d\alpha, \tag{5.70}$$

$$Y^{\pm 180}_{\cos\alpha} = \frac{1}{2\pi}\int_0^{2\pi} Y'_0 A(\alpha+\pi)\cos\alpha[1 + \Lambda^{180} P_x \cos\alpha + \Lambda^{180} P_y \sin\alpha + \\ \pm \delta_\odot(I^\odot + \Lambda^{180} P_x^\odot \cos\alpha + \Lambda^{180} P_y^\odot \sin\alpha)]d\alpha, \tag{5.71}$$

$$Y^{\pm 0}_{\sin 2\alpha} = \frac{1}{2\pi}\int_0^{2\pi} Y'_0 A(\alpha)\sin 2\alpha[1 + \Lambda^0 P_x \cos\alpha + \Lambda^0 P_y \sin\alpha + \\ \pm \delta_\odot(I^\odot + \Lambda^0 P_x^\odot \cos\alpha + \Lambda^0 P_y^\odot \sin\alpha)]d\alpha, \tag{5.72}$$

$$Y^{\pm 180}_{\sin 2\alpha} = \frac{1}{2\pi}\int_0^{2\pi} Y'_0 A(\alpha+\pi)\sin 2\alpha[1 + \Lambda^{180} P_x \cos\alpha + \Lambda^{180} P_y \sin\alpha + \\ \pm \delta_\odot(I^\odot + \Lambda^{180} P_x^\odot \cos\alpha + \Lambda^{180} P_y^\odot \sin\alpha)]d\alpha, \tag{5.73}$$

$$Y^{\pm 0}_{\cos 2\alpha} = \frac{1}{2\pi}\int_0^{2\pi} Y'_0 A(\alpha)\cos 2\alpha[1 + \Lambda^0 P_x \cos\alpha + \Lambda^0 P_y \sin\alpha + \\ \pm \delta_\odot(I^\odot + \Lambda^0 P_x^\odot \cos\alpha + \Lambda^0 P_y^\odot \sin\alpha)]d\alpha, \text{and} \tag{5.74}$$

$$Y^{\pm 180}_{\cos 2\alpha} = \frac{1}{2\pi}\int_0^{2\pi} Y'_0 A(\alpha+\pi)\cos 2\alpha[1 + \Lambda^{180} P_x \cos\alpha + \Lambda^{180} P_y \sin\alpha + \\ \pm \delta_\odot(I^\odot + \Lambda^{180} P_x^\odot \cos\alpha + \Lambda^{180} P_y^\odot \sin\alpha)]d\alpha. \tag{5.75}$$

After evaluating these integrals, subtracting from the (+0) moments the (−0) moments, respectively from (+180) moments the (−180) moments the helicity inde-

pendent part cancels out and the resulting differences are:

$$Y^{+0} - Y^{-0} = \bar{\delta}_{\odot} Y_0 \Big(a_0^0 I^{\odot} + a_1^0 P_x^{\odot} \bar{\Lambda}^0 + b_1^0 P_y^{\odot} \bar{\Lambda}^0 \Big), \tag{5.76}$$

$$Y^{+180} - Y^{-180} = \bar{\delta}_{\odot} Y_0 \Big(a_0^{180} I^{\odot} - a_1^{180} P_x^{\odot} \bar{\Lambda}^{180} - b_1^{180} P_y^{\odot} \bar{\Lambda}^{180} \Big), \tag{5.77}$$

$$Y^{+0}_{\sin\alpha} - Y^{-0}_{\sin\alpha} = \bar{\delta}_{\odot} Y_0 \Big(b_1^0 I^{\odot} + \frac{b_2^0}{2} P_x^{\odot} \bar{\Lambda}^0 + \Big(\frac{a_0^0}{2} - \frac{a_2^0}{2} \Big) P_y^{\odot} \bar{\Lambda}^0 \Big), \tag{5.78}$$

$$Y^{+180}_{\sin\alpha} - Y^{-180}_{\sin\alpha} = \bar{\delta}_{\odot} Y_0 \Big(- b_1^{180} I^{\odot} + \frac{b_2^{180}}{2} P_x^{\odot} \bar{\Lambda}^{180} + \Big(\frac{a_0^{180}}{2} - \frac{a_2^{180}}{2} \Big) P_y^{\odot} \bar{\Lambda}^{180} \Big), \tag{5.79}$$

$$Y^{+0}_{\cos\alpha} - Y^{-0}_{\cos\alpha} = \bar{\delta}_{\odot} Y_0 \Big(a_1^0 I^{\odot} + \Big(\frac{a_0^0}{2} + \frac{a_2^0}{2} \Big) P_x^{\odot} \bar{\Lambda}^0 + \frac{b_2^0}{2} P_y^{\odot} \bar{\Lambda}^0 \Big), \tag{5.80}$$

$$Y^{+180}_{\cos\alpha} - Y^{-180}_{\cos\alpha} = \bar{\delta}_{\odot} Y_0 \Big(- a_1^{180} I^{\odot} + \Big(\frac{a_0^{180}}{2} + \frac{a_2^{180}}{2} \Big) P_x^{\odot} \bar{\Lambda}^{180} + \frac{b_2^{180}}{2} P_y^{\odot} \bar{\Lambda}^{180} \Big), \tag{5.81}$$

$$Y^{+0}_{\sin 2\alpha} - Y^{-0}_{\sin 2\alpha} = \bar{\delta}_{\odot} Y_0 \Big(b_2^0 I^{\odot} + \frac{b_1^0}{2} \bar{\Lambda}^0 P_x^{\odot} + \frac{a_1^0}{2} \bar{\Lambda}^0 P_y^{\odot} \Big), \tag{5.82}$$

$$Y^{+180}_{\sin 2\alpha} - Y^{-180}_{\sin 2\alpha} = \bar{\delta}_{\odot} Y_0 \Big(b_2^{180} I^{\odot} - \frac{b_1^{180}}{2} \bar{\Lambda}^{180} P_x^{\odot} - \frac{a_1^{180}}{2} \bar{\Lambda}^{180} P_y^{\odot} \Big), \tag{5.83}$$

$$Y^{+0}_{\cos 2\alpha} - Y^{-0}_{\cos 2\alpha} = \bar{\delta}_{\odot} Y_0 \Big(a_2^0 I^{\odot} + \frac{a_1^0}{2} \bar{\Lambda}^0 P_x^{\odot} - \frac{b_1^0}{2} \bar{\Lambda}^0 P_y^{\odot} \Big), \text{and} \tag{5.84}$$

$$Y^{+180}_{\cos 2\alpha} - Y^{-180}_{\cos 2\alpha} = \bar{\delta}_{\odot} Y_0 \Big(a_2^{180} I^{\odot} - \frac{a_1^{180}}{2} \bar{\Lambda}^{180} P_x^{\odot} + \frac{b_1^{180}}{2} \bar{\Lambda}^{180} P_y^{\odot} \Big), \tag{5.85}$$

where $\bar{\delta}_{\odot} = \frac{\sum_i Q_i \delta_{\odot}^i}{\sum_i Q_i}$ being the average degree of photon beam polarization for that kinematic bin, $Y^{\pm 0,180} = \frac{1}{N^{0,180}} \sum_i Q_i H_i$, $Y^{\pm 0,180}_{\sin\alpha} = \frac{1}{N^{0,180}} \sum_i H_i \sin\alpha_i$, $Y^{\pm 0,180}_{\sin 2\alpha} = \frac{1}{N^{0,180}} \sum_i Q_i H_i \sin 2\alpha_i$, $Y^{\pm 0,180}_{\cos\alpha} = \frac{1}{N^{0,180}} \sum_i H_i \cos\alpha_i$, $Y^{\pm 0,180}_{\cos 2\alpha} = \frac{1}{N^{0,180}} \sum_i Q_i H_i \cos 2\alpha_i$, and the index i runs over all events in that kinematic bin and H_i is the photon helicity corresponding to that event.

One assumption of the use of the Q_i values in the expressions of the moments is that the background is unpolarized. This assumption is fulfilled for the polarization observables P_x, P_y, $P_x^{\odot}$, and $P_y^{\odot}$. It is not fulfilled for the observable $I^{\odot}$ as double-pion photoproduction off bound nucleons also give helicity asymmetries in the cross section. The factor Q_i is included in the expression for $Y^{\pm 0,180}$. It takes into account the polarized background and making the assumption that the signal and background asymmetries are equal; i.e. the polarization observable $I^{\odot}$ is assumed to be equal for photoproduction off free and bound protons. The $Y^{\pm 0,180}$ moments were only used in

the extraction of $I^{\odot}$.

The difference between the moments corresponding to the helicity ± 1 states is expressed:

$$Y^{+} - Y^{-} = Y^{+0} - Y^{-0} + Y^{+180} - Y^{-180} = \delta_{\odot} Y_0 (a_0^0 + a_0^{180}) \Big[(I^{\odot} + \Big(\frac{a_1^0 \bar{\Lambda}^0 - a_1^{180} \bar{\Lambda}^{180}}{a_0^0 + a_0^{180}} \Big) P_x^{\odot} + \Big(\frac{b_1^0 \bar{\Lambda}^0 - b_1^{180} \bar{\Lambda}^{180}}{a_0^0 + a_0^{180}} \Big) P_y^{\odot} \Big]. \tag{5.86}$$

Similarly combining $Y^{\pm}_{\sin\alpha}$ moment differences and factorizing out $(a_0^0 + a_0^{180})$ leads to:

$$Y^{+}_{\sin\alpha} - Y^{-}_{\sin\alpha} = Y^{+0}_{\sin\alpha} - Y^{-0}_{\sin\alpha} + Y^{+180}_{\sin\alpha} - Y^{-180}_{\sin\alpha} = \delta_{\odot} Y_0 (a_0^0 + a_0^{180}) \Big(\frac{b_1^0 - b_1^{180}}{a_0^0 + a_0^{180}} \Big) I^{\odot} + + \Big(\frac{b_2^0 \bar{\Lambda}^0 + b_2^{180} \bar{\Lambda}^{180}}{2(a_0^0 + a_0^{180})} \Big) P_x^{\odot} + \Big(\frac{a_0^0 \bar{\Lambda}^0 + a_0^{180} \bar{\Lambda}^{180}}{2(a_0^0 + a_0^{180})} - \frac{a_2^0 \bar{\Lambda}^0 + a_2^{180} \bar{\Lambda}^{180}}{2(a_0^0 + a_0^{180})} \Big) P_y^{\odot}. \tag{5.87}$$

Adding the $Y^{+0}_{\cos\alpha} - Y^{-0}_{\cos\alpha}$ and $Y^{+180}_{\cos\alpha} - Y^{-180}_{\cos\alpha}$ and factorizing out $(a_0^0 + a_0^{180})$ the following expression is obtained:

$$Y^{+}_{\cos\alpha} - Y^{-}_{\cos\alpha} = Y^{+0}_{\cos\alpha} - Y^{-0}_{\cos\alpha} + Y^{+180}_{\cos\alpha} - Y^{-180}_{\cos\alpha} = \delta_{\odot} Y_0 (a_0^0 + a_0^{180}) \Big[\frac{a_1^0 - a_1^{180}}{a_0^0 + a_0^{180}} I^{\odot} + \Big(\frac{a_0^0 \bar{\Lambda}^0 + a_0^{180} \bar{\Lambda}^{180}}{2(a_0^0 + a_0^{180})} + \frac{a_2^0 \bar{\Lambda}^0 + a_2^{180} \bar{\Lambda}^{180}}{2(a_0^0 + a_0^{180})} \Big) P_x^{\odot} + \frac{b_2^0 \bar{\Lambda}^0 + b_2^{180} \bar{\Lambda}^{180}}{2(a_0^0 + a_0^{180})} P_x^{\odot} \Big]. \tag{5.88}$$

Rearranging Eq. (5.86) and replacing the coefficient ratios with carbon yield (Eqs. (5.27 - 5.36)) ratios gives:

$$\frac{Y^{+} - Y^{-}}{\delta_{\odot} Y_0 (a_0^0 + a_0^{180})} = I^{\odot} + \Big(\frac{Y^0_{\cos\alpha, C} \bar{\Lambda}^0 + Y^{180}_{\cos\alpha, C} \bar{\Lambda}^{180}}{Y_C^0 + Y_C^{180}} \Big) P_x^{\odot} + + \Big(\frac{Y^0_{\sin\alpha, C} \bar{\Lambda}^0 + Y^{180}_{\sin\alpha, C} \bar{\Lambda}^{180}}{Y_C^0 + Y_C^{180}} \Big) P_y^{\odot}. \tag{5.89}$$

Similarly Eq. (5.87) becomes:

$$\frac{Y^{+}_{\sin\alpha} - Y^{-}_{\sin\alpha}}{\delta_{\odot} Y_0 (a_0^0 + a_0^{180})} = \Big(\frac{Y^0_{\sin\alpha, C} + Y^{180}_{\sin\alpha, C}}{Y_C^0 + Y_C^{180}} \Big) I^{\odot} + \Big(\frac{Y^0_{\sin 2\alpha, C} \bar{\Lambda}^0 + Y^{180}_{\sin 2\alpha, C} \bar{\Lambda}^{180}}{2(Y_0^0 + Y_C^{180})} \Big) P_x^{\odot} + + \Big(\frac{Y_C^0 \bar{\Lambda}^0 + Y_C^{180} \bar{\Lambda}^{180}}{2(Y_C^0 + Y_C^{180})} - \frac{Y^0_{\cos 2\alpha, C} \bar{\Lambda}^0 + Y^{180}_{\cos 2\alpha, C} \bar{\Lambda}^{180}}{2(Y_C^0 + Y_C^{180})} \Big) P_y^{\odot}. \tag{5.90}$$

And in the same way, Eq. (5.88) becomes:

$$\frac{Y^{+}_{\cos\alpha} - Y^{-}_{\cos\alpha}}{\delta_{\odot} Y_0 (a_0^0 + a_0^{180})} = \frac{Y^{0}_{\cos\alpha,C} + Y^{180}_{\cos\alpha,C}}{Y^0_C + Y^{180}_C} I^{\odot} + \Big(\frac{Y^0_C \bar{\Lambda}^0 + Y^{180}_C \bar{\Lambda}^{180}}{2(Y^0_C + Y^{180}_C)} + \\ + \frac{Y^0_{\cos 2\alpha,C} \bar{\Lambda}^0 + Y^{180}_{\cos 2\alpha,C} \bar{\Lambda}^{180}}{2(Y^0_C + Y^{180}_C)} \Big) P_x^{\odot} + \frac{Y^0_{\sin 2\alpha,C} \bar{\Lambda}^0 + Y^{180}_{\sin 2\alpha,C} \bar{\Lambda}^{180}}{2(Y^0_C + Y^{180}_C)} P_y^{\odot}. \tag{5.91}$$

Factorizing $(a_0^0 + a_0^{180})$ from Eq. (5.21) Y_0 yields:

$$(a_0^0 + a_0^{180}) Y_0 = \frac{Y^0 + Y^{180}}{1 + P_x \Big(\frac{a_1^0 \bar{\Lambda}^0 - a_1^{180} \bar{\Lambda}^{180}}{a_0^0 + a_0^{180}} \Big) + P_y \Big(\frac{b_1^0 \bar{\Lambda}^0 - b_1^{180} \bar{\Lambda}^{180}}{a_0^0 + a_0^{180}} \Big)}. \tag{5.92}$$

Replacing c_3 and c_6 into the above Y_0 one gets:

$$(a_0^0 + a_0^{180}) Y_0 = \frac{Y^0 + Y^{180}}{1 + c_3 P_x + c_6 P_y}. \tag{5.93}$$

Substituting Eq. (5.93) and $c1$ to $c7$ into Eq. (5.89), Eq. (5.90) and Eq. (5.91) one gets:

$$\frac{Y^{+} - Y^{-}}{\delta_{\odot} (Y^0 + Y^{180})} (1 + c_3 P_x + c_6 P_y) = I^{\odot} + c_3 P_x^{\odot} + c_2 P_y^{\odot}, \tag{5.94}$$

$$\frac{Y^{+}_{\sin\alpha} - Y^{-}_{\sin\alpha}}{\delta_{\odot} (Y^0 + Y^{180})} (1 + c_3 P_x + c_6 P_y) = c_1 I^{\odot} + c_2 P_x^{\odot} + (c_4 - c_5) P_y^{\odot}, \text{and} \tag{5.95}$$

$$\frac{Y^{+}_{\cos\alpha} - Y^{-}_{\cos\alpha}}{\delta_{\odot} (Y^0 + Y^{180})} (1 + c_3 P_x + c_6 P_y) = c_7 I^{\odot} + (c_4 + c_5) P_x^{\odot} + c_2 P_y^{\odot}. \tag{5.96}$$

Looking at Eq. (5.95) and (5.96) one can see that the c_4 terms dominate where the other terms are much smaller corrections, and when excluding the smaller terms, one can obtain the simplified expression of each individual helicity depedent observable. To verify the contribution of the correction terms to the observable value one can solve the system of equations Eq. (5.94), (5.95), (5.96) in order to get the corrected observables but these corrections factors from carbon and polyethylene would increase significantly the statistical uncertainties of the observables, which become larger than the systematic uncertainties.

The path chosen in this analysis, was to derive the expressions for the helicity-dependent observables $I^{\odot}$, $P_x^{\odot}$ and $P_y^{\odot}$, while assuming the same acceptance for

positive, respectively negative target polarization and the following equalities were used $a_0^0 = a_0^{180} = a_0$, $a_1^0 = a_1^{180} = a_1$, $b_1^0 = b_1^{180} = b_1$, $a_2^0 = a_2^{180} = a_2$, $b_2^0 = b_2^{180} = b_2$, and then the Eqs. (5.20) became:

$$Y^{+0} - Y^{-0} = \delta_{\odot} Y_0 \Big(a_0 I^{\odot} + a_1 P_x^{\odot} \bar{\Lambda}^0 + b_1 P_y^{\odot} \bar{\Lambda}^0 \Big) \tag{5.97}$$

$$Y^{+180} - Y^{-180} = \delta_{\odot} Y_0 \Big(a_0 I^{\odot} - a_1 P_x^{\odot} \bar{\Lambda}^{180} - b_1 P_y^{\odot} \bar{\Lambda}^{180} \Big), \tag{5.98}$$

$$Y_{\sin\alpha}^{+0} - Y_{\sin\alpha}^{-0} = \delta_{\odot} Y_0 \Big(b_1 I^{\odot} + \frac{b_2}{2} P_x^{\odot} \bar{\Lambda}^0 + \Big(\frac{a_0}{2} - \frac{a_2}{2} \Big) P_y^{\odot} \bar{\Lambda}^0 \Big), \tag{5.99}$$

$$Y_{\sin\alpha}^{+180} - Y_{\sin\alpha}^{-180} = \delta_{\odot} Y_0 \Big(- b_1 I^{\odot} + \frac{b_2}{2} P_x^{\odot} \bar{\Lambda}^{180} + \Big(\frac{a_0}{2} - \frac{a_2}{2} \Big) P_y^{\odot} \bar{\Lambda}^{180} \Big), \tag{5.100}$$

$$Y_{\cos\alpha}^{+0} - Y_{\cos\alpha}^{-0} = \delta_{\odot} Y_0 \Big(a_1 I^{\odot} + \Big(\frac{a_0}{2} + \frac{a_2}{2} \Big) P_x^{\odot} \bar{\Lambda}^0 + \frac{b_2}{2} P_y^{\odot} \bar{\Lambda}^0 \Big), \tag{5.101}$$

$$Y_{\cos\alpha}^{+180} - Y_{\cos\alpha}^{-180} = \delta_{\odot} Y_0 \Big(- a_1^{\odot} + \Big(\frac{a_0}{2} + \frac{a_2}{2} \Big) P_x^{\odot} \bar{\Lambda}^{180} + \frac{b_2}{2} P_y^{\odot} \bar{\Lambda}^{180} \Big), \tag{5.102}$$

$$Y_{\sin 2\alpha}^{+0} - Y_{\sin 2\alpha}^{-0} = \delta_{\odot} Y_0 \Big(b_2 I^{\odot} + \frac{b_1}{2} P_x^{\odot} \bar{\Lambda}^0 + \frac{a_1}{2} P_y^{\odot} \bar{\Lambda}^0 \Big), \tag{5.103}$$

$$Y_{\sin 2\alpha}^{+180} - Y_{\sin 2\alpha}^{-180} = \delta_{\odot} Y_0 \Big(b_2 I^{\odot} - \frac{b_1}{2} P_x^{\odot} \bar{\Lambda}^{180} - \frac{a_1}{2} P_y^{\odot} \bar{\Lambda}^{180} \Big), \tag{5.104}$$

$$Y_{\cos 2\alpha}^{+0} - Y_{\cos 2\alpha}^{-0} = \delta_{\odot} Y_0 \Big(a_2 I^{\odot} + \frac{a_1}{2} P_x^{\odot} \bar{\Lambda}^0 - \frac{b_1}{2} P_y^{\odot} \bar{\Lambda}^0 \Big), \text{and} \tag{5.105}$$

$$Y_{\cos 2\alpha}^{+180} - Y_{\cos 2\alpha}^{-180} = \delta_{\odot} Y_0 \Big(a_2 I^{\odot} - \frac{a_1}{2} P_x^{\odot} \bar{\Lambda}^{180} + \frac{b_1}{2} P_y^{\odot} \bar{\Lambda}^{180} \Big). \tag{5.106}$$

The first two differences shown in Eq. (5.106) give:

$$\bar{\Lambda}^{180}(Y^{+0} - Y^{-0}) + \bar{\Lambda}^0(Y^{+180} - Y^{-180}) = a_0 \delta_{\odot} Y_0 I^{\odot} (\bar{\Lambda}^0 + \bar{\Lambda}^{180}). \tag{5.107}$$

and replacing a_0 (shown in Eq. (5.60)) and Y_0 (Eq. (5.21)), the expression for the observable $I^{\odot}$ becomes:

$$I^{\odot} = \frac{\bar{\Lambda}^{180}(Y^{+0} - Y^{-0}) + \bar{\Lambda}^0(Y^{+180} - Y^{-180})}{\bar{\delta}_{\odot}(\bar{\Lambda}^{180} Y^0 + \bar{\Lambda}^0 Y^{180})}. \tag{5.108}$$

Similar procedure will be followed to get the $P_x^{\odot}$ observable.

$$Y_{\sin\alpha}^{+0} - Y_{\sin\alpha}^{-0} + Y_{\sin\alpha}^{+180} - Y_{\sin\alpha}^{-180} = \delta_{\odot} Y_0 \Big(\frac{b_2}{2} P_x^{\odot} (\bar{\Lambda}^0 + \bar{\Lambda}^{180}) + \Big(\frac{a_0}{2} - \frac{a_2}{2} \Big) P_y^{\odot} (\bar{\Lambda}^0 + \bar{\Lambda}^{180}) \Big) \tag{5.109}$$

$$Y_{\cos\alpha}^{+0} - Y_{\cos\alpha}^{-0} + Y_{\cos\alpha}^{+180} - Y_{\cos\alpha}^{-180} = \delta_{\odot} Y_0 \Big(\Big(\frac{a_0}{2} + \frac{a_2}{2} \Big) P_x^{\odot} (\bar{\Lambda}^0 + \bar{\Lambda}^{180}) + \frac{b_2}{2} P_y^{\odot} (\bar{\Lambda}^0 + \bar{\Lambda}^{180}) \Big) \tag{5.110}$$

Next step is to solve for $P_x^{\odot}$ observable:

$$\frac{b_2}{2}\Big(Y^{+0}_{\sin\alpha} - Y^{-0}_{\sin\alpha} + Y^{+180}_{\sin\alpha} - Y^{-180}_{\sin\alpha}\Big) - \Big(\frac{a_0}{2} - \frac{a_2}{2}\Big)\Big(Y^{+0}_{\cos\alpha} - Y^{-0}_{\cos\alpha} + Y^{+180}_{\cos\alpha} - Y^{-180}_{\cos\alpha}\Big) = \\ = \delta_{\odot} Y_0 \Big(\frac{b_2^2}{4} - \frac{a_0^2}{4} + \frac{a_2^2}{4}\Big) P_x^{\odot}(\bar{\Lambda}^0 + \bar{\Lambda}^{180}). \tag{5.111}$$

$$P_x^{\odot} = \frac{\frac{b_2}{2}\Big(Y^{+0}_{\sin\alpha} - Y^{-0}_{\sin\alpha} + Y^{+180}_{\sin\alpha} - Y^{-180}_{\sin\alpha}\Big) - \Big(\frac{a_0}{2} - \frac{a_2}{2}\Big)\Big(Y^{+0}_{\cos\alpha} - Y^{-0}_{\cos\alpha} + Y^{+180}_{\cos\alpha} - Y^{-180}_{\cos\alpha}\Big)}{\delta_{\odot} Y_0 \Big(\frac{b_2^2}{4} - \frac{a_0^2}{4} + \frac{a_2^2}{4}\Big)(\bar{\Lambda}^0 + \bar{\Lambda}^{180})} \tag{5.112}$$

Replacing the coefficients a_0, a_2 and b_2 Eq. (5.60), (5.63), (5.64) in the $P_x^{\odot}$ expression leads to:

$$P_x^{\odot} = 2\frac{(\bar{\Lambda}^{180} Y^0_{\sin 2\alpha} + \bar{\Lambda}^0 Y^{180}_{\sin 2\alpha})(Y^{+0}_{\sin\alpha} - Y^{-0}_{\sin\alpha} + Y^{+180}_{\sin\alpha} - Y^{-180}_{\sin\alpha})}{\delta_{\odot}[(\bar{\Lambda}^{180} Y^0_{\sin 2\alpha} + \bar{\Lambda}^0 Y^0_{\sin 2\alpha})^2 - (Y^0\bar{\Lambda}^{180} + Y^{180}\bar{\Lambda}^0)^2 + (Y^0_{\cos 2\alpha}\bar{\Lambda}^{180} + Y^{180}_{\cos 2\alpha}\bar{\Lambda}^0)^2]} \\ -2\frac{[(Y^0\bar{\Lambda}^{180} + Y^{180}\bar{\Lambda}^0) - (Y^0_{\cos 2\alpha}\bar{\Lambda}^{180} + Y^{180}_{\cos 2\alpha}\bar{\Lambda}^0)](Y^{+0}_{\cos\alpha} - Y^{-0}_{\cos\alpha} + Y^{+180}_{\cos\alpha} - Y^{-180}_{\cos\alpha})}{\delta_{\odot}[(\bar{\Lambda}^{180} Y^0_{\sin 2\alpha} + \bar{\Lambda}^0 Y^{180}_{\sin 2\alpha})^2 - (Y^0\bar{\Lambda}^{180} + Y^{180}\bar{\Lambda}^0)^2 + (Y^0_{\cos 2\alpha}\bar{\Lambda}^{180} + Y^{180}_{\cos 2\alpha}\bar{\Lambda}^0)^2]}. \tag{5.113}$$

Similarly for $P_y^{\odot}$ one could get:

$$P_y^{\odot} = 2\frac{[(Y^0\bar{\Lambda}^{180} + Y^{180}\bar{\Lambda}^0) + (Y^0_{\cos 2\alpha}\bar{\Lambda}^{180} + Y^{180}_{\cos 2\alpha}\bar{\Lambda}^0)](Y^{+0}_{\sin\alpha} - Y^{-0}_{\sin\alpha} + Y^{+180}_{\sin\alpha} - Y^{-180}_{\sin\alpha})}{\delta_{\odot}[(Y^0\bar{\Lambda}^{180} + Y^{180}\bar{\Lambda}^0)^2 - (\bar{\Lambda}^{180} Y^0_{\sin 2\alpha} + \bar{\Lambda}^0 Y^0_{\sin 2\alpha})^2 - (Y^0_{\cos 2\alpha}\bar{\Lambda}^{180} + Y^{180}_{\cos 2\alpha}\bar{\Lambda}^0)^2]} \\ -2\frac{(\bar{\Lambda}^{180} Y^0_{\sin 2\alpha} + \bar{\Lambda}^0 Y^{180}_{\sin 2\alpha})(Y^{+0}_{\cos\alpha} - Y^{-0}_{\cos\alpha} + Y^{+180}_{\cos\alpha} - Y^{-180}_{\cos\alpha})}{\delta_{\odot}[(Y^0\bar{\Lambda}^{180} + Y^{180}\bar{\Lambda}^0)^2 - (\bar{\Lambda}^{180} Y^0_{\sin 2\alpha} + \bar{\Lambda}^0 Y^{180}_{\sin 2\alpha})^2 - (Y^0_{\cos 2\alpha}\bar{\Lambda}^{180} + Y^{180}_{\cos 2\alpha}\bar{\Lambda}^0)^2]}. \tag{5.114}$$

These final expressions of the polarization observables include different moments terms correcting for the instrumental asymmetries and they were used in the extraction of the observables of this analysis. A study (Fig. 5.4) showed that when extracting the helicity-dependent observables for different combinations of run groups and topologies one can observe that the acceptance effects cancelled out for the helicity-dependent observables.

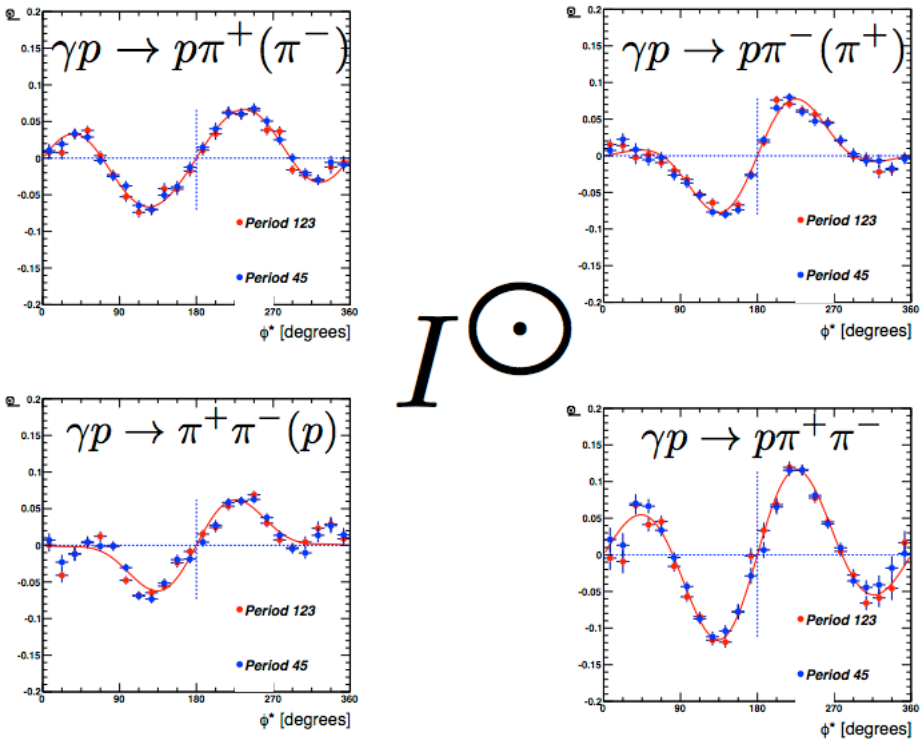

Figure 5.4: The observable $I^{\odot}$ extracted for each individual topology, where "Period 123" represents run groups 1, 2, and 3 and "Period 45" represents the run groups 4 and 5.

5.3 Sources of Systematic Uncertainties

Equation (5.115) was used to determine the contributions to the systematic uncertainties.

$$\sigma_O = \sqrt{\frac{\sum_{i=1}^{N} \frac{[O_i^{nom} - O_i^{alt}]^2}{(\sigma_i^{nom})^2}}{\sum_{i=1}^{N} \frac{1}{(\sigma_i^{nom})^2}}} \tag{5.115}$$

where O_i^{nom} is the nominal value of the observable in i-th bin, O_i^{alt} is the altered observable in the i-th bin, σ_i^{nom} is the uncertainty of the nominal value of observable in the i-th bin and N is the total number of bins. The first three systematic uncertainties shown in Table 5.1 pertain to the whole experiment and the other contributions are specific to this analysis.

∗ **Beam charge asymmetry** The systematic uncertainty due to the beam charge

Table 5.1: Systematic uncertainties.

Source	$I^{\odot}$	P_x	P_y	$P_x^{\odot}$	$P_y^{\odot}$
Beam charge asymmetry	0.01%	0.0%	0.0%	0.01%	0.01%
Photon beam polarization	3.0%	0.0%	0.0%	3.0%	3.0%
Target polarization	0.0%	$< 3.5\%$	$< 3.5\%$	$< 3.5\%$	$< 3.5\%$
Acceptance change	0.0	< 0.01	< 0.01	0.0	0.0
Background subtraction method	0.001	0.001	0.002	0.003	0.002
Target polarization angle offset	0.0	< 0.001	< 0.001	< 0.001	< 0.001
Particle ID	0.01	0.01	0.01	0.02	0.02
TOTAL (absolute)	0.01	0.01	0.01	0.02	0.02
TOTAL (%)	3.0%	3.5%	3.5%	4.6%	4.6%

asymmetry was determined to be less than 0.01% [31] (see Section 2.2)

* **Photon beam polarization** The second contribution was due to the degree of the beam polarization and will affect the observables $I^{\odot}$, $P_x^{\odot}$, $P_y^{\odot}$ which include the degree of the beam polarization $\delta_{\odot}$ in the denominator (Eqs. (5.108), (5.113), and (5.114)). The contribution to the systematic uncertainty due to measuring the degree of photon beam polarization degree $\delta_{\odot}$ (Eq. (2.2)) was determined to be 3% [31]. The polarization observables P_x, P_y are not affected by the uncertainty in measuring $\delta_{\odot}$ because these observables arise due to the target polarization only.

* **Target polarization** The third contribution to the systematic uncertainty is due to measuring the degree of the target polarization which will affect the observables P_x, P_y, $P_x^{\odot}$ and $P_y^{\odot}$ since their equations (Eqs. (4.10), (4.11), (4.12), (4.13)) include the target polarization in their expressions. For the observable $I^{\odot}$ there is no contribution to the systematic uncertainty due to the target polarization measurement since it does not include the target polarization in its expression. The systematic uncertainty due to the measurement of the target

polarization Λ is 1.7% [45] and when the butanol target was replaced with a polarized deuterated propanediol target the systematic uncertainty in measuring the target polarization Λ was found to be $\approx 3\%$ [46]. So for the target polarization measurement the overall systematic uncertainty is $< 3.5\%$.

* **Acceptance correction** Because of the changing acceptance from run group to run group, correction factors to the observable extraction were obtained (Section 5.1 and Section 5.2) and were used to estimate the systematic uncertainties due to the changing acceptance as shown in Table 5.1.

* **Background subtraction** The probabilistic weighting method employed in determining the Q-values for each event, gives Q-values between 0 and 1, and a study determined the contribution to the systematic uncertainties if events with $Q < 0.05$, $Q < 0.10$ and $Q < 0.15$ were excluded from the observables extraction. These excluded events are most likely background events, since their Q is close to zero. The uncertainties are shown in Table 5.1. A more direct test of the uncertainties of the Q values, e.g., with repeated fits using various fit functions, would possibly result in a higher uncertainty estimate.

* **Target polarization angle offset** As shown in Section 6.1 the target offset angle was determined to be $116.3^\circ \pm 1.4^\circ$ for the positive target polarization and $296.3^\circ \pm 1.4^\circ$ for the negative target polarization and since the polarization observables P_x, P_y, $P_x^\odot$ and $P_x^\odot$ enter the expression of the polarized cross-section (Eq. (5.1)) via a $\sin\alpha$ or $\cos\alpha$ term and then the contribution to systematic uncertainty due to $\delta\alpha = 1.4^\circ$ is derived as shown:

$$\sin(\alpha + \delta\alpha) = \sin\alpha\cos\delta\alpha + \cos\alpha\sin\delta\alpha \tag{5.116}$$

$$\cos(\alpha + \delta\alpha) = \cos\alpha\cos\delta\alpha - \sin\alpha\sin\delta\alpha \tag{5.117}$$

where $\cos\delta\alpha > 0.999$ and that means a negligible contribution of $\delta\alpha$ to the systematic uncertainty of the observables P_x, P_y, $P_x^{\odot}$ and $P_x^{\odot}$ as shown in Table 5.1.

* **Particle identification** For the particle ID the $\Delta\beta$ cuts were varied from 3σ to 2σ range (Section 3.3) and the results are shown in Table 5.1. These results are dominated by statistical uncertainties and likely overestimated.

Chapter 6

The Results

6.1 Kinematics

Before discussing the results of the analysis, one should be familiar with the kinematics of this reaction and the variables specific to this reaction channel are: the center-of-mass energy W, the angle $\phi*$, the angle θ_{CM}, the angle $\theta*$ (Fig. 6.1), the invariant mass squared $m^2_{\pi^+\pi^-}$ and the invariant mass $m_{p\pi^+}$. The coordinates and angles are defined as:

$$\vec{q} = \vec{p}_{\pi^+} + \vec{p}_{\pi^-}, \tag{6.1}$$

$$\hat{y'} = \hat{k} \times \hat{q}, \tag{6.2}$$

$$\cos\theta^* = \hat{p}_{\pi^+} \cdot \hat{z'}, \tag{6.3}$$

$$\cos\phi^* = \frac{\hat{y'} \cdot (\hat{z'} \times \hat{p}_{\pi^+})}{|\hat{z'} \times \hat{p}_{\pi^+}|}, \tag{6.4}$$

$$\sin\phi^* = -\frac{\hat{x} \cdot (\hat{z'} \times \hat{p}_{\pi^+})}{|\hat{z'} \times \hat{p}_{\pi^+}|}, and \tag{6.5}$$

$$\cos\theta_{CM} = \hat{k} \cdot \hat{q}. \tag{6.6}$$

Another angle to be defined is the target polarization angle α (Fig. 6.2).

6.2 The Observables' Distributions For Different Kinematic Bins

After the event selection, the Eloss and momentum corrections, and after presenting the method for the extraction of the observables, and estimating the systematic uncertainties associated with this experiment, the results are presented and discussed

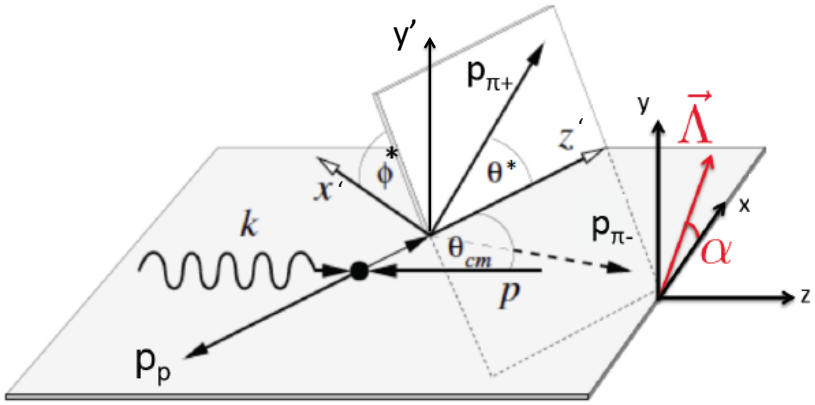

Figure 6.1: Reaction plane in the center of mass (CM) (modified figure from [21]), where k and p are the momenta of the photon and of the incident proton in the center of mass frame, and p_p, p_{π^+} and p_{π^-} are the momenta of recoiling proton, π^+ and π^- in the center of mass frame. The x, y and z are the coordinates in the reaction frame.

in this section. The analysis extracted the observables $I^{\odot}$, P_x, P_y, $P_x^{\odot}$ and $P_x^{\odot}$ for 11 kinematic bins in center of mass energy W ranging from 1450 MeV to 2550 MeV for 24 bins in ϕ^* ranging from 0° to 360°. Also the results include observables binned in $\cos\Theta_{CM}$, respectively $\cos\Theta^*$ ranging from -1 to $+1$. Each observable is characterized by an odd or even behaviour due to the parity conservation and thus an even or odd Fourier function was fitted to the results to check the symmetry of the observables. The expressions of the odd and even fit functions F_{odd} and F_{even} are shown by Eq. (6.7) and Eq. (6.8).

$$F_{odd} = b_1 \sin(\Phi^*) + b_2 \sin(2\Phi^*) + b_3 \sin(3\Phi^*) + b_4 \sin(4\Phi^*) + b_5 \sin(5\Phi^*) \tag{6.7}$$

$$F_{even} = a_0 + a_1 \cos(\Phi^*) + a_2 \cos(2\Phi^*) + a_3 \cos(3\Phi^*) + a_4 \cos(4\Phi^*) + a_5 \cos(5\Phi^*) \tag{6.8}$$

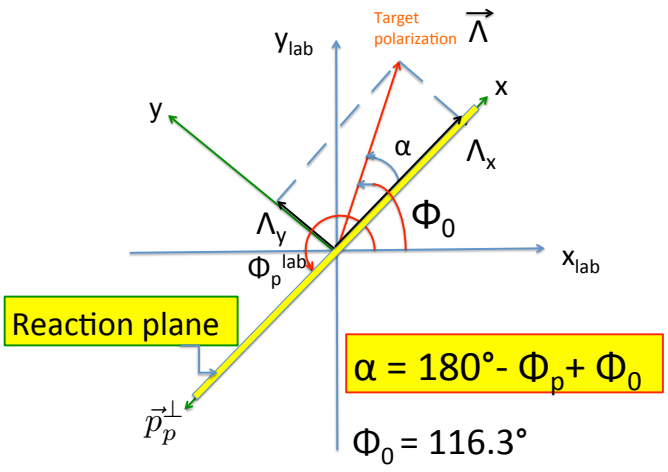

Figure 6.2: Target polarization direction, where: angle α is the target polarization angle, $\vec{p}_p^{\perp}$ is the perpendicular component of the recoiling proton momentum, ϕ_p^{lab} is the angle that the recoiling proton makes with x_{lab}, $\vec{\Lambda}$ the target polarization vector and Λ_x, Λ_y are the x, y projections of the target polarization vector $\vec{\Lambda}$ on x and y axis, and ϕ_0 is the target polarization offset. ϕ_0 can have two possible values: for the positive orientation the value is 116.3° from x_{lab} and for the negative orientation the value is 296.3° from x_{lab}.

First are shown the observables after integrating over all kinematic variables as in Fig. 6.3, 6.4, 6.5, 6.6. When integrating over all kinematic variables except W, the observables are shown in Fig. 6.7, 6.8, 6.9, 6.10, 6.11.

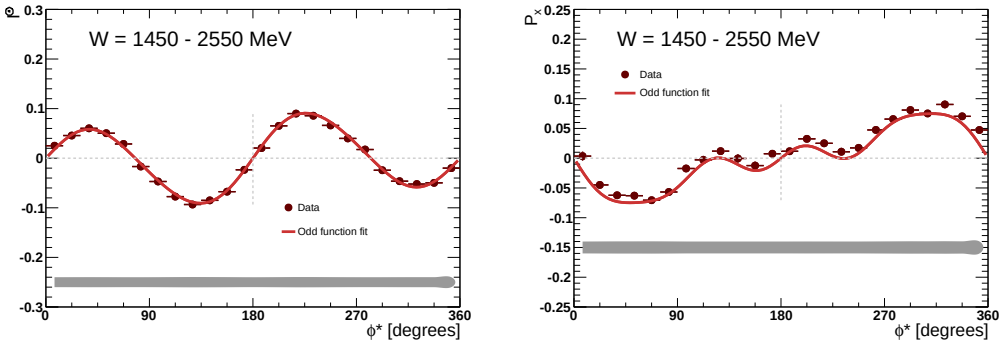

Figure 6.3: Angular distribution of the observable $I^{\odot}$ (left) and P_x (right) integrated over all kinematic variables, where the lower gray bands represent the systematic uncertainties.

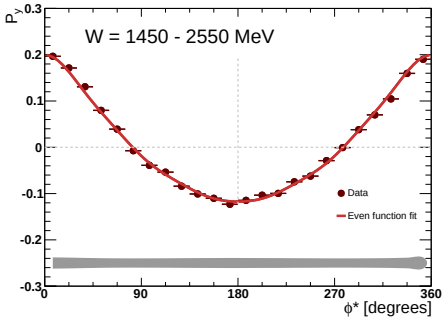

Figure 6.4: Angular distribution of observable P_y integrated over all kinematic variables, where the lower gray band represents the systematic uncertainties.

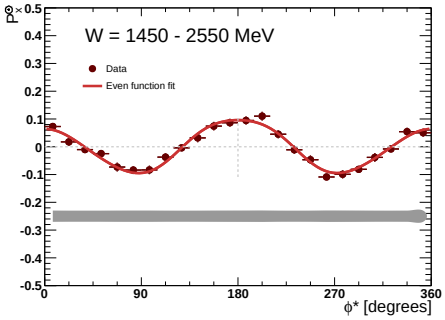

Figure 6.5: Angular distribution of the observable $P_x^{\odot}$ integrated over all kinematic variables, where the lower gray band represents the systematic uncertainties.

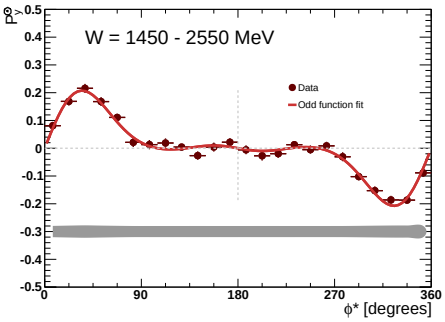

Figure 6.6: Angular distribution of observable $P_y^{\odot}$ integrated over all kinematic variables, where the lower gray band represents the systematic uncertainties.

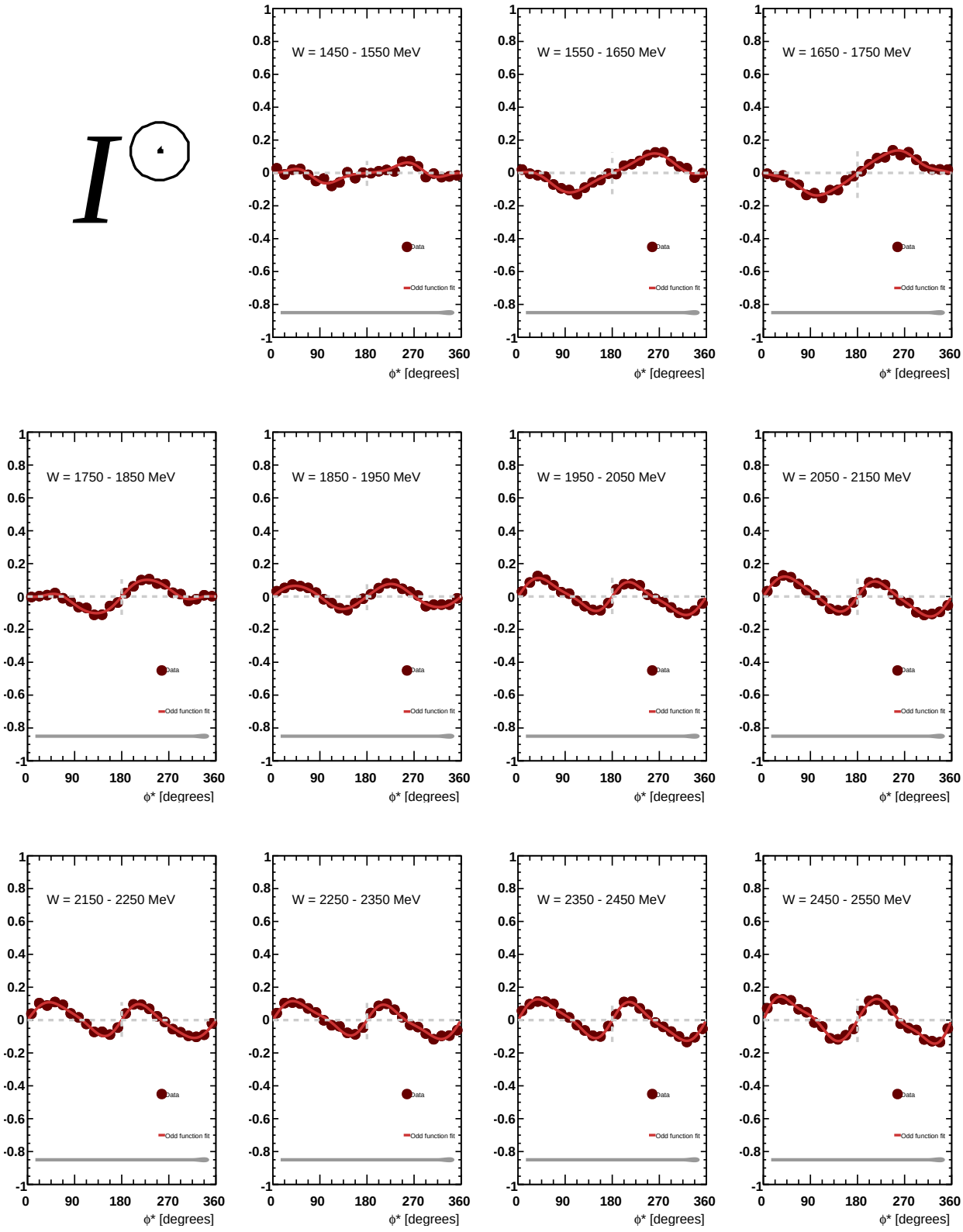

Figure 6.7: Angular distribution of observable $I^{\odot}$ for 11 bins in W, where the dark red markers represent the data, the red curve represents the odd fit reflecting the expected symmetry of this observable, and the lower gray bands represent the systematic uncertainties.

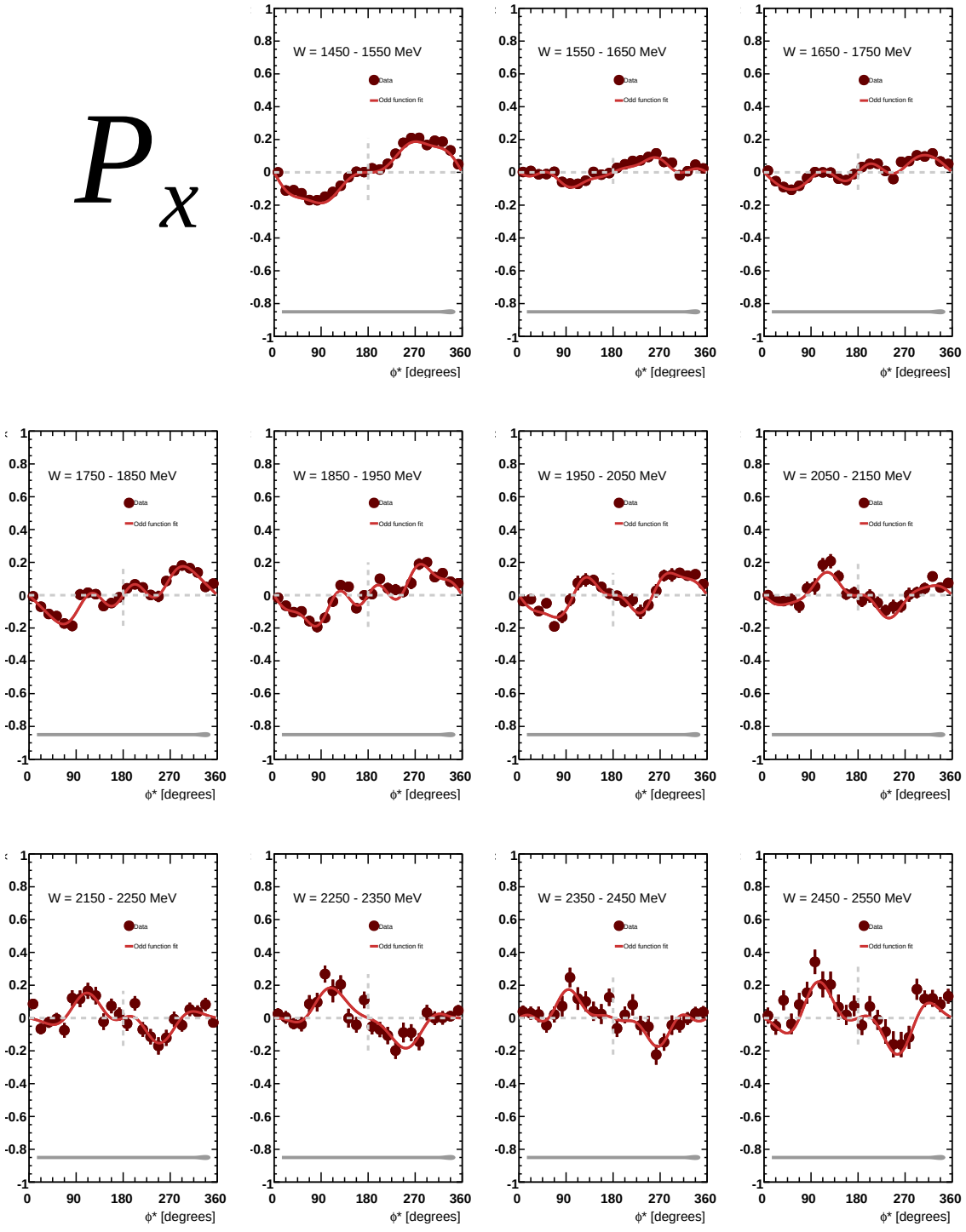

Figure 6.8: Angular distribution of observable P_x for 11 bins in W, where the dark red markers represent the data, the red curve represents the odd fit reflecting the expected symmetry of this observable, and the lower gray bands represent the systematic uncertainties.

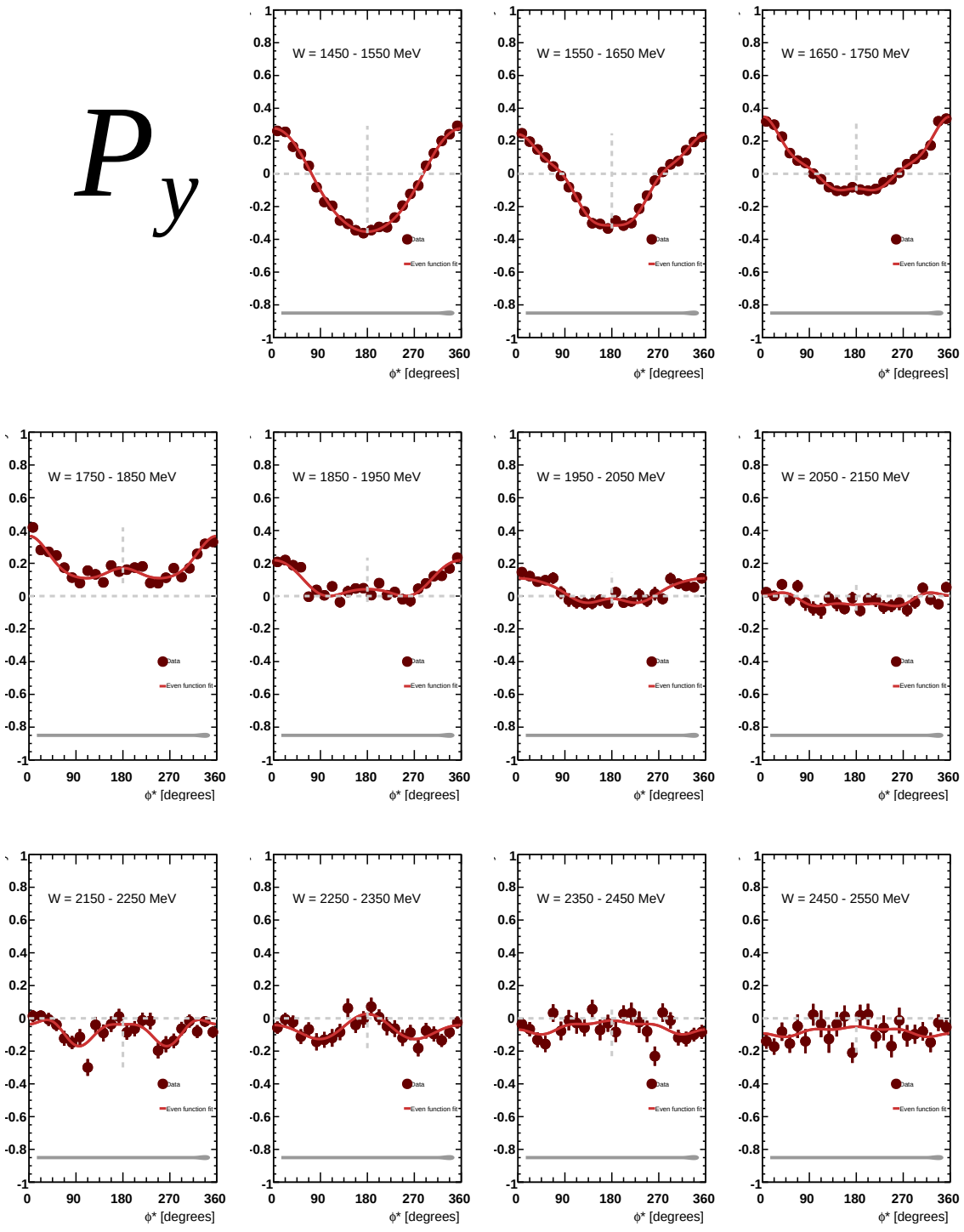

Figure 6.9: Angular distribution of observable P_y for 11 bins in W, where dark red markers represent the data, the red curve represents the even fit reflecting the expected symmetry of this observable, and the lower gray bands represent the systematic uncertainties.

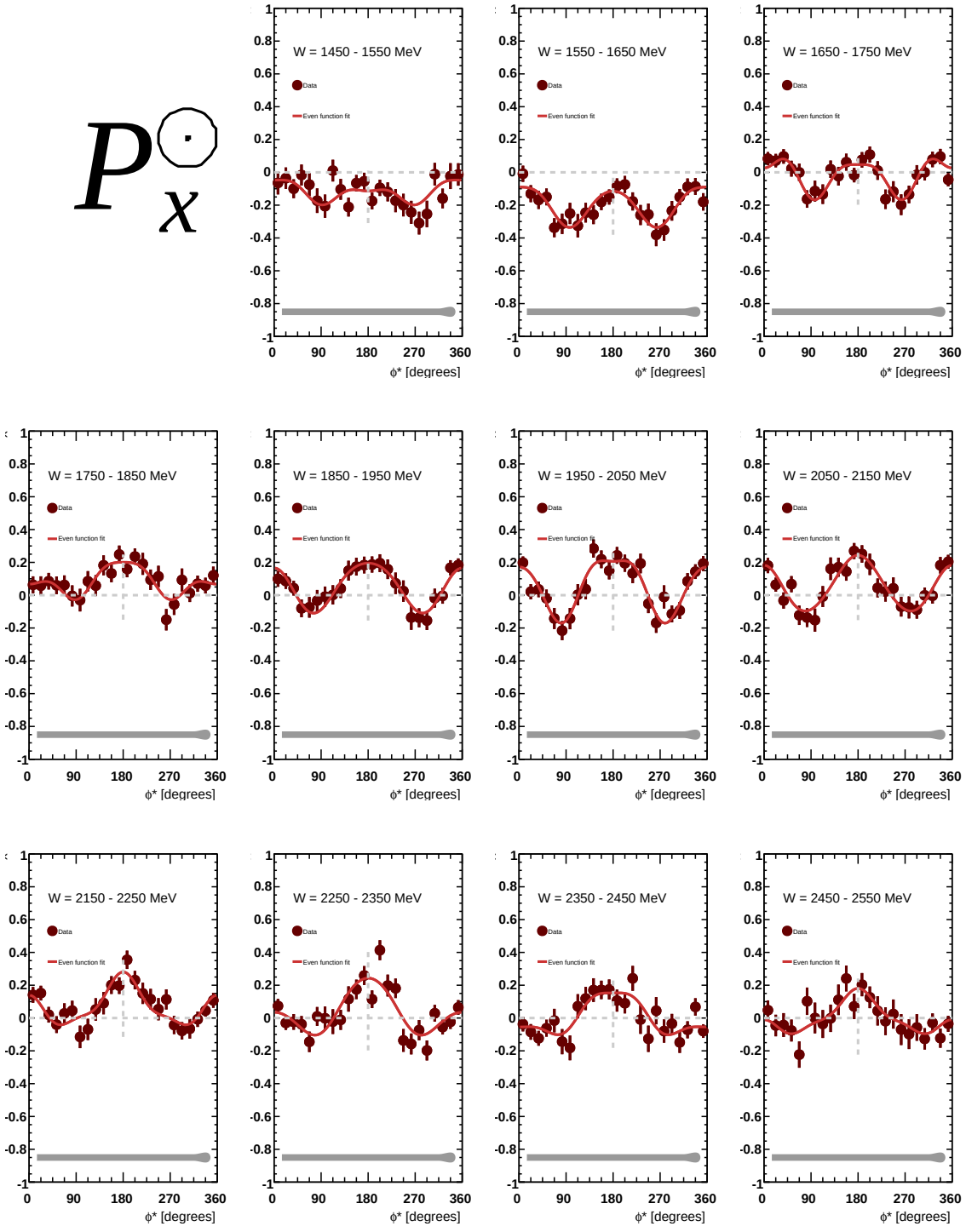

Figure 6.10: Angular distribution of observable $P_x^{\odot}$ for 11 bins in W, where dark red markers represent the data, the red curve represents the even fit reflecting the expected symmetry of this observable, and the lower gray bands represent the systematic uncertainties.

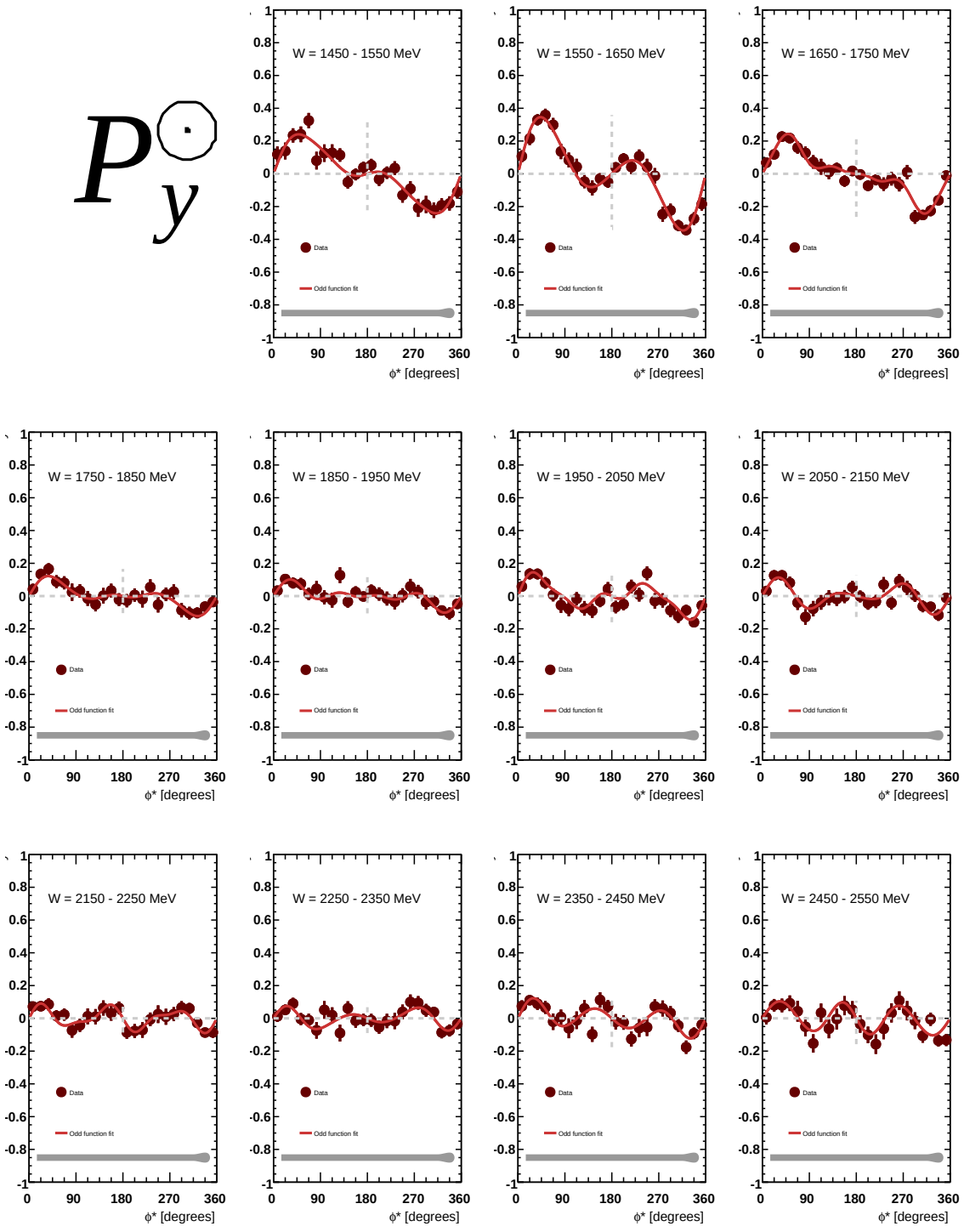

Figure 6.11: Angular distribution of observable $P_y^{\odot}$ for 11 bins in W, where dark red markers represent the data, the red curve represents the odd fit reflecting the expected symmetry of this observable, and the lower gray bands represent the systematic uncertainties.

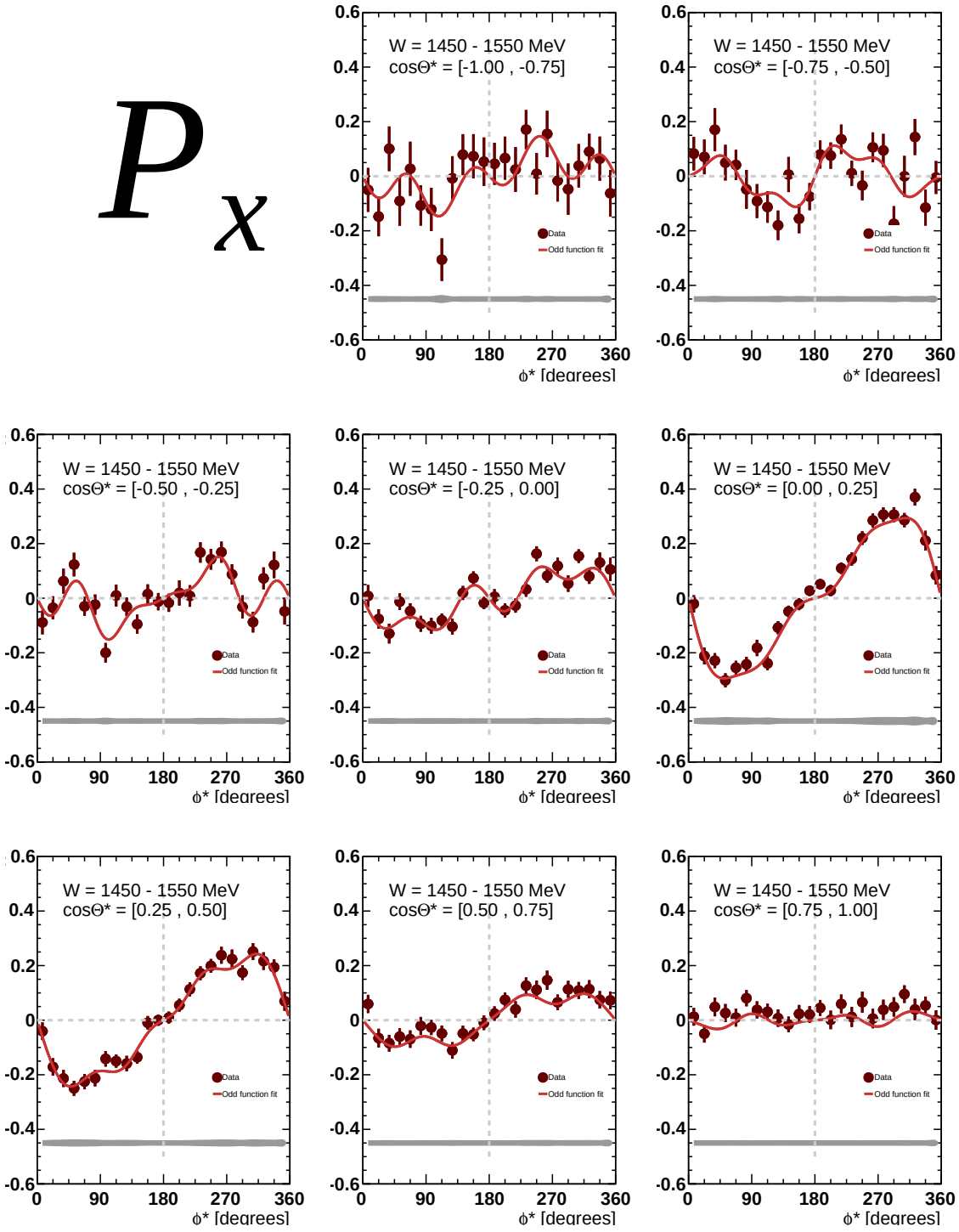

Figure 6.12: Angular distribution of observable P_x for $W = 1450$ MeV and 8 bins in $\cos\Theta^*$, where dark red markers represent the data, the red curve represents the odd fit reflecting the expected symmetry of this observable, and the lower gray bands represent the systematic uncertainties.

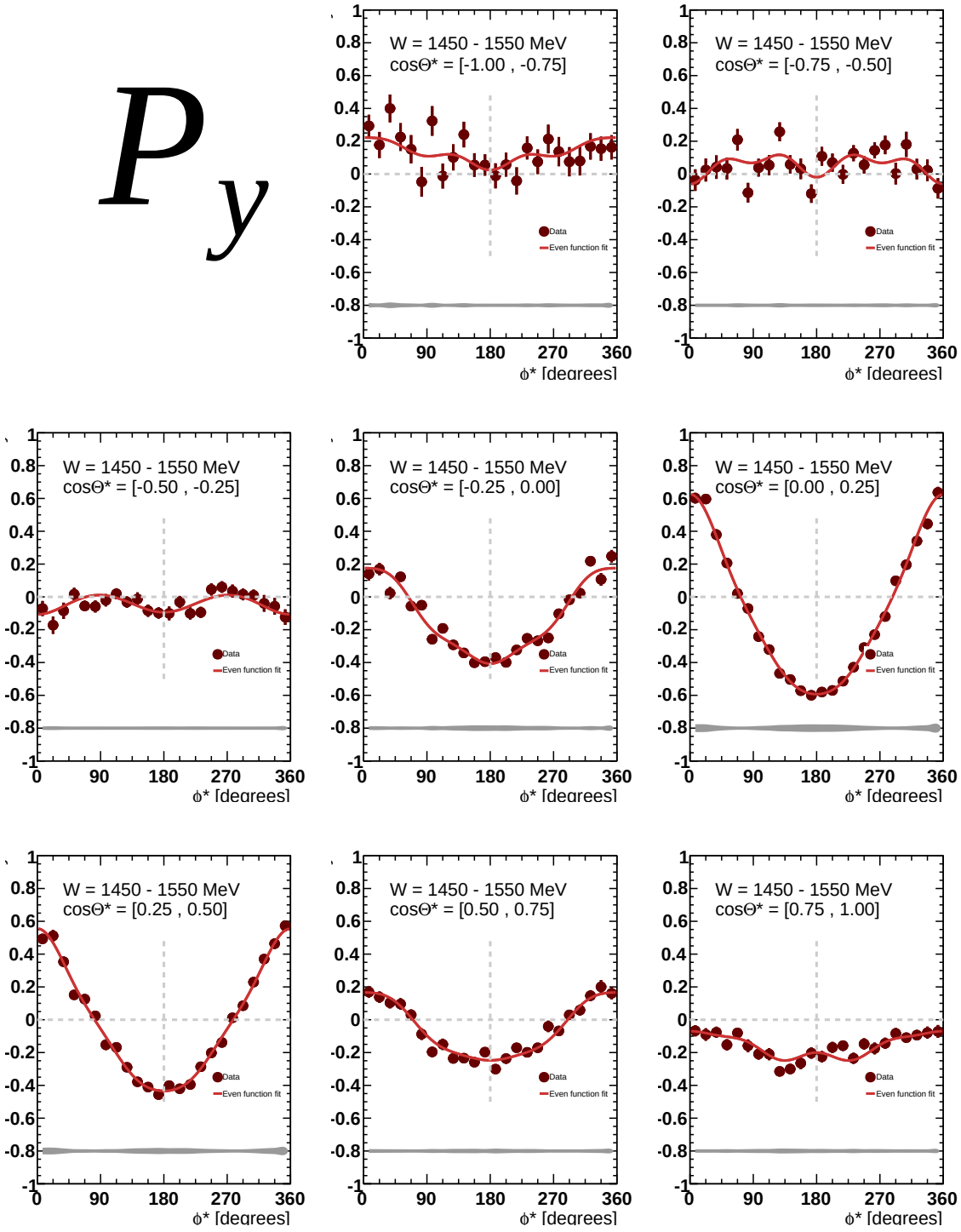

Figure 6.13: Angular distribution of observable P_y for $W = 1450$ MeV and 8 bins in $\cos\Theta^*$, where dark red markers represent the data, the red curve represents the even fit reflecting the expected symmetry of this observable, and the lower gray bands represent the systematic uncertainties.

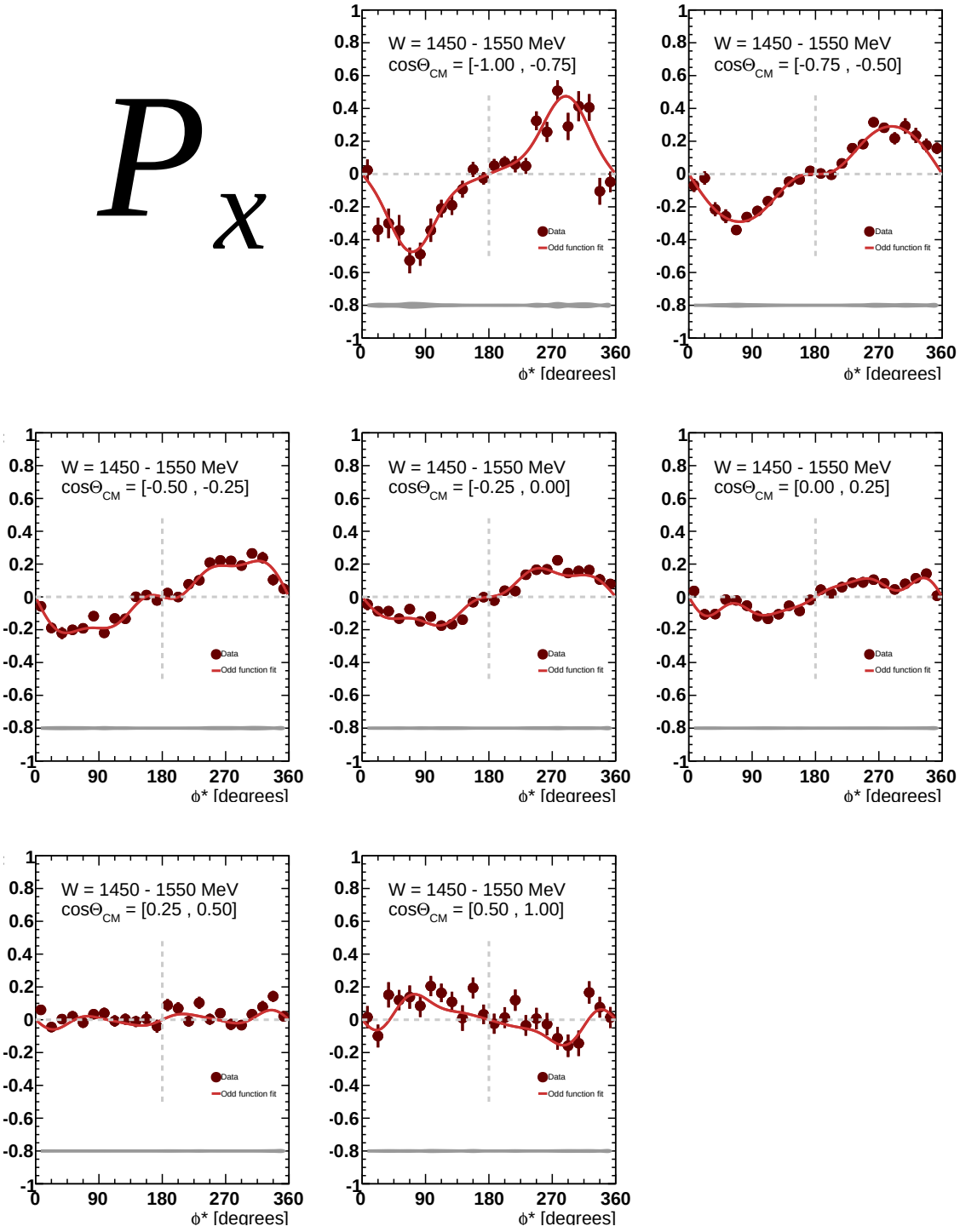

Figure 6.14: Angular distribution of observable P_x for $W = 1450$ MeV and 7 bins in $\cos\Theta_{CM}$, where dark red markers represent the data, the red curve represents the odd fit reflecting the expected symmetry of this observable, and the lower gray bands represent the systematic uncertainties.

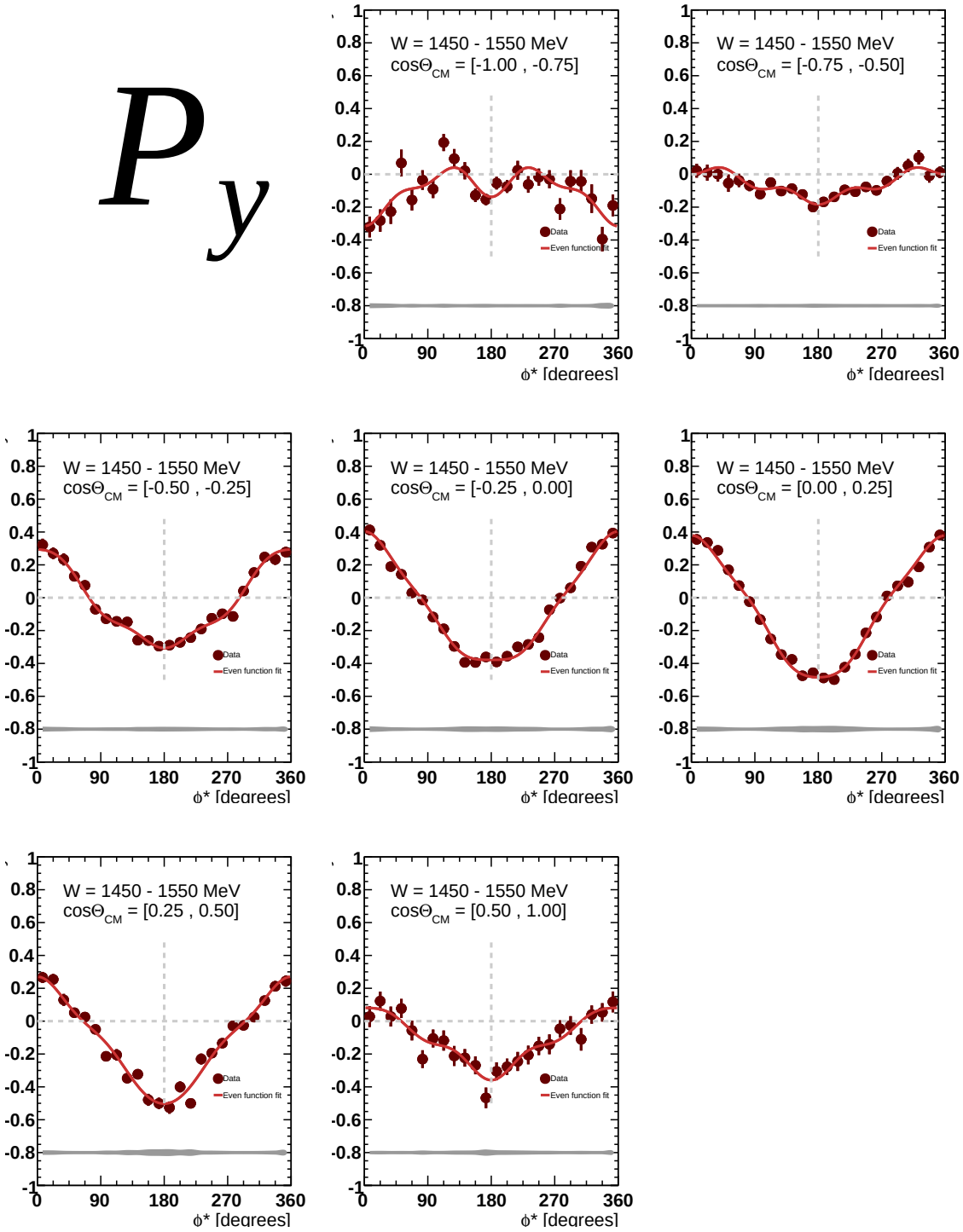

Figure 6.15: Angular distribution of the observable P_y for $W = 1450$ MeV and 7 bins in $\cos\Theta_{CM}$, where dark red markers represent the data, the red curve represents the odd fit reflecting the expected symmetry of this observable, and the lower gray bands represent the systematic uncertainties.

6.3 Comparison With g1c Results

An analysis check consists of comparing the results of this analysis with the published results, which exist only for the $I^{\odot}$ observable, and the comparison is shown in Fig. 6.17. The first published results for the observable $I^{\odot}$ [21] come from the g1c experiment of double-pion photoproduction from unpolarized hydrogen with circularly-polarized photons in the energy range between 0.5 GeV and 2.3 GeV. The g1c experiment used an unpolarized target (pure hydrogen target) providing only unpolarized nucleons coming from a hydrogen target, but g9b experiment used a polarized butanol target which includes free protons and bound nucleons from carbon and oxygen. A non-zero helicity asymmetry is possible for both, the double-pion photoproduction off free and bound protons. Figure 6.16 shows $I^{\odot}$ extracted from the carbon-target data.

Therefore, the observable $I^{\odot}$ extracted from the g9b butanol data includes asymmetry contributions from free and bound protons. The comparison of the g9b data with the data from g1c in Fig. 6.17 shows good agreement, indicating that the helicity asymmetry off bound protons is similar to that off free protons.

6.4 Observables' Comparison To The Model Calculation

As explained before, the excited states of the baryons cannot be completely described by pQCD and theoretical models are used to predict observables, which in turn will assist in the identification of baryons resonances. Two examples (Fig. 6.18 and 6.19) were chosen to show a preliminary comparison between the observables and the results from the reaction model by A. Fix and H. Arenhövel [11]. The comparison shows rather a lack of agreement between the data and model. The constraints from the present data may help to improve the model description.

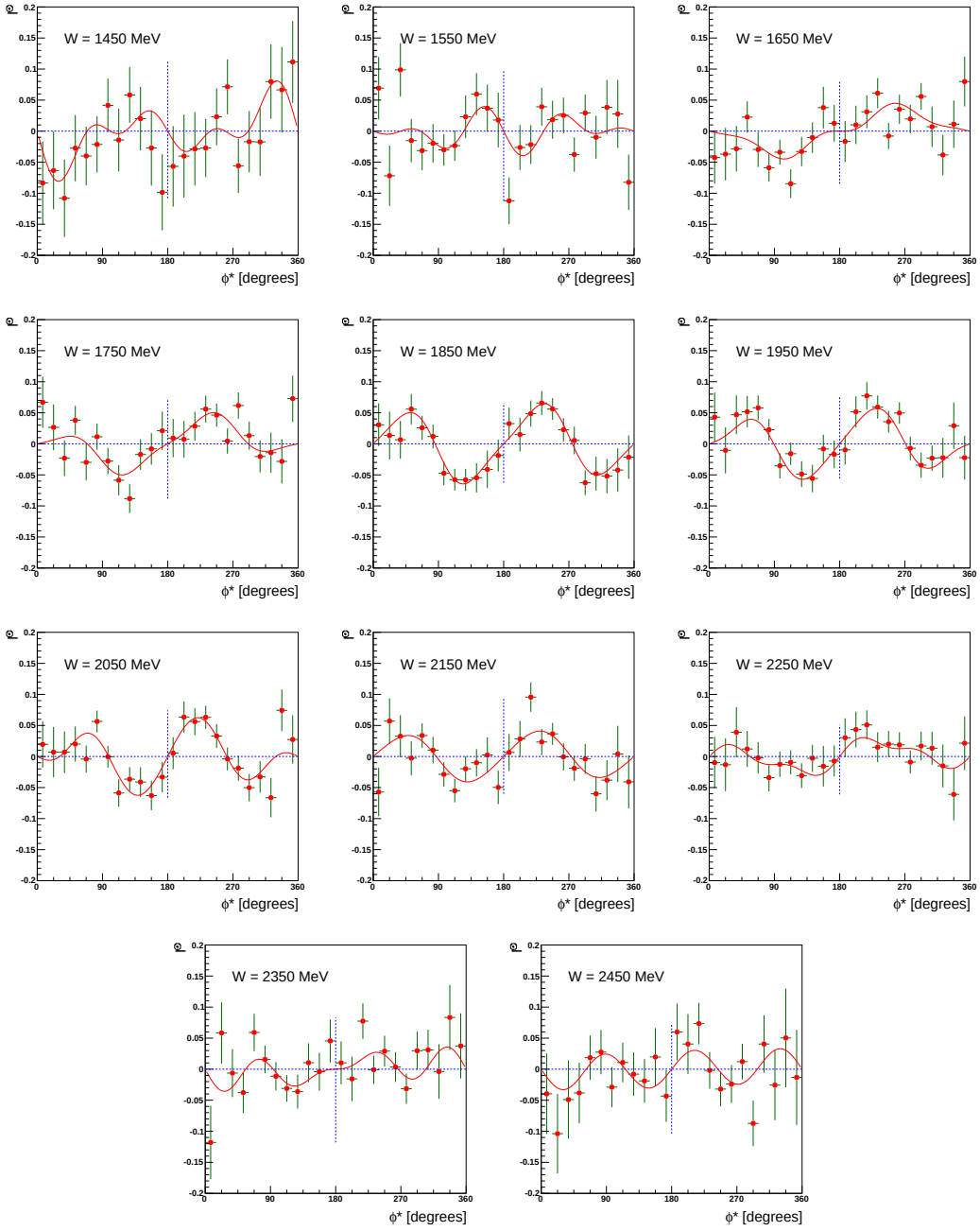

Figure 6.16: Observable $I^{\odot}$ for double-pion photoproduction off ^{12}C for eleven bins in W.

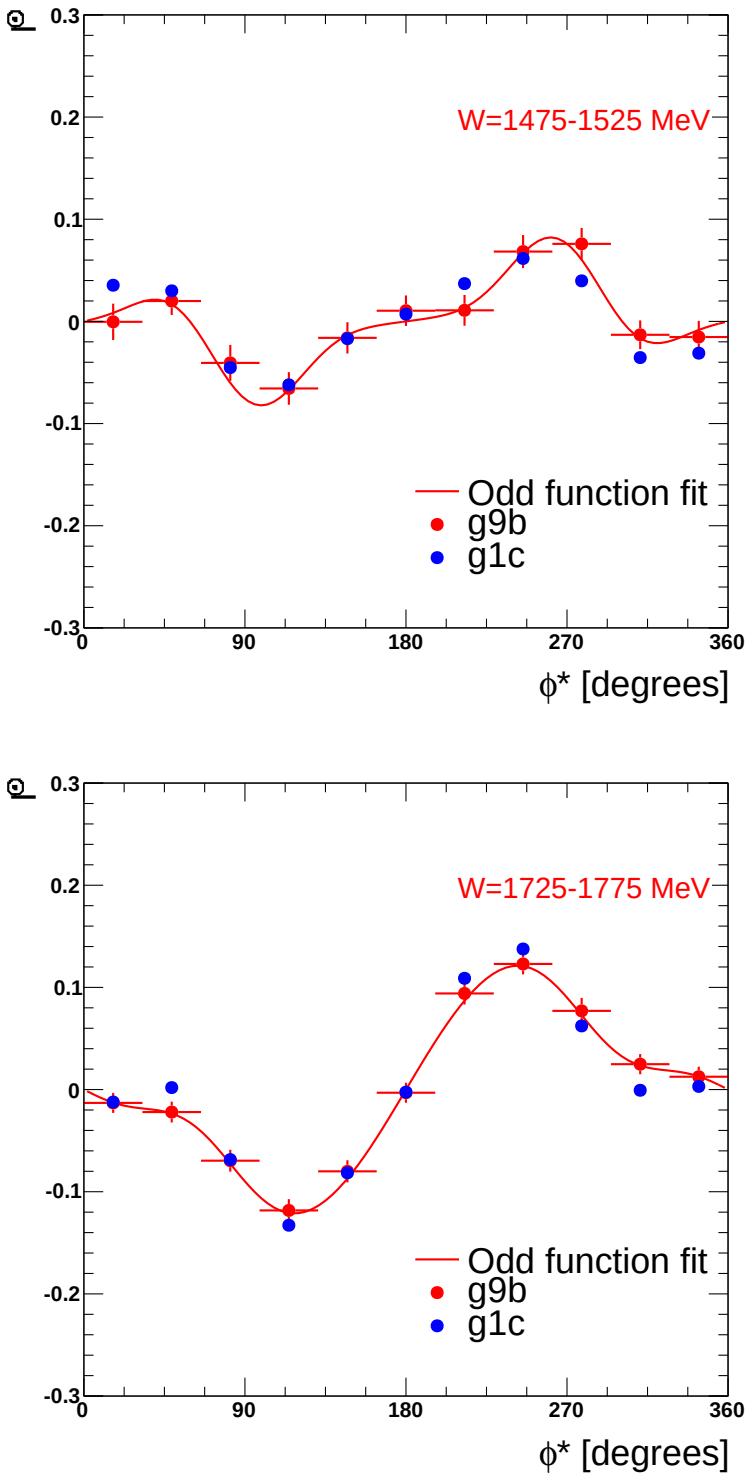

Figure 6.17: Comparison of the observable $I^{\odot}$ from g1c and g9b experiment for $W = 1475 - 1525$ MeV (top) and $W = 1725 - 1725$ MeV (bottom).

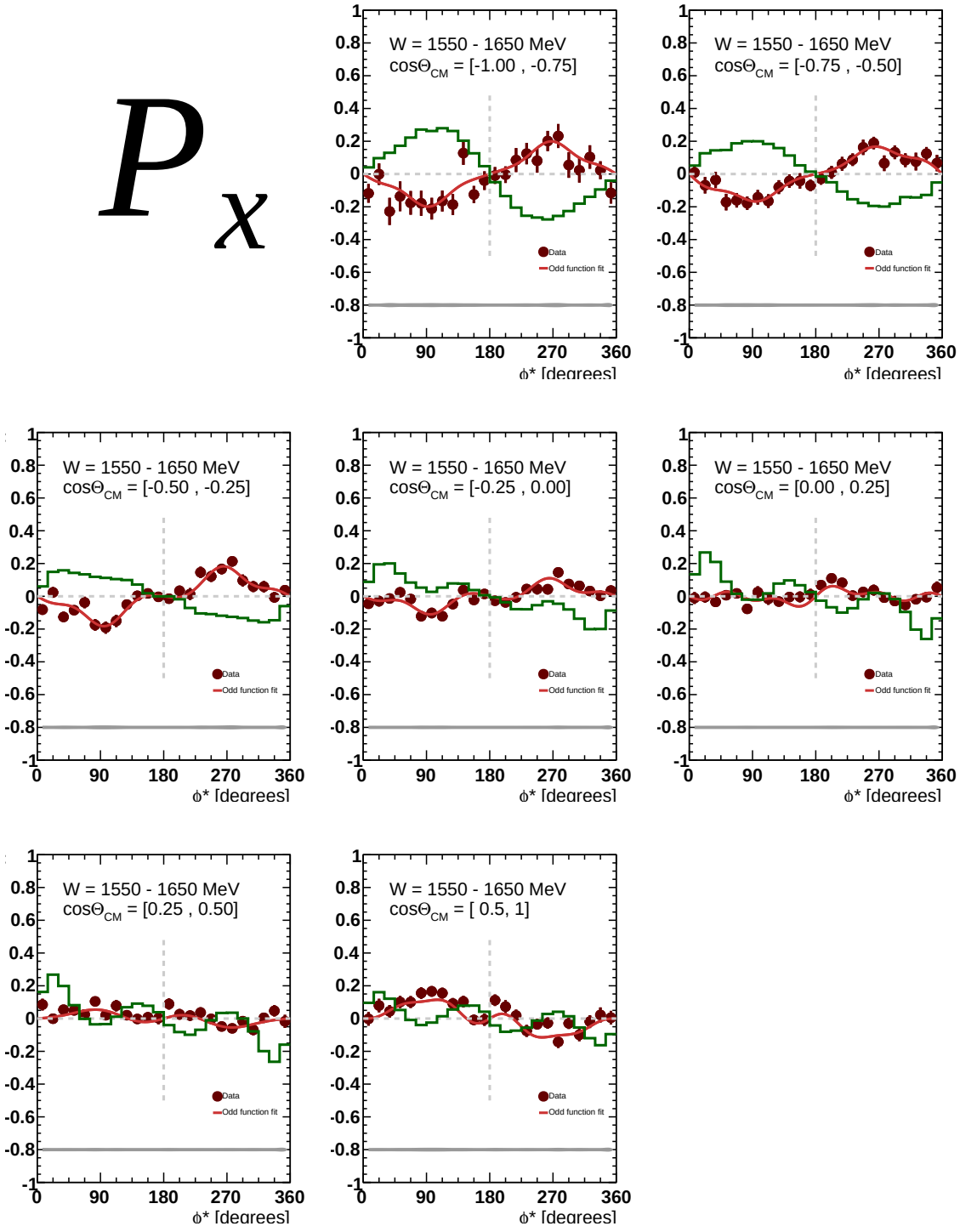

Figure 6.18: Comparison of P_x for $W = 1550 - 1650$ MeV and 7 bins in $\cos_{CM}$ with the model calculation (green curve). The lower gray bands represent the systematic uncertainties.

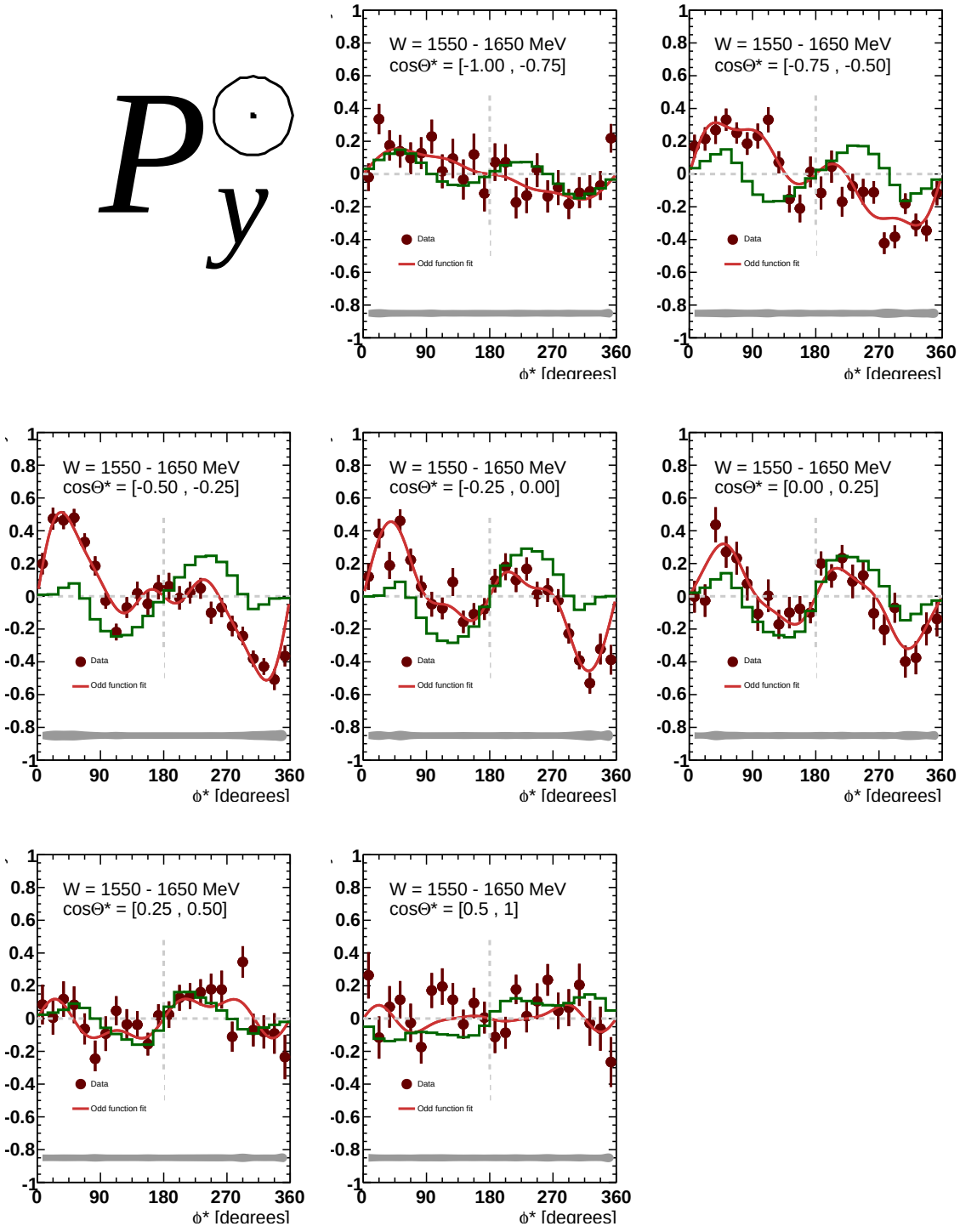

Figure 6.19: Comparison of $P_y^{\odot}$ for $W = 1550 - 1650$ MeV and 7 bins in $\cos\phi^*$ with the model calculation (green curve). The lower gray bands represent the systematic uncertainties.

Chapter 7

Summary

Understanding the complex interaction between quarks and gluons inside protons and neutrons is one of the most significant challenges of physics today, since the pQCD calculation fails to provide solutions in this low-energy regime and thus alternative pathways are needed to explore the complex structure and interactions of baryons. Baryon spectroscopy is one of the useful tools employed by the nuclear scientists, together with the computational power used by Lattice QCD. Since the theoretical models predict "missing resonances" (or missing excited baryon states), there is an ongoing experimental effort to look for these missing baryons, and at JLab, the N^* program focuses on investigating the baryon spectrum, by trying to produce these "missing resonances" through photon-induced excitations. Recent analysis results from JLab data confirmed the existence of five new excited baryon states, progress made possible by experiments using polarized beam and target. A better knowledge of the baryon spectrum will help deepen the current understanding of baryon structure and its properties within QCD, which are strongly correlated to the baryon's degrees of freedom. For the same reasons, this present work tries to find answers to the "missing resonance" problem by analyzing the $\vec{\gamma}\vec{p} \to p\pi^+\pi^-$ reaction channel in order to extract the polarization observables $I^{\odot}$, P_x, P_y, $P_x^{\odot}$, and $P_y^{\odot}$ specific to the interaction of a circularly polarized photon beam with a transversely polarized target in a center of mass energy range from 1.45 GeV to 2.55 GeV. This work presents the comprehensive analysis of this particular reaction channel and its results will help further expand the present understanding of the baryon excited states. The result for

the polarization observable $I^{\odot}$ was compared to the previous published results for the experiment g1c [21] and although a different type of target was used by g1c experiment (pure hydrogen target) and g9b experiment (butanol target), agreement exists between the two experimental results. The other results are first-time measurements for the observables P_x, P_y, $P_x^{\odot}$, and $P_y^{\odot}$. These results were compared to results of a reaction model, which uses a Lagrangian approach to determine the polarized cross-section and polarization observables for this channel. The preliminary comparison showed a lack of agreement between the data and the calculations, indicating that the model needs improvement in order to better predict the dynamics of this particular reaction channel. The extracted observables, together with other experimental results from similar analyses will be used by PWA groups in order to identify the baryon missing excited states, that were predicted by the theoretical calculations but not observed as of now, and hopefully the outcome will help clarify the spectrum of the baryon resonances, which will represent one more step forward in the current understanding of the quark confinement and the strong interaction.

Bibliography

[1] V. Credé and W. Roberts. "Progress towards understanding baryon resonances". In: *Rept. Prog. Phys.* 76 (2013), p. 076301. DOI: 10.1088/0034-4885/76/7/076301. arXiv: 1302.7299 [nucl-ex].

[2] Willibald Plessas and T. Melde. "Relativistic Quark-Model Results for Baryon Ground and Resonant States". In: *AIP Conf. Proc.* 1056 (2008), pp. 15–22. DOI: 10.1063/1.3013036. arXiv: 0811.1752 [hep-ph].

[3] E. Santopinto. "An Interacting quark-diquark model of baryons". In: *Phys. Rev.* C72 (2005), p. 022201. DOI: 10.1103/PhysRevC.72.022201. arXiv: hep-ph/0412319 [hep-ph].

[4] S. Durr et al. "Ab-Initio Determination of Light Hadron Masses". In: *Science* 322 (2008), pp. 1224–1227. DOI: 10.1126/science.1163233. arXiv: 0906.3599 [hep-lat].

[5] Bernard Metsch and Ulrich Loring. "A relativistic quark model of baryons". In: *PiN Newslett.* 16 (2002), pp. 225–231. arXiv: hep-ph/0110415 [hep-ph].

[6] M. Ronniger and B. C. Metsch. "Effects of a spin-flavour dependent interaction on the baryon mass spectrum". In: *Eur. Phys. J.* A47 (2011), p. 162. DOI: 10.1140/epja/i2011-11162-8. arXiv: 1111.3835 [hep-ph].

[7] *Nucleon and Delta Resonances*. http://pdg.lbl.gov/2016/reviews/rpp2016-rev-n-delta-resonances.pdf.

[8] *N(1720)*3/2+. http://www-pdg.lbl.gov/2015/listings/rpp2015-list-N-1720-3o2-plus.pdf.

[9] Kaoru Hagiwara et al. "Review of particle physics. Particle Data Group". In: *Phys.Rev.* D66 (2002), p. 010001. DOI: 10.1103/PhysRevD.66.010001.

[10] W. Roberts and T. Oed. "Polarization observables for two-pion production off the nucleon". In: *Phys.Rev.* C71 (2005), p. 055201. DOI: 10.1103/PhysRevC.71.055201. arXiv: nucl-th/0410012 [nucl-th].

[11] A. Fix and H. Arenhövel. "Double pion photoproduction on nucleon and deuteron". In: *Eur.Phys.J.* A25 (2005), pp. 115–135. DOI: 10.1140/epja/i2005-10067-5. arXiv: nucl-th/0503042 [nucl-th].

[12] Joseph Ballam et al. "Bubble Chamber Study of Photoproduction by 2.8-GeV and 4.7-GeV Polarized Photons. 1. Cross-Section Determinations and Production of ρ_0 and Δ^{++} in the Reaction gamma $p \to p\pi^+\pi^-$". In: *Phys. Rev.* D5 (1972), p. 545. DOI: 10.1103/PhysRevD.5.545.

[13] L. Luke and P. Soeding. In: *Springer Tracts in Modern Physics* 59 ().

[14] Alessandro Braghieri et al. "Double-pion photoproduction up to 800-MeV at Mainz". In: *Proceedings, 7th Conference on Perspectives in Nuclear Physics at Intermediate Energies: Trieste, Italy, May 8-12, 1995*. 1995, pp. 189–198.

[15] L. Y. Murphy and Jean-Marc Laget. "Reaction mechanisms in two pion photoproduction on the proton". In: *Submitted to: Phys. Lett. B* (1995).

[16] J. A. Gomez Tejedor, M. J. Vicente-Vacas, and E. Oset. "Double pion photoproduction in nuclei". In: *Nucl. Phys.* A588 (1995), pp. 819–828. DOI: 10.1016/0375-9474(95)00087-H. arXiv: nucl-th/9411029 [nucl-th].

[17] M. Battaglieri et al. "Photoproduction of the ρ^0 meson on the proton at large momentum transfer". In: *Phys. Rev. Lett.* 87 (2001), p. 172002. DOI: 10.1103/PhysRevLett.87.172002. arXiv: hep-ex/0107028 [hep-ex].

[18] "Photoproduction of Meson and Baryon Resonances at Energies up to 5.8 GeV". In: *Phys. Rev.* 175 (1968), pp. 1669–1696. DOI: 10.1103/PhysRev.175.1669.

[19] H. L. Anderson et al. "Rho meson photoproduction". In: *Phys. Rev.D* 14 (1976), p. 679.

[20] C. Wu et al. "Photoproduction of ρ^0 mesons and Delta-baryons in the reaction $\gamma p \to p\pi^+\pi^-$ at energies up to $s^{1/2} = 2.6$ GeV". In: *Eur. Phys. J.* A23 (2005), pp. 317–344. DOI: 10.1140/epja/i2004-10093-9.

[21] S. Strauch et al. "Beam-helicity asymmetries in double-charged-pion photoproduction on the proton". In: *Phys.Rev.Lett.* 95 (2005), p. 162003. DOI: 10.1103/PhysRevLett.95.162003. arXiv: hep-ex/0508002 [hep-ex].

[22] V. I. Mokeev et al. "Helicity components of the cross section for double charged-pion production by real photons on protons". In: *Phys. Atom. Nucl.* 66 (2003). [Yad. Fiz.66,1322(2003)], pp. 1282–1288. DOI: 10.1134/1.1592582.

[23] Krambric. et al. “Beam-Helicity Asymmetries in Double Pion Photoproduction off the Proton”. In: *Phys. Rev. Lett.* 103 (2009), p. 052002. DOI: 10.1103/PhysRevLett.103.052002. arXiv: 0907.0358 [nucl-ex].

[24] L. Roca. “Helicity asymmetries in double pion photoproduction on the proton”. In: *Nucl. Phys.* A748 (2005), pp. 192–205. DOI: 10.1016/j.nuclphysa.2004.10.028. arXiv: nucl-th/0407049 [nucl-th].

[25] H. A. Grunder et al. “The Continuous Electron Beam Accelerator Facility”. In: *Nucl. Phys.* A478 (1988), pp. 831C–846C. DOI: 10.1016/0375-9474(88)90921-9.

[26] *The aerial view of JLab*. https://www.jlab.org/Hall-B/int-web/aerial.jpg.

[27] C. Keith. *The Frozen Spin Target Layout*. https://userweb.jlab.org/~ckeith/Frozen/CoreManagersMeeting2008.pdf.

[28] B. A. Mecking et al. “The CEBAF Large Acceptance Spectrometer (CLAS)”. In: *Nucl. Instrum. Meth.* A503 (2003), pp. 513–553. DOI: 10.1016/S0168-9002(03)01001-5.

[29] D. I. Sober et al. “The bremsstrahlung tagged photon beam in Hall B at JLab”. In: *Nucl. Instrum. Meth.* A440 (2000), pp. 263–284. DOI: 10.1016/S0168-9002(99)00784-6.

[30] Haakon Olsen and L. C. Maximon. “Photon and Electron Polarization in High-Energy Bremsstrahlung and Pair Production with Screening”. In: *Phys. Rev.* 114 (1959), pp. 887–904. DOI: 10.1103/PhysRev.114.887.

[31] *Circular beam polarization*. https://clasweb.jlab.org/rungroups/g9/wiki/index.php/Circular_Beam_Polarization.

[32] C. D. Keith et al. “The Jefferson Lab Frozen Spin Target”. In: *Nucl. Instrum. Meth.* A684 (2012), pp. 27–35. DOI: 10.1016/j.nima.2012.04.067. arXiv: 1204.1250 [physics.ins-det].

[33] H. Jiang. *Polarization observables T and F in $p(\gamma,\pi^0)p$*. https://www.jlab.org/Hall-B/shifts/admin/paper_reviews/2016/AN_2016_10_21-7405753-2016-10-27-v2.pdf.

[34] C. Keith. *The FROZEN spin target*. https://userweb.jlab.org/~ckeith/Frozen/FROSTposter.pdf.

[35] *Clas detector geometry.* https://www.jlab.org/Hall-B/int-web/clas_large1.jpg.

[36] Y. G. Sharabian et al. "A new highly segmented start counter for the CLAS detector". In: *Nucl. Instrum. Meth.* A556 (2006), pp. 246–258. DOI: 10.1016/j.nima.2005.10.031.

[37] M. D. Mestayer et al. "The CLAS drift chamber system". In: *Nucl. Instrum. Meth.* A449 (2000), pp. 81–111. DOI: 10.1016/S0168-9002(00)00151-0.

[38] E. S. Smith et al. "The time-of-flight system for CLAS". In: *Nucl. Instrum. Meth.* A432 (1999), pp. 265–298. DOI: 10.1016/S0168-9002(99)00484-2.

[39] CLAS Note 2007-016. *Energy loss corrections for charged particles in CLAS.* 2007.

[40] M. Dugger, P.Roy, N. Walford. *Momentum corrections for protons and π^+ in g9b data.* https://misportal.jlab.org/ul/Physics/Hall-B/clas/viewFile.cfm/2013-011.pdf?documentId=720.

[41] *The Tagger Energy Scale: Interpreting the CMU Kinematic Fit Results.* https://www.jlab.org/Hall-B/notes/clas_notes04/2004-019.pdf.

[42] M. Dugger, B.G. Ritchie. *CLAS note draft: Phase Space Dependent Scale Factors for FROST g9a Data.*

[43] D. Besset et al. "A set of efficient estimators for polarization measurements". In: *Nucl. Instrum. Meth.* 166 (1979), pp. 515–520. DOI: 10.1016/0029-554X(79)90543-3.

[44] Tibshirani R. Efron B. *An introduction to the Bootstrap.* http://cds.cern.ch/record/526679/files/0412042312_TOC.pdf.

[45] *Target polarization.* http://www.jlab.org/Hall-B/secure/g9/anetanet/target_pol.pdf.

[46] C. D. Keith. "The JLab frozen spin target". In: *AIP Conf. Proc.* 1149 (2009), pp. 886–889. DOI: 10.1063/1.3215785.